

NOVEL DECOUPLING NETWORKS FOR SMALL
ANTENNA ARRAYS

YU YANTAO

(B.Eng.(Hons.),NUS)

A THESIS SUBMITTED
FOR THE DEGREE OF DOCTOR OF PHILOSOPHY
DEPARTMENT OF ELECTRICAL AND COMPUTER
ENGINEERING
NATIONAL UNIVERSITY OF SINGAPORE

2009

ACKNOWLEDGEMENT

I would like to express my great appreciation to Dr. Jacob Carl Coetzee and Dr. Hui Hon Tat for their invaluable guidance and supervision in this project. I am indebted to them for their understanding, patience and help along the way. Without their help, the thesis would not have been completed successfully. I have benefitted from the valuable experience and knowledge that they have shared with me.

I am also very grateful to Madam Lee Siew Choo, Madam Guo Lin, Mr. Sing Cheng Hiong, Mr. Chan Leong Hin and Mr. Abdul Jalil Bin Din for their help on fabricating and measuring the antennas. I also thank Ms Ho Leng Joo for her encouragement and advice when problems were faced.

I am indebted to my close family for support given throughout my life. Appreciation goes to my parents, relatives and friends for their love and encouragement.

Contents

SUMMARY	iv
List of Figures	v
List of Tables	xi
Chapter 1 Introduction	1
1.1 Background	1
1.2 Objectives of the project	4
1.3 Organization of the thesis	4
1.4 Publications	5
Chapter 2 Theoretical Background	7
2.1 Introduction	7
2.2 Digital beam forming	7
2.3 Mutual coupling	10
2.4 The need for a decoupled array.....	12
Chapter 3 Decoupling Network Design Using Eigenmode Analysis	15
3.1 Introduction.....	15
3.2 Modal representation of a dense antenna array	15
3.3 Properties of multi-port dense antenna array	19
3.3.1 Antenna properties by means of eigenmode models	21
3.4 DBF in multi-port dense antenna array	24
3.5 DN for multi-port dense antenna array	27
3.6 DN design and realization	30
3.6.1 DN for 3-port antenna array	30
3.6.1.1 Eigenmode analysis	32

3.6.1.2	Network analysis	33
3.6.1.3	Matching network	34
3.6.1.4	DN implementation and measurement results	37
3.6.2	DN for 4-port antenna array by eigenmode analysis.....	41
3.6.2.1	Eigenmode analysis	44
3.6.2.2	Measurement results	55
Chapter 4	Closed-form Design Equations for Decoupling Network of Circulant Symmetric Dense Array	58
4.1	Introduction	58
4.2	Design of decoupling networks for small arrays	58
4.3	Design of decoupling networks for larger arrays	64
4.3.1	Basic circuit model	65
4.3.2	Decoupling of larger arrays.....	66
4.3.2.1	Decoupling of a circular symmetrical 6-element array	67
4.3.2.2	Decoupling of a circular symmetrical 8-element array	88
Chapter 5	Decoupling Network Design Using Modal Feed Network	121
5.1	Introduction	121
5.2	The inspiration of the alternative design of decoupling network	121
5.3	Theory and design of modal feed network	122
5.3.1	S-parameters of feed network and array combination	122
5.3.2	Ideal modal feed network	124
5.3.3	Practical modal feed network	127
5.4	Results of design examples and discussion	128
5.4.1	Modal feed network for 2-element monopole array	129

5.4.2	Modal feed network for 2×2 element monopole array	136
5.4.3	Compact modal feed network for 2×2 element monopole array ...	144
Chapter 6	Conclusions	158
	REFERENCE	161
	APPENDIX A: PROGRAM CODE IN MATHEMATICA FOR CLOSED-FORM DESIGN EQUATIONS OF 6-ELEMENT ARRAY	168
	APPENDIX B: CIRCUIT MODEL IN IE3D TO CALCULATE THE S-PARAMETERS OF THE DECOUPLED 6-ELEMENT ARRAY	172
	APPENDIX C: CIRCUIT MODEL IN IE3D TO CALCULATE THE RADIATION PATTERN OF THE DECOUPLED 6-ELEMENT ARRAY	173
	APPENDIX D: CIRCUIT MODEL IN ADS TO CALCULATE THE S-PARAMETERS OF THE DECOUPLED 6-ELEMENT ARRAY	174
	APPENDIX E: ARRAY MODEL IN HFSS TO CALCULATE THE RADIATION PATTERN WITH FINITE GROUND PLANE	175

SUMMARY

Antenna arrays with multiple isolated ports are widely used in space-time techniques like diversity reception, MIMO technique, adaptive beamforming or nulling and direction finding. For applications on size-limited platforms (e.g. in mobile terminals), restrictions on the available space demand the use of an element spacing significantly smaller than $\lambda/2$. The small element spacing introduces strong mutual coupling between the ports of the compact arrays. The strong coupling can cause significant system performance degradation. An RF decoupling network may be used to compensate for the mutual coupling effects. A systematic decoupling network design approach using eigenmode analysis is proposed. It involves the step-by-step decoupling of the characteristic eigenmodes of the array. The decoupling networks contain only lossless reactive components. In practical implementation, the lossless reactive components are usually converted to microstrip lines or striplines. These networks are sometimes much larger in size than the array itself, which makes the concept less suitable for applications where the available space for the antennas is limited. Therefore, an alternative approach to realize port decoupling is also presented. Antenna elements are fed via a modal feed network where isolation between the new input ports is achieved by exploiting the inherent orthogonality of the eigenmodes of the array. For beam forming, the required element weights are obtained as a linear combination of the orthogonal eigenvectors. This new approach is easy to understand and provides a simple design procedure of decoupling. The size of the decoupling network can be significantly reduced. This makes it suitable for application in mobile devices.

List of Figures

Figure 2.1 120° sectorized cell pattern	8
Figure 2.2 Independently steered beams	9
Figure 2.3 A generic DBF antenna system	9
Figure 2.4 Two element monopole array	11
Figure 2.5 Equivalent circuit for m th eigenmode of array in receive mode	12
Figure 3.1 The basic diagram of MIMO systems	16
Figure 3.2 Equivalent $(N + 1)$ -port network of antenna arrays	16
Figure 3.3 Mode model for multi-port antenna	22
Figure 3.4 Dense multi-port antennas with DN	28
Figure 3.5 DN for a two-port antenna	30
Figure 3.6 A 3-element monopole array	31
Figure 3.7 A generalized DN for a 3-element array	32
Figure 3.8 Equivalent circuits for different modes of 3-element array	33
Figure 3.9 L section matching networks for cases where (a) $R_L > R_{in}$ and (b) $R_L < R_{in}$	35
Figure 3.10 A 3-element array with decoupling and matching network	36
Figure 3.11 The 3-element array with supporting structure	38
Figure 3.12 Photo of microstrip network	39
Figure 3.13 Simulated and measured S_{11} of array to be decoupled	39
Figure 3.14 Simulated and measured S_{12} of array to be decoupled	40
Figure 3.15 Simulated and measured S_{11} of the decoupled and matched array	41
Figure 3.16 Simulated and measured S_{12} of the decoupled and matched array	41
Figure 3.17 Single aperture-coupled ring patch	42
Figure 3.18 Four-element aperture-coupled ring patch array	43

Figure 3.19 S-Parameters of the optimized array	44
Figure 3.20 DN topology for 4-port array	46
Figure 3.21 General circuit for the lemma	46
Figure 3.22 The circle defined by Equation (3.66) on GB plane	47
Figure 3.23 Equivalent circuit for mode 1 with DN	48
Figure 3.24 Equivalent circuit for mode 2 and 3 with DN	49
Figure 3.25 Equivalent circuit for mode 4 with DN	50
Figure 3.26 S-parameters of the array with decoupling and matching network	55
Figure 3.27 Photo of the front of the array	56
Figure 3.28 Photo of the back of the array	56
Figure 3.29 Measured S-parameters of the decoupled and matched array	57
Figure 4.1 Decoupling networks for (a) a 2-element array and (b) a symmetrical 3-element array	60
Figure 4.2 Scattering parameters of the 2-element monopole array	62
Figure 4.3 Scattering parameters of the 3-element monopole array	62
Figure 4.4 Normalized azimuth radiation pattern of the 2-element array	63
Figure 4.5 Normalized azimuth radiation pattern of the 3-element array	64
Figure 4.6 General circuit model for matching two distinct terminating impedances	65
Figure 4.7 Stage network configurations for 6-element array	68
Figure 4.8 Equivalent network of the circuits in Figure 4.7 when mode m is excited	68
Figure 4.9 Equivalent circuit of the first circuit in Figure 4.7 for mode a	70
Figure 4.10 Equivalent circuit of the first circuit in Figure 4.7 for mode b	71
Figure 4.11 Equivalent circuit of the first circuit in Figure 4.7 for modes c and d	72
Figure 4.12 Equivalent circuit of the first circuit in Figure 4.7 for modes e and f	73
Figure 4.13 Equivalent circuit of the second circuit in Figure 4.7 for mode a	74

Figure 4.14 Equivalent circuit of the second circuit in Figure 4.7 for mode b	75
Figure 4.15 Equivalent circuit of the second circuit in Figure 4.7 for modes c and d	76
Figure 4.16 Equivalent circuit of the second circuit in Figure 4.7 for modes e and f	77
Figure 4.17 Equivalent circuit of the third circuit in Figure 4.7 for mode a	78
Figure 4.18 Equivalent circuit of the third circuit in Figure 4.7 for mode b	79
Figure 4.19 Equivalent circuit of the third circuit in Figure 4.7 for modes c and d	80
Figure 4.20 Equivalent circuit of the third circuit in Figure 4.7 for modes e and f	81
Figure 4.21 Complete decoupling network for a symmetrical 6-element array	83
Figure 4.22 Scattering parameters of the decoupled and matched 6-element array	87
Figure 4.23 Normalized azimuth radiation pattern of the decoupled 6-element array	87
Figure 4.24 Stage network configurations for 8-element array	89
Figure 4.25 Equivalent circuit of the first circuit in Figure 4.24 for mode a	90
Figure 4.26 Equivalent circuit of the first circuit in Figure 4.24 for mode b	91
Figure 4.27 Equivalent circuit of the first circuit in Figure 4.24 for modes c and d	92
Figure 4.28 Equivalent circuit of the first circuit in Figure 4.24 for modes e and f	95
Figure 4.29 Equivalent circuit of the first circuit in Figure 4.24 for modes g and h	96
Figure 4.30 Equivalent circuit of the second circuit in Figure 4.24 for mode a	98
Figure 4.31 Equivalent circuit of the second circuit in Figure 4.24 for mode b	98
Figure 4.32 Equivalent circuit of the second circuit in Figure 4.24 for modes c and d	99
Figure 4.33 Equivalent circuit of the second circuit in Figure 4.24 for modes e and f	100
Figure 4.34 Equivalent circuit of the second circuit in Figure 4.24 for modes g and h	101
Figure 4.35 Equivalent circuit of the third circuit in Figure 4.24 for mode a	102

Figure 4.36 Equivalent circuit of the third circuit in Figure 4.24 for mode b	103
Figure 4.37 Equivalent circuit of the third circuit in Figure 4.24 for modes c and d	104
Figure 4.38 Equivalent circuit of the third circuit in Figure 4.24 for modes e and f	105
Figure 4.39 Equivalent circuit of the third circuit in Figure 4.24 for modes g and h	106
Figure 4.40 Equivalent circuit of the fourth circuit in Figure 4.24 for mode a	107
Figure 4.41 Equivalent circuit of the fourth circuit in Figure 4.24 for mode b	108
Figure 4.42 Equivalent circuit of the fourth circuit in Figure 4.24 for modes c and d	109
Figure 4.43 Equivalent circuit of the fourth circuit in Figure 4.24 for modes e and f	110
Figure 4.44 Equivalent circuit of the fourth circuit in Figure 4.24 for modes g and h	111
Figure 4.45 Decoupling circuit for 8-element array	113
Figure 4.46 Scattering parameters of the decoupled and matched 8-element array .	119
Figure 4.47 Normalized azimuth radiation pattern of the 8-element array	120
Figure 5.1 $(M+N)$ -port feed network connected to an N -element array	123
Figure 5.2 Network setup in ADS to verify modal feed network	126
Figure 5.3 Monopole array element used in the construction of prototype arrays ...	129
Figure 5.4 Port numbering for a rat-race 180° hybrid coupler which acts as modal feed network for the 2-element array	130
Figure 5.5 2-element monopole array mounted on a substrate	131
Figure 5.6 Measured S-parameters of the 2-element monopole array	132
Figure 5.7 Modal feed network implemented as a rat-race hybrid on the lower surface of the substrate	132
Figure 5.8 Measured S-parameters of the hybrid coupler connected to the 2-element monopole array	133
Figure 5.9 Measured S-parameters of the 2-element monopole array with matching networks at the external ports of the modal feed network	134

Figure 5.10 Measured S-parameters of the 2-element monopole array with tuned matching networks at the external ports of the modal feed network	134
Figure 5.11 Simulated and measured radiation patterns for mode 1 of the 2-element monopole array	135
Figure 5.12 Simulated and measured radiation patterns for mode 2 of the 2-element monopole array	136
Figure 5.13 8-port modal feed network for the 2×2 element array	138
Figure 5.14 2×2 element monopole array with inter-element spacing of 20 mm ...	139
Figure 5.15 Measured scattering parameters of the 2×2 array	139
Figure 5.16 8-port modal feed network consisting of four -3 dB 90° branchline couplers	140
Figure 5.17 Measured scattering parameters of the modal feed network connected to the 2×2 array	141
Figure 5.18 Measured scattering parameters of the 2×2 array with matched external ports of the modal feed network	141
Figure 5.19 Simulated radiation patterns (normalized) of the 2×2 array for eigenmodes 1 and 2	142
Figure 5.20 Simulated radiation patterns (normalized) of the 2×2 array for eigenmodes 3 and 4	143
Figure 5.21 Schematic diagram of an 8-port hybrid ring circuit based on four coupled line 90° hybrids	145
Figure 5.22 2×2 element monopole array with compact ring-type comparator circuit as modal feed network	147
Figure 5.23 Prototype 2×2 element monopole array with decoupled ports.....	148
Figure 5.24 Ring etched on the bottom surface of first layer	148

Figure 5.25 Ring etched on the bottom surface of second layer	149
Figure 5.26 Measured S-parameters of the original 2×2 monopole array	149
Figure 5.27 Measured S-parameters of the modal feed network connected to the 2×2 array	150
Figure 5.28 Measured S-parameters of the 2×2 array with matched external ports of the modal feed network	151
Figure 5.29 Radiation pattern (normalized) of the 2×2 array for eigenmode 1	151
Figure 5.30 Radiation pattern (normalized) of the 2×2 array for eigenmode 2	152
Figure 5.31 Radiation pattern (normalized) of the 2×2 array for eigenmode 3	152
Figure 5.32 Radiation pattern (normalized) of the 2×2 array for eigenmode 4	153
Figure 5.33 Redesigned prototype of 2×2 monopole array with decoupled ports ...	154
Figure 5.34 Measured S-parameters of the redesigned prototype array	155
Figure 5.35 Radiation pattern (normalized) of the redesigned prototype 2×2 array for eigenmode 1	155
Figure 5.36 Radiation pattern (normalized) of the redesigned prototype 2×2 array for eigenmode 2	156
Figure 5.37 Radiation pattern (normalized) of the redesigned prototype 2×2 array for eigenmode 3	156
Figure 5.38 Radiation pattern (normalized) of the redesigned prototype 2×2 array for eigenmode 4	157

List of Tables

Table 3.1 Dimensions of the 3 element monopole array	31
Table 3.2 Decoupling network and matching network configurations	37
Table 3.3 Transformation of ideal components to microstrip stubs	38
Table 3.4 Dimensions of the aperture-coupled ring patch	43
Table 4.1 Dimensions of the 2-element and 3-element monopole arrays	61
Table 4.2 Calculated decoupling and matching network elements for small arrays ..	61
Table 4.3 Basic circuit configurations for mode decoupling	82
Table 4.4 S-parameters and decoupling network elements for the 6-element array ..	86
Table 4.5 Basic circuit configurations for mode decoupling	112
Table 4.6 S-parameters and decoupling network elements for the 8-element array ..	118
Table 5.1 Simulation results in ADS	127

Chapter 1 Introduction

1.1 Background

Multi-antenna technology may be viewed as an extension of the so-called smart antenna [1], a popular technology for improving wireless communication dating back to 1950s. In multiple-input-multiple-output (MIMO) wireless communication techniques, multiple antennas are employed at both ends of the wireless link to significantly improve system performance [2]. In wireless systems such as mobile, personal communications, and wireless PBX/LAN networks, the use of multiple antennas can result in a significant increase in system capacity. With 2 or 3 antennas, the capacity of a mobile radio system can be doubled, while a 7-fold capacity increase can be achieved with 5 antennas [3]. Antenna arrays with multiple ports can also be used in space-time techniques like diversity reception, adaptive beamforming or nulling and direction finding. Multi-port antennas usually have the design goal of isolated ports and uncorrelated radiation patterns. However, when two or more antennas are in close proximity of each other, there is an interchange of energy between them. This interchange of energy constitutes mutual coupling among the antenna elements. Mutual coupling becomes particularly significant as the inter-element spacing is decreased [4]. It has been shown [5, 6] that the performance of an adaptive antenna array is strongly affected by the electromagnetic characteristics of the antenna array, like the mutual coupling between its elements. The goal of isolation is normally achieved by ensuring a sufficient inter-element spacing of at least $\lambda/2$ in order to inhibit the effects of mutual coupling. However, in the case of size-limited platforms like mobile applications, the required diversity can only be achieved if an element spacing significantly smaller than $\lambda/2$ is utilized. With such

small element spacing mutual coupling is not any longer negligible [7, 8]. The increased mutual coupling between the antenna elements apparently does not affect the capacity of a MIMO system [9], but it will decrease the antenna gain considerably and thus cause significant system performance degradation [4, 10, 11]. Mutual coupling causes a reduction in the signal-to-noise ratio (SNR) [4, 12]. The decrease in the SNR reduces the detection range and increases the minimum detectable velocity of the target in spacetime adaptive processing [12]. The presence of mutual coupling also decreases the eigenvalues of the covariance matrix of the signal, which controls the response time of an adaptive array [4]. Studies have also examined the effect of mutual coupling on pattern characteristics for a variety of communication applications [13-17]. In many applications, the available volume restricts the physical size of the antennas. For maximum versatility, the number of elements in an adaptive array needs to be as large as possible. On the other hand, the increased mutual coupling associated with a decrease in element spacing limits the frequency bandwidth and increases the sensitivity to dissipative losses. The required bandwidth and radiation efficiency dictates the maximum number of array elements for a given platform size. It is therefore vital that mutual coupling be taken into consideration during the design of arrays with small element spacing.

This has attracted much attention and various compensation techniques have been proposed. In shaped beam antennas, modification of the excitation vector can compensate for mutual coupling [18]. Signal processing techniques may be applied to the received signal vectors from adaptive arrays in digital beam forming (DBF) and direction finding applications to counter the effects of mutual coupling [19-22]. However, the SNR of receiver or transmitter channels can only be optimized through

proper matching of the port impedances of the array for arbitrary element excitations. Due to mutual coupling, port impedances vary for different element excitations and cannot be simultaneously matched to the optimum source impedance. SNR degradation resulting from impedance mismatches cannot be compensated for through signal processing, but can be overcome via the implementation of a RF decoupling network (DN) [23-25]. Various implementations of decoupling networks have been described in the literature. In its simplest form, the decoupling network consists of reactive elements connected between neighboring array elements, which effectively cancels the external mutual coupling between them. However, this is only applicable in special cases where the off-diagonal elements of the admittance matrix are all purely imaginary [23, 24, 26]. Decoupling networks for arrays with arbitrary complex mutual admittances were described in [27-29]. The DNs for 3-element and 4-element arrays described in [28, 29] are symmetrical networks. Network elements were obtained by either applying an eigenmode analysis or a complete network analysis of the DN/array combination. The design of decoupling networks for larger arrays with 4 or more elements is presented in the thesis. For circulant symmetric arrays, a systematic design approach can be formulated by involving the step-by-step decoupling of the characteristic eigenmodes of the array.

An alternative approach to achieve port decoupling is also proposed. It involves a modal feed network which makes use of the orthogonality of the eigenmodes of the array to achieve decoupling. The input ports to the feed network and array combination can then be matched independently. In digital beam forming applications, the required element weights are obtained as a linear combination of the orthogonal eigenmode vectors.

1.2 Objectives of the project

This project aims to develop design concepts of decoupling networks for compact arrays with small element spacing. Different ways of achieving decoupling between the antenna ports are investigated analytically. Procedures for the design and realization of the decoupling networks are to be developed and verified with experimental results.

1.3 Organization of the thesis

This thesis consists of six chapters, including this introductory chapter. Chapter 2 provides the theoretical background on dense arrays for digital beam-forming and the theory of mutual coupling. Chapter 3 presents a brief review of related work on characteristics of dense arrays and the modal model. It also describes the decoupling network design using the eigenmode analysis with design examples of 3-element and 4-element arrays. Chapter 4 describes a systematic design approach for decoupling larger arrays. It involves the step-by-step decoupling of the characteristic eigenmodes of the array, illustrated with design examples. Chapter 5 presents the alternative approach to achieve port decoupling by using the modal feed network, where isolation between the new input ports is achieved by exploiting the inherent orthogonality of the eigenmodes of the array. Design examples with experimental results are included. Chapter 6 gives some concluding remarks on this project.

1.4 Publications

Journal papers:

1. J. C. Coetzee and Y. Yu, "Port decoupling for small arrays by means of an eigenmode feed network", *IEEE Trans. Antennas and Propagation*, vol. 56, no. 6, pp.1587-1593, Jun 2008.
2. J. C. Coetzee and Y. Yu, "New Modal Feed Network for a Compact Monopole Array with Isolated Ports", *IEEE Trans. Antennas and Propagation*, vol. 56, no.12, pp.3872-3875, Dec 2008.
3. J. C. Coetzee and Y. Yu, "Closed-form Design Equations for Decoupling Networks of Small Arrays", *Electronics Letters*, vol. 44, no. 25, pp.1441-1442, Dec 2008.
4. J. C. Coetzee and Y. Yu, "Design of Decoupling Networks for Circulant Symmetric Antenna Arrays", *IEEE Antennas and Wireless Propagation Letters*, vol. 8, pp.291-294, 2009.

Conference papers:

5. J. C. Coetzee and Y. Yu, "Size reduction of a 4-port microstrip antenna array with a simplified decoupling and matching network", in *Proc. IEEE AP-S/URSI Symp.*, Washington DC, USA, Jul 2005.
6. J. C. Coetzee and Y. Yu, "An alternative approach to decoupling of arrays with reduced element spacing", in *Proc. Int. Symp. on Antennas and Propagation (ISAP)*, Singapore, Nov 2006.

7. J. C. Coetzee and Y. Yu, "A Compact 4-Element Monopole Array with Isolated Ports", in *Proc. IEEE AP-S/URSI Symp.*, San Diego, California, USA, Jul 2008.
8. J. C. Coetzee and Y. Yu, "A Compact Monopole Array with Decoupled Ports", in *Proc. IEEE Int. RF and Microwave Conference*, Kuala Lumpur, Malaysia, Dec 2008.

Awards:

Best paper gold award (2nd place), IEEE International RF and Microwave Conference, Kuala Lumpur, Malaysia, Dec 2008 for paper [8].

Chapter 2 Theoretical Background

2.1 Introduction

This chapter introduces the theoretical background to the project. It includes digital beam forming and its applications, the theory of mutual coupling and the need for a decoupled array.

2.2 Digital beam forming

With the increasing demand for wireless services, telecommunications has evolved from the traditional wired phone to personal communication services (PCS). This brings about an increase in the type of wireless services provided, such as fixed, mobile, outdoor and indoor, and satellite communications. As PCS provides pervasive communication services, it will require much higher levels of system capacity than the current mobile systems. The capacity of a communications system can be increased directly by enlarging the bandwidth of the existing communications channels or by allocating new frequencies to the service. However, since the electromagnetic spectrum is limited and becoming congested with a proliferation of sources of interference, it is usually not feasible to increase system capacity by opening new spectrum space for wireless communications applications. Instead, efficient reuse of the existing frequency resources is critical.

Many multiple access techniques have been used to maximize the capacity of the existing frequency resources. Space-division multiple access (SDMA) is one of them. In SDMA, the geographical coverage area is divided into a large number of cells. The same frequency can be reused in different cells that are separated by a spatial distance

to reduce the level of co-channel interference. However, for a given amount of base station transmission power, there is a limit on the number of cells that can be served in a particular geographical area, and hence a limit on the capacity that the base station can support. Therefore, to further increase the capacity, advanced forms of SDMA are needed. The advanced forms of SDMA use smart antennas, or more commonly known as adaptive antennas. These antennas are capable of beam-forming. For example, 120° sectorial beams at different carrier frequencies can be used within a cell and each sectorial beam can be used to serve the same number of users as are served in the case of ordinary cells [30], as illustrated in Figure 2.1. This technique triples the capacity of the cell. The ultimate form of SDMA is to use independently steered high-gain beams at the same carrier frequency to provide service to individual user within a cell [30], as shown in Figure 2.2.

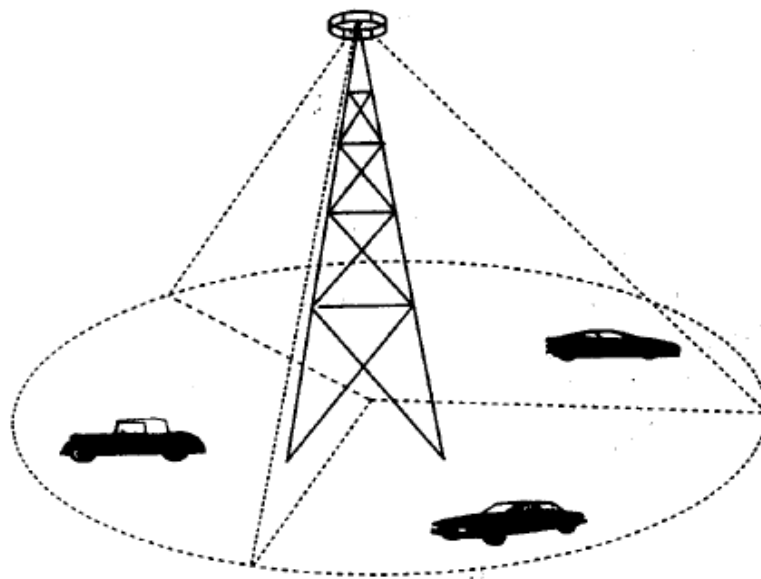


Figure 2.1 120° sectorized cell pattern [30]

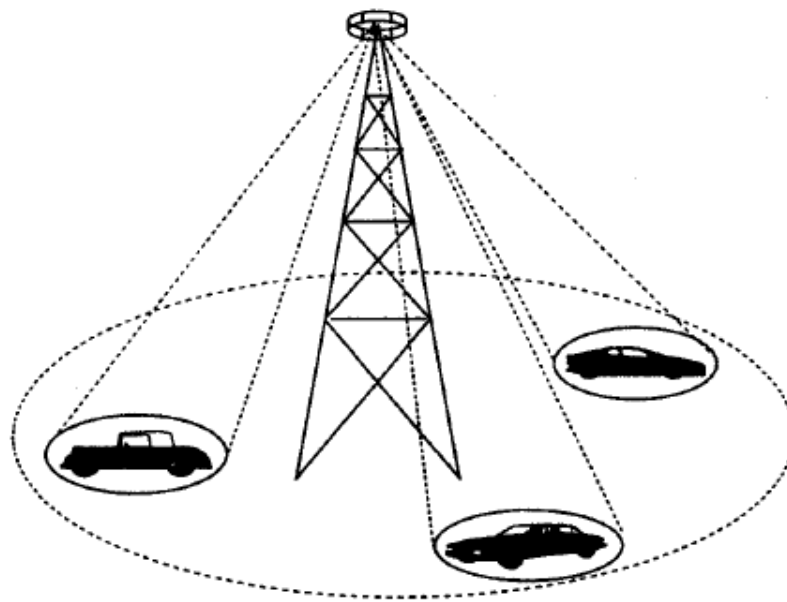


Figure 2.2 Independently steered beams [30]

By employing digital beam-forming (DBF) techniques, more flexibility and control can be achieved from smart antennas. A DBF antenna can be considered as the ultimate antenna, since it has the ability to capture all the information incident on the antenna and apply appropriate signal processing technology to make the information useful to the observer. DBF is a marriage between antenna technology and digital technology. Figure 2.3 shows a generic DBF antenna system [30].

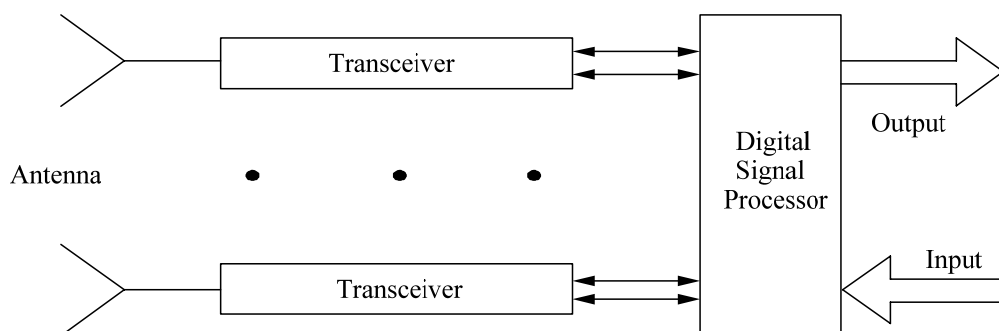


Figure 2.3 A generic DBF antenna system

It consists of three major components, namely the antenna array, the digital transceivers, and the digital signal processor [30]. DBF is a system in which the RF signal received by the antenna array is digitized and processed digitally. The radiation patterns of the antenna can be controlled by digital signal processing techniques to achieve the desired performance [30-38].

2.3 Mutual coupling

When two or more antennas are in close proximity of each other, there is an exchange of energy between them. This exchange of energy constitutes mutual coupling among the antenna elements. The presence of a nearby element alters the current distribution, radiated field and input impedance of an antenna. Therefore, the performance of the antenna depends not only on its own current but also on the current of neighboring elements. With the emerging trends to employ multipoint antenna technologies at mobile terminals, mutual coupling is prominent and the assumption of constant SNR in many publications [39, 40] no longer holds due to the limited space allocated to antenna systems. Therefore, considering a dense antenna array as a radiating structure with mutual coupled ports is more suitable.

For an antenna element, there are two types of impedance associated with it. The first type is the driving point impedance. This depends on the self-impedance, that is, the input impedance in the absence of other elements. The second type is arriving point impedance, which is dependent on the mutual impedance between the driven element and other elements. Consider a two-element antenna system as shown in Figure 2.4.

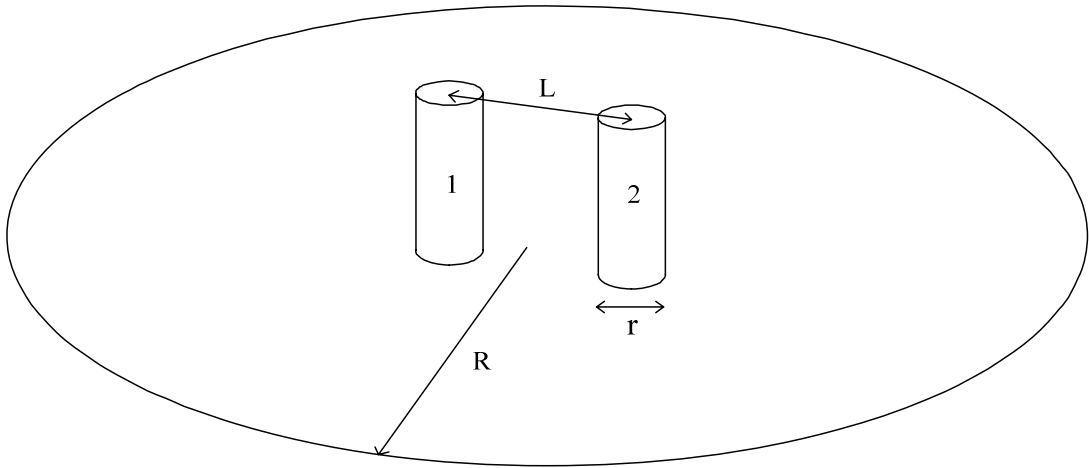


Figure 2.4 Two element monopole array

The two-element system is equivalent to a two-port network. The voltage-current relations can be written as:

$$\begin{aligned} V_1 &= Z_{11}I_1 + Z_{12}I_2 \\ V_2 &= Z_{21}I_1 + Z_{22}I_2 \end{aligned} \quad (2.1)$$

where

$$\begin{aligned} Z_{11} &= \left. \frac{V_1}{I_1} \right|_{I_2=0} \\ Z_{12} &= \left. \frac{V_1}{I_2} \right|_{I_1=0} \\ Z_{21} &= \left. \frac{V_2}{I_1} \right|_{I_2=0} \\ Z_{22} &= \left. \frac{V_2}{I_2} \right|_{I_1=0} \end{aligned} \quad (2.2)$$

Z_{11} and Z_{22} are the self-impedances of antenna elements 1 and 2 respectively; Z_{12} and Z_{21} are the mutual impedances. The driving-point impedances are given as

$$\begin{aligned} Z_{1d} &= \frac{V_1}{I_1} = Z_{11} + Z_{12} \frac{I_2}{I_1} \\ Z_{2d} &= \frac{V_2}{I_2} = Z_{22} + Z_{21} \frac{I_1}{I_2} \end{aligned} \quad (2.3)$$

To match an antenna element, the driving-point impedance needs to be adjusted to a required value. Since mutual impedance affects the driving-point impedance, it plays an important role in the performance of the array.

2.4 The need for a decoupled array

For an array with M elements, there exist M mutually orthogonal eigenmodes. The mode admittance associated with eigenmode m is given by $Y_m = G_m + jB_m$, where G_m and B_m are respectively the conductance and susceptance of mode m . The mode admittance is equal to the m th eigenvalue of the admittance matrix. By means of eigenmode representation, the array with mutually coupled elements can be replaced with a set of equivalent antennas whose radiation patterns correspond to the mutually orthogonal radiation patterns [23, 24]. In the receive mode, each of the equivalent antennas can be modeled as a current source with source admittance equal to the corresponding mode admittance Y_m and current source i_m , as illustrated in Figure 2.5. A receiver channel with input admittance $Y_{in,rec}$ is connected to the antenna. A noise voltage and a noise current source, as shown in Figure 2.5, represent the noise characteristics of the receiver channel.

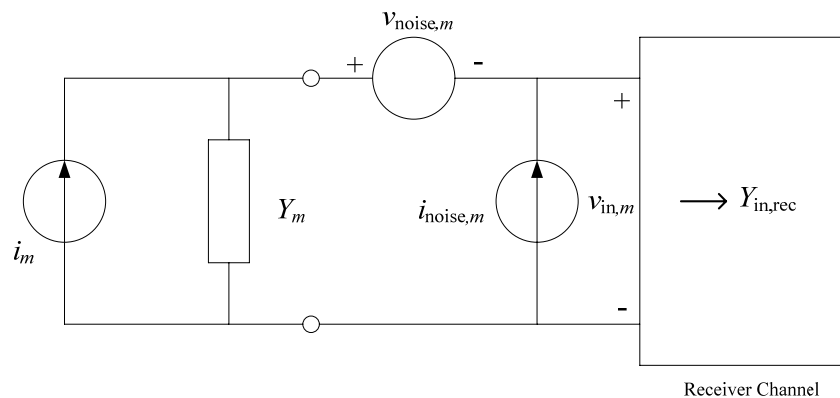


Figure 2.5 Equivalent circuit for m th eigenmode of array in receive mode

The performance of the array, in terms of power matching and signal-to-noise-ratio (SNR), is affected by the mutual coupling between the array elements.

The power contribution from mode m is maximized if the condition $Y_m^* = Y_{\text{in,rec}}$ is met. In an ideal case with no mutual coupling between the array elements, all the mode admittances are equal to each other. Simple two-port matching networks between the antenna ports and receiver channels can transform the mode admittances to meet the condition for maximum power transfer. However, in the presence of mutual coupling, the mode admittances are not identical and simultaneous matching for all modes cannot be achieved via two-port matching networks [24]. If one particular mode is selected for power matching, the other modes will be mismatched. Mismatch of a mode results in a decrease in transducer power gain for that mode relative to the case of power matching.

In analysis of the circuit model in Figure 2.5, it is taken into account that the effective receiver noise temperature T_{eff} is a function of the source admittance Y_m . The minimum receiver noise temperature $T_{\text{eff,min}}$ is achieved when the source admittance equals an optimum value $Y_{\text{opt}} = G_{\text{opt}} + jB_{\text{opt}}$. The effective noise temperature for mode m can be written as [23, 24]

$$T_{\text{eff},m} = T_{\text{eff,min}} + T_0 R_{\text{eq}} \frac{|Y_m - Y_{\text{opt}}|^2}{G_m}, \quad (2.4)$$

where R_{eq} and T_0 are the equivalent noise resistance and the room temperature respectively.

For an array with incident signal given by $\mathbf{E}_{\text{inc}}(\Theta, \Phi)$, the SNR is given by [23, 24]

$$\text{SNR} = \frac{\sum_{m=1}^M |\tilde{w}_m \mathbf{C}(\Theta, \Phi) \cdot \mathbf{E}_{\text{inc}}(\Theta, \Phi)|^2}{T_{\text{eff}, \text{min}} \sum_{m=1}^M |\tilde{w}_m|^2 + T_0 R_{\text{eq}} \sum_{m=1}^M |\tilde{w}_m|^2 \frac{|Y_m - Y_{\text{opt}}|^2}{G_m}}, \quad (2.5)$$

where $\mathbf{C}(\Theta, \Phi)$ is a vector function that defines the mode radiation patterns, and \tilde{w}_m is a set of effective weights for adjustments to form the desired radiation pattern.

From (2.5), it is clear that the maximum SNR is achieved when all mode admittances are noise-matched: $Y_m = Y_{\text{opt}}$ for $m = 1, 2, \dots, M$. In the presence of mutual coupling between the array elements, noise matching for a selected mode can only be achieved at the cost of noise-mismatch for the remaining modes. In addition, the SNR becomes a function of the effective weights and also a function of the desired radiation pattern. It has been shown in [23, 24] that signal-to-noise maximization can only be achieved if all mode admittances of the array are identical and matched to the optimum admittance. This necessitates the use of a decoupling network. It has been suggested that by connecting simple reactive elements between the input ports and antenna ports, the mutual coupling between the antenna elements can be completely removed [26]. However, this can only be implemented in cases where the off-diagonal elements of the admittance matrix are all purely imaginary. In the design of decoupling networks for arrays with arbitrary complex mutual admittances, eigenmode and network analysis can be applied, which will be presented in detail in the following chapters.

Chapter 3 Decoupling Network Design Using Eigenmode Analysis

3.1 Introduction

This chapter presents a brief review of related work on characteristics of dense arrays and a modal model from Chaloupka [23-25]. It describes the design of decoupling networks for 3-element and 4-element arrays using eigenmode analysis or network analysis. Analytical solutions and experimental results verify both analysis methods.

3.2 Modal representation of a dense antenna array

Figure 3.1 shows the basic diagram of an adaptive array in [4]. The output signal from each element is multiplied by a complex weight, and then these signals are summed to produce the array output $S(t)$. The weights are automatically adjusted to optimize some desired criteria, e.g. SNR, with a selected algorithm. To study the behavior of a dense array, we must know the element/port output voltages. These port output voltages will be used as the input signals to the processor. Therefore, Gupta and Ksienski [4] developed the expression for the element output voltages when the mutual coupling is taken into account. The expression, as in Equation (3.9), was developed by considering the N -element array as an $(N+1)$ -terminal linear, bilateral network responding to an outside source, as shown in Figure 3.2.

As shown in Figure 3.2, each port of the N -element array is terminated in a known load impedance Z_{Lk} ($k = 1, 2, \dots, N$). For the sake of simplicity, we first consider the case $Z_{L1} = Z_{L2} = \dots = Z_{LN} = Z_L$ here. The far field radiation is symbolized as a driving source with open circuit voltage V_g and internal impedance Z_g . With these notations, the Kirchoff relation for the $(N + 1)$ -port network is given as below:

$$\begin{aligned}
 V_1 &= I_1 Z_{11} + I_2 Z_{12} + \dots + I_N Z_{1N} + I_g Z_{1S} \\
 V_2 &= I_1 Z_{21} + I_2 Z_{22} + \dots + I_N Z_{2N} + I_g Z_{2S} \\
 &\vdots \\
 V_N &= I_1 Z_{N1} + I_2 Z_{N2} + \dots + I_N Z_{NN} + I_g Z_{NS}
 \end{aligned}
 \tag{3.1}$$

where non-vanishing $Z_{ij} = Z_{ji}$ ($i, j = 1, 2, \dots, N$) represents the mutual impedance between the ports (array elements) i and j . Here Z_{kS} ($k = 1, 2, \dots, N$) is the mutual impedance between port (array element) k and the hypothesized port at the driving source and it shows the “coupling to free space”.

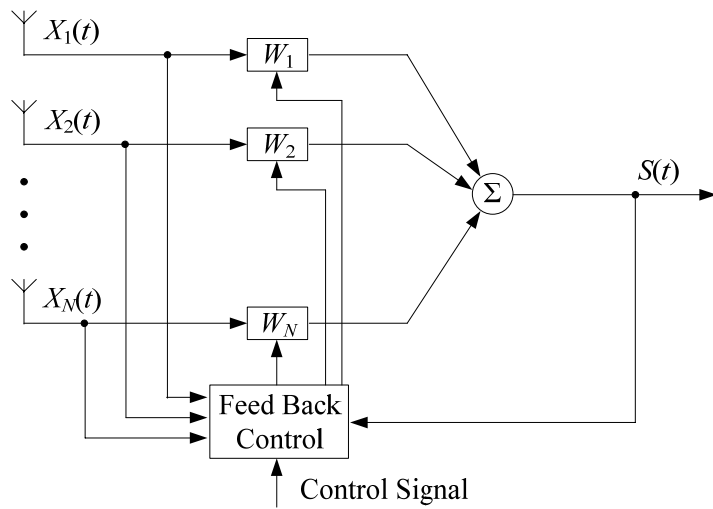


Figure 3.1 The basic diagram of an adaptive array

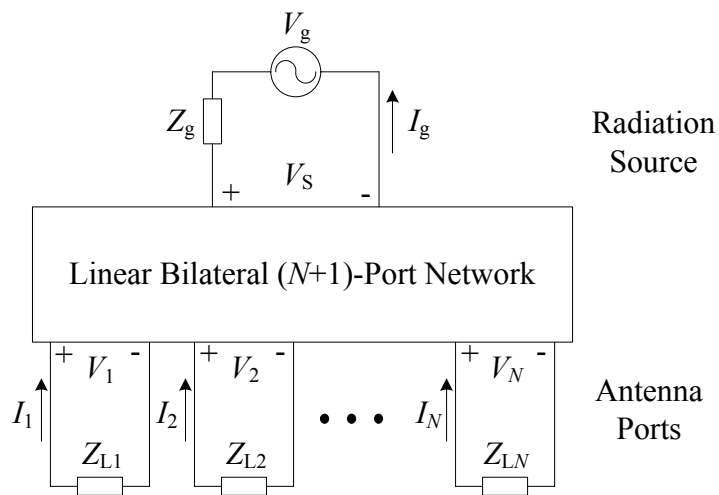


Figure 3.2 Equivalent $(N + 1)$ -port network of antenna arrays

Furthermore, making use of the relationship between terminal current and load impedance, we have

$$I_j = -\frac{V_j}{Z_L}, j = 1, 2, \dots, N. \quad (3.2)$$

If all the elements in the array are in an open circuit condition, then

$$I_j = 0, j = 1, 2, \dots, N, \quad (3.3)$$

and from Equation (3.1), we have

$$V_j = V_{oj} = I_g Z_{jS}. \quad (3.4)$$

Substituting (3.2) and (3.4) into (3.1), we obtain

$$\begin{bmatrix} 1 + \frac{Z_{11}}{Z_L} & \frac{Z_{12}}{Z_L} & \dots & \frac{Z_{1N}}{Z_L} \\ \frac{Z_{21}}{Z_L} & 1 + \frac{Z_{22}}{Z_L} & \dots & \frac{Z_{2N}}{Z_L} \\ \vdots & \vdots & \ddots & \vdots \\ \frac{Z_{N1}}{Z_L} & \frac{Z_{N2}}{Z_L} & \dots & 1 + \frac{Z_{NN}}{Z_L} \end{bmatrix} \begin{bmatrix} V_1 \\ V_2 \\ \vdots \\ V_N \end{bmatrix} = \begin{bmatrix} V_{o1} \\ V_{o2} \\ \vdots \\ V_{oN} \end{bmatrix}. \quad (3.5)$$

Then, we use the vector/matrix notation as

$$\mathbf{Z}_0 = \begin{bmatrix} 1 + \frac{Z_{11}}{Z_L} & \frac{Z_{12}}{Z_L} & \dots & \frac{Z_{1N}}{Z_L} \\ \frac{Z_{21}}{Z_L} & 1 + \frac{Z_{22}}{Z_L} & \dots & \frac{Z_{2N}}{Z_L} \\ \vdots & \vdots & \ddots & \vdots \\ \frac{Z_{N1}}{Z_L} & \frac{Z_{N2}}{Z_L} & \dots & 1 + \frac{Z_{NN}}{Z_L} \end{bmatrix}, \quad (3.6)$$

and

$$\begin{aligned} \mathbf{V} &= [V_1 \quad V_2 \quad \dots \quad V_N]^T \\ \mathbf{V}_o &= [V_{o1} \quad V_{o2} \quad \dots \quad V_{oN}]^T, \end{aligned} \quad (3.7)$$

so that we have a compact expression

$$\mathbf{Z}_0 \mathbf{V} = \mathbf{V}_o. \quad (3.8)$$

In Equation (3.8), \mathbf{Z}_0 is the normalized impedance matrix and \mathbf{V}_o represents the open circuit voltages at the antenna terminals. Because \mathbf{Z}_0 is nonsingular, the element output voltages can be obtained from the open circuit voltages [4] as

$$\mathbf{V} = \mathbf{Z}_0^{-1} \mathbf{V}_o = (\mathbf{I}_{NN} + \mathbf{Z}_{NN} / Z_L)^{-1} \mathbf{V}_o. \quad (3.9)$$

Here, \mathbf{I}_{NN} is an $N \times N$ identity matrix and \mathbf{Z}_{NN} represents the symmetric $N \times N$ impedance matrix. Because \mathbf{Z}_{NN} is a complex valued matrix, we have

$$\mathbf{Z}_{NN} = \mathbf{R}_{NN} + j\mathbf{X}_{NN}, \quad (3.10)$$

where \mathbf{R}_{NN} is the resistance matrix, while \mathbf{X}_{NN} is the reactance matrix.

Eigensolution representation by Chaloupka [25] is an appropriate way for discussing the specific properties of dense arrays and details are shown as follows.

Since \mathbf{R}_{NN} and \mathbf{X}_{NN} are real symmetric matrices, their eigenvalues are real and the corresponding eigenvectors are mutually orthogonal. Furthermore, for a large class of antenna configurations which possess certain symmetry properties, the eigenvectors of \mathbf{R}_{NN} and \mathbf{X}_{NN} coincide. In case they disagree, eigenvectors of \mathbf{R}_{NN} and \mathbf{X}_{NN} can be forced to agree with each other by adding some reactive loading to the antenna ports. Without loss of generality, common eigenvectors of \mathbf{R}_{NN} and \mathbf{X}_{NN} are assumed here, such that the impedance matrix can be diagonalized, that is,

$$\mathbf{Z}_{NN} = \mathbf{U}_{NN} \cdot \mathbf{z}_N \cdot \mathbf{U}_{NN}^T, \quad (3.11)$$

where

$$\mathbf{z}_N = \text{diag}[z_1, z_2, \dots, z_N] \quad (3.12)$$

is composed of the N “modal impedances” and the unitary matrix

$$\mathbf{U}_{NN} = (\mathbf{u}_1, \mathbf{u}_2, \dots, \mathbf{u}_N) \quad (3.13)$$

is composed of the N orthonormal eigenvectors of \mathbf{Z}_{NN} .

From Equations (3.9) and (3.11), the element output voltages can be represented as

$$\mathbf{U}_{NN}^T \mathbf{V} = (\mathbf{I}_{NN} + \mathbf{z}_N / Z_L)^{-1} \mathbf{U}_{NN}^T \mathbf{V}_o. \quad (3.14)$$

Therefore, by means of this eigensolution, the array with mutually coupled ports is modelled by an equivalent set of N non-coupled antennas (modes), with

$$\begin{cases} \mathbf{v}_o = \mathbf{U}_{NN}^T \mathbf{V}_o \\ \mathbf{v} = \mathbf{U}_{NN}^T \mathbf{V} \end{cases} \quad (3.15)$$

as modal open circuit voltages and modal output voltages respectively.

The modal model provides a deep insight into the characteristic properties of multi-port antenna with reduced element spacing. It allows us to draw a basic conclusion about how increased mutual coupling impacts the properties of a dense multi-port antenna.

3.3 Properties of multi-port dense antenna array

The properties of an arbitrary N -element array with N ports terminated by the complex-valued load impedance Z_L have been characterized in [10] by relating the port voltages V_n to the electric field vector \mathbf{E}_{inc} of a plane wave impinging the array from a variable direction of arrival (DOA) (Θ, Φ) :

$$V_n = k \mathbf{C}_n(\Theta, \Phi) \cdot \mathbf{E}_{\text{inc}}. \quad (3.16)$$

Here, we denote coefficient k as

$$k = \lambda_0 \sqrt{\frac{\text{Re}\{Z_L\}}{4\pi Z_0}}, \quad (3.17)$$

where λ_0 and Z_0 denote free space wavelength and wave impedance respectively. With the particular choice of k in Equation (3.17), the power delivered to the load at port n becomes

$$P_n = \frac{\lambda^2}{4\pi} |\mathbf{C}_n(\Theta, \Phi)|^2 S_{\text{inc,cp}} \quad (3.18)$$

with $S_{\text{inc,cp}}$ as the incident co-polar radiation density. \mathbf{C}_n represents the complex-valued vector radiation pattern associated with port n , or the port pattern. The square of their magnitude equals to the angular dependent antenna gain, if we define the gain to include power reduction due to mismatch and crosstalk between the ports. What is important here is that the port pattern differs from the element pattern of a dense array, given the strong mutual coupling between different elements.

In the discussion of the properties of dense multi-port antennas, two aspects are of major interest, namely, the pattern correlation and the gain reduction.

The pattern correlation between different ports can be represented by utilizing an inner product defined as [10]

$$K_{ij} = \langle \mathbf{C}_i, \mathbf{C}_j \rangle = \frac{1}{4\pi} \oint \mathbf{C}_i^*(\Theta, \Phi) \cdot \mathbf{C}_j(\Theta, \Phi) d\Omega, \quad (3.19)$$

where $d\Omega$ denotes the element of solid angle. Therefore, $N \times N$ correlation matrix \mathbf{K} gives the entire set of correlation coefficients among N port patterns. Ideally when there is no cross talk and power matching at all ports and no dissipative losses, matrix \mathbf{K} simplifies into a unity matrix.

Accordingly, the gain reduction can be quantified as the gain reduction factor given by [10]

$$\eta_j = K_{jj}. \quad (3.20)$$

Here, η_j is in the range of $[0, 1]$ and characterizes the deviations from the ideal case for the port patterns. To discount the impact from gain reduction, the normalized cross-correlation coefficient k_{ij} between the patterns of ports i and j is defined as

$$\kappa_{ij} = \frac{|K_{ij}|}{\sqrt{K_{ii}K_{jj}}}. \quad (3.21)$$

This describes the similarity between different port patterns, in regards to the angular dependence of amplitude, phase and polarization.

The definition of port patterns of a multi-port antenna from Equation (3.16), the gain reduction factors from Equation (3.20) and the normalized cross-correlation from Equation (3.21) provide an appropriate formal framework to discuss the impact of mutual coupling on the antenna properties. In the following subsection, the eigenmode model is used to further discuss the properties of dense multi-port antennas.

3.3.1 Antenna properties by means of eigenmode models

As shown in the sections above, each N -port antenna possesses N mutually orthogonal modal patterns, even if the element spacing is reduced to values much smaller than $\lambda/2$. Therefore, the modal representation [10] will be further explored in this subsection to discuss the properties of dense multi-port antennas.

Figure 3.3 depicts the modal model for an N -port antenna in the receive mode, in which the antenna is represented by a set of N uncoupled antennas. Mode m ($m = 1, 2, \dots, N$) is defined to correspond to the excitation of the multi-port antenna which is

obtained by setting all modal voltages equal to zero except for voltage v_m . This leads to the specific set of driving voltages given by:

$$V_m = \mathbf{U}_{NN} \cdot (0, 0, \dots, v_m, \dots, 0)^T. \quad (3.22)$$

The corresponding modal pattern is denoted by $\mathbf{c}_m(\Theta, \Phi)$ and normalized to $\|\mathbf{c}_m\|=1$.

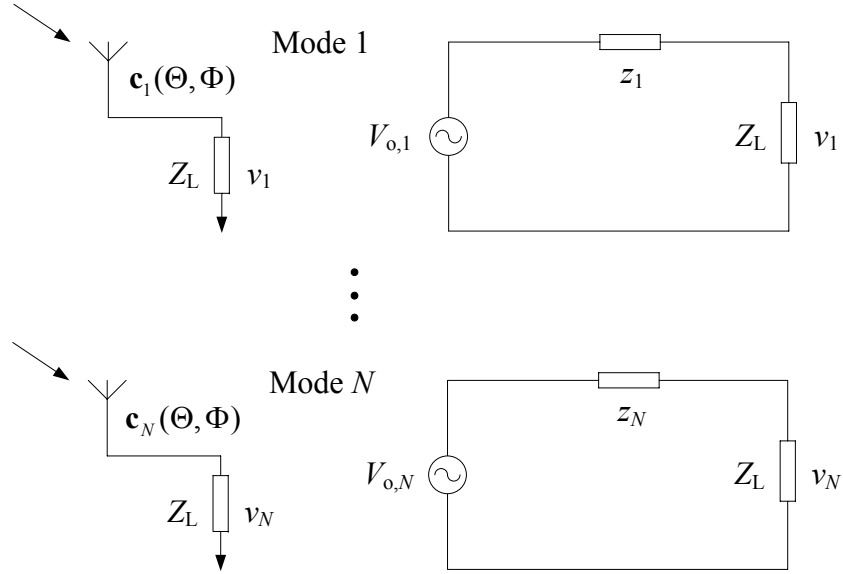


Figure 3.3 Mode model for multi-port antenna

As we assume no dissipative losses in the antenna structure, the principle of energy conservation enforces the so-defined eigen-radiation patterns to be mutually orthogonal [24, 41]. Thus, we have

$$\langle \mathbf{c}_m, \mathbf{c}_n \rangle = \delta_{mn}, \quad (3.23)$$

where δ_{mn} denotes the Kronecker delta function.

As in Equation (3.16) and (3.17), the modal source voltage and modal output voltages

of mode m become [10, 25]

$$\begin{cases} v_{o,m} = \lambda_0 \sqrt{\frac{\text{Re}\{z_m\}}{\pi Z_0}} \mathbf{c}_m(\Theta, \Phi) \cdot \mathbf{E}_{\text{inc}} \\ v_m = \frac{v_{o,m}}{1 + z_m / Z_L} = \frac{\lambda_0}{1 + z_m / Z_L} \sqrt{\frac{\text{Re}\{z_m\}}{\pi Z_0}} \mathbf{c}_m(\Theta, \Phi) \cdot \mathbf{E}_{\text{inc}} \end{cases}, \quad (3.24)$$

with the available power from mode m given by

$$p_{m,\text{avail}} = \frac{\lambda_0^2}{8\pi Z_0} |\mathbf{c}_m \cdot \mathbf{E}_{\text{inc}}|^2. \quad (3.25)$$

Here, we define the complex valued mismatch factor for mode m as

$$\Lambda_m = \frac{2\sqrt{\text{Re}\{z_m\} \text{Re}\{Z_L\}}}{z_m + Z_L}, \quad (3.26)$$

with $0 \leq |\Lambda_m|^2 \leq 1$, so that, the power delivered via the m -th eigen-radiation pattern to the load is given by

$$p_m = |\Lambda_m|^2 p_{m,\text{avail}}. \quad (3.27)$$

Moreover, with the definition of mismatch factors Λ_m , the radiation pattern for port n can be represented as a linear combination of the mutually orthogonal eigen radiation patterns of the array [10, 25]:

$$\mathbf{C}_n(\Theta, \Phi) = \sum_{m=1}^N u_{nm} \Lambda_m \mathbf{c}_m(\Theta, \Phi). \quad (3.28)$$

The expansion coefficients are given by the product of the elements u_{nm} of the unitary matrix \mathbf{U}_{NN} and the mismatch factors Λ_m , whereas u_{nm} depends on the array structure and Λ_m are functions of the load impedance. Therefore, for arrays with mutually coupled ports, the port radiation patterns depend on the choice of the load impedance Z_L .

Thus, the gain reduction factor at port n becomes [10, 25]

$$\eta_{\text{port},n} = \frac{1}{4\pi} \oint |\mathbf{C}_n|^2 d\Omega = \sum_{m=1}^N |\Lambda_m|^2 |u_{nm}|^2. \quad (3.29)$$

This gain reduction factor includes the effect of non-vanishing cross-talk between different ports as well as mismatch at the ports. Since

$$\sum_{m=1}^N |u_{nm}|^2 = 1, \quad (3.30)$$

$\eta_{\text{port},n}$ approaches unity if all mismatch factors are equal to one. Similarly, we have

$$\kappa_{ij} = \frac{|K_{ij}|}{\sqrt{K_{ii}K_{jj}}} = \frac{\sum_{m=1}^N |\Lambda_m|^2 u_{mi}^* u_{mj}}{\sqrt{(\sum_{m=1}^N |\Lambda_m|^2 |u_{mi}|^2)(\sum_{m=1}^N |\Lambda_m|^2 |u_{mj}|^2)}}. \quad (3.31)$$

If all mismatch factors approach unity (i.e. perfect matching to all modes), the N port radiation patterns would be uncorrelated, due to the orthonormality of the rows of matrix \mathbf{U}_{NN} .

Equations (3.27) to (3.31) turn out to be the key for understanding the impact of mutual coupling on the properties of a dense multi-port antenna. With increasing mutual coupling, the deviation between the modal impedances increases. Since the modal impedances are different from each other, while the load impedances are equal, simultaneous matching of all modes is not possible. Therefore, the non-unity mismatching factors Λ_m lead to the port gain reduction and inter-port cross correlation.

3.4 DBF in multi-port dense antenna array

The digital beam forming (DBF) can be represented via a linear combination of the N modal radiation patterns of the antennas [25]:

$$\mathbf{C}_{\text{DBF}}(\Theta, \Phi) = \sum_{m=1}^N w_m^* \mathbf{c}_m(\Theta, \Phi), \quad (3.32)$$

As shown from Equation (3.28), the modal output signals are weighted in an unwanted manner by the mismatch factors Λ_m . This unwanted weighting can be numerically compensated for in DBF by using the modified modal weights:

$$\tilde{w}_m = k w_m / \Lambda_m^*. \quad (3.33)$$

Here, k is an arbitrarily-defined constant.

This type of compensation can be considered as “compensation for the effects of mutual coupling” in digital processing and has already been discussed in a variety of references [4, 19, 20, 42, 43]. The port weights, which are more accessible to signal processing part, can be obtained [25] via:

$$\mathbf{W} = (W_1, W_2, \dots, W_N)^T = k \mathbf{U}_{NN} \mathbf{d}_{NN} \mathbf{w}. \quad (3.34)$$

Here,

$$\mathbf{d}_{NN} = \text{diag}\left[\frac{1}{\Lambda_1^*}, \frac{1}{\Lambda_2^*}, \dots, \frac{1}{\Lambda_N^*}\right] \quad (3.35)$$

and

$$\mathbf{w} = (w_1, w_2, \dots, w_N)^T \quad (3.36)$$

denotes the modal weights.

The constant k can be determined if

$$\mathbf{W}^H \mathbf{W} = 1 \quad (3.37)$$

is to be enforced, so that we get

$$\eta_{\text{DBF}} = k^2 = \frac{\sum_{m=1}^N |w_m|^2}{\sum_{m=1}^N |w_m|^2 / |\Lambda_m|^2}. \quad (3.38)$$

η_{DBF} gives the effective gain reduction of a multi-port dense antenna. Maximum gain reduction occurs if the highest weight $|w_m|$ is allocated to the modal pattern m with the strongest mismatch, or the lowest $|\Lambda_m|$.

In case of receiver systems, the modal voltages due to a strongly mismatched mode are typically much weaker than the modal voltages corresponding to well-matched modes. DBF is able to “numerically amplify” the modal voltages by employing a higher weight. However, this changes the effective load for each mode and therefore, makes the noise matching impossible [24].

In case of transmitter systems, a higher weight can also be used to compensate for the strong reflection due to mode mismatching. The cost is that the delivered power will be increased by a factor of $1/\eta_{\text{DBF}}$ in order to end up with to the same radiated power density in the far field.

Except for these results obtained from the mode model, this method also sheds light on how we can proceed to address the pattern correlation and gain reduction simultaneously within multi-port dense antenna arrays. Note that, from Equation (3.38), we can find that if all array modes are matched to the load at the same time while the radiation pattern remains the same in terms of amplitude, phase and polarization on the DOA, the absolute value of the amplitude for all DOA increases by a factor of $1/\sqrt{\eta_{\text{DBF}}}$.

In the next section, a general theory about the decoupling network (DN) will be introduced.

3.5 DN for multi-port dense antenna array

Since strong mutual coupling exists within dense multi-port antennas, if all modes are terminated with the same load Z_L , non-correlated radiation patterns can only be achieved at the cost of a reduced effective antenna gain, which, therefore, requires a higher transmitted power in transmitting systems or degrades the signal-to-noise ratio (SNR) in receiving systems.

A solution to this problem is to use an RF network to transform the N parallel load impedances Z_L into a set of different impedances [23-25], which will match the different modal impedances, respectively.

Figure 3.4 gives a general idea of such a decoupling network. The left shows a dense multi-port antenna with decoupling network, and the right shows the effective circuits for different modes. These effective circuits differ for each mode, so that at the load point, different modal impedances are all converted into the same, which achieve the power or noise matching, depending on the application. To avoid energy consumption, the decoupling network should be a lossless $2N$ -port network with N -input and N -output ports. It transforms the N modal impedance with impedance matrix \mathbf{z}_N into a new modal impedance matrix $\tilde{\mathbf{z}}_N$, so that it is the conjugate of the load impedance matrix $\mathbf{Z}_L = \text{diag}[\underbrace{Z_L, Z_L, \dots, Z_L}_N]$, that is,

$$\tilde{\mathbf{z}}_N = \mathbf{Z}_L^* = \text{diag}[\underbrace{Z_L, Z_L, \dots, Z_L}_N]^* . \quad (3.39)$$

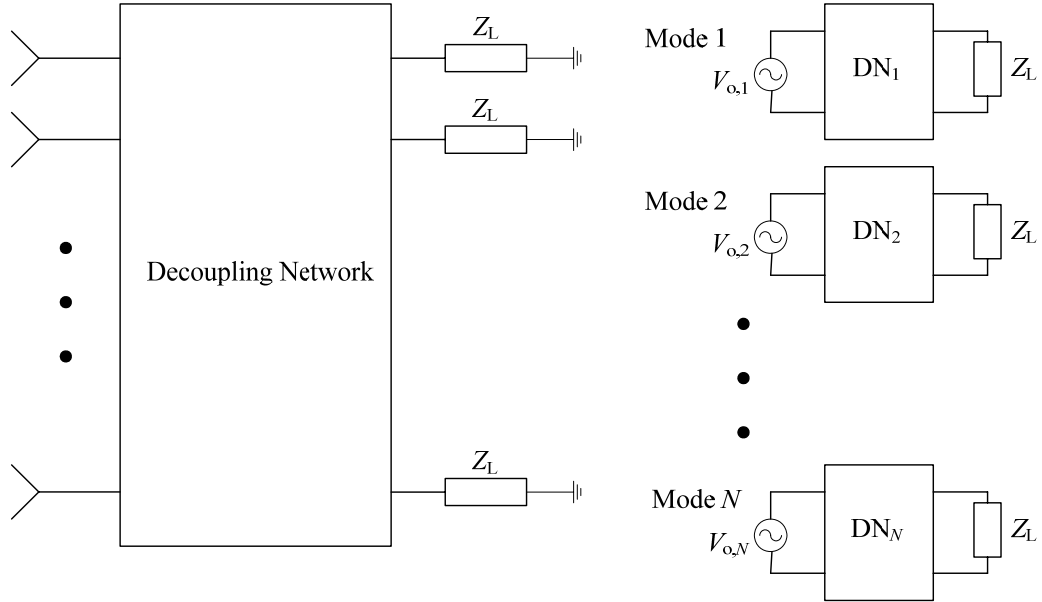


Figure 3.4 Dense multi-port antennas with DN

It has been assumed in the previous section that the array impedance matrix \mathbf{Z}_{NN} can be transformed into a diagonal matrix \mathbf{z}_N by means of a unitary matrix \mathbf{U}_{NN} . This requires the eigenvectors of \mathbf{R}_{NN} and \mathbf{X}_{NN} to coincide. For a class of antenna structures where certain symmetry conditions are met, this statement holds, but it is not always so. In a more general case, the following procedure described in [25] can be applied to obtain an impedance matrix $\tilde{\mathbf{Z}}_{NN}$ which can be represented by Equation (3.11):

- 1) Since $\mathbf{Y}_{NN} = \mathbf{Z}_{NN}^{-1} = \mathbf{G}_{NN} + j\mathbf{B}_{NN}$, the real and symmetric conductance matrix is determined and diagonalized as

$$\mathbf{G}_{NN} = \mathbf{U}_{NN} \cdot \mathbf{g} \cdot \mathbf{U}_{NN}^T . \quad (3.40)$$

2) In case the eigenvectors of \mathbf{G}_{NN} do not agree with the eigenvectors of \mathbf{B}_{NN} , a shunt network $\mathbf{B}_{\text{shunt}}$ composed of susceptances is connected between antenna ports, so that the new susceptance matrix

$$\tilde{\mathbf{B}}_{NN} = \mathbf{B}_{NN} + \mathbf{B}_{\text{shunt}} \quad (3.41)$$

has the same eigenvectors as \mathbf{G}_{NN} .

3) Then the new impedance matrix

$$\tilde{\mathbf{Z}}_{NN} = (\mathbf{G}_{NN} + j\tilde{\mathbf{B}}_{NN})^{-1} = \mathbf{U}_{NN} \cdot \tilde{\mathbf{z}} \cdot \mathbf{U}_{NN}^T \quad (3.42)$$

has the properties which were assumed throughout the previous sections.

4) The shunt network $\mathbf{B}_{\text{shunt}}$ can be merged with a shunt network from the decoupling and matching network.

There are different realizations for a DN [27]. If a ladder type is chosen, the synthesis can be derived from conventional 2-port network synthesis. The fundamental theory in the DN realization is that, while series reactances jx_{series} are common to all two-ports, shunt susceptances $jb_{\text{shunt},m}$ are different for each mode. Therefore, different modal impedance matching simultaneously is made possible.

A possible topology of the DN for a two-port antenna in [25] is given in Figure 3.5. Ports 1 and 2 are antenna ports, while ports 1' and 2' are the newly formed ports from the decoupling network.

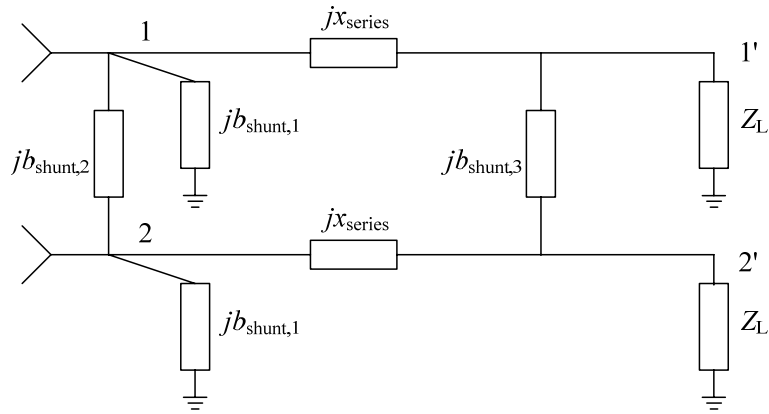


Figure 3.5 DN for a two-port antenna

In the simplest case, i.e. with a minimum number of sections, the decoupling condition is enforced at the centre frequency only. With additional sections, the decoupling frequency bandwidth can be increased. However, with an increase in the decoupling network sections n_s , a saturation effect with the bandwidth improvement will occur [44, 45].

3.6 DN design and realization

3.6.1 DN for 3-port antenna array

An array of three monopoles was fabricated to verify the model [28]. Figure 3.6 shows the 3-element array, where each monopole element has a length that is quarter of a wavelength and the inter-element spacing is a tenth of a wavelength. Table 3.1 summarizes the parameters of the array [28]. The inter-element spacing is very small compared to the conventional half-wavelength element spacing. This small element spacing results in strong mutual coupling between elements of the array. The performance of the array, in terms of power matching and signal-to-noise-ratio (SNR), is affected by the mutual coupling between the array elements. The admittance

parameters of the array are $Y_{11} = 0.0406 \angle -77.8^\circ$ and $Y_{12} = 0.0203 \angle 92.2^\circ$.

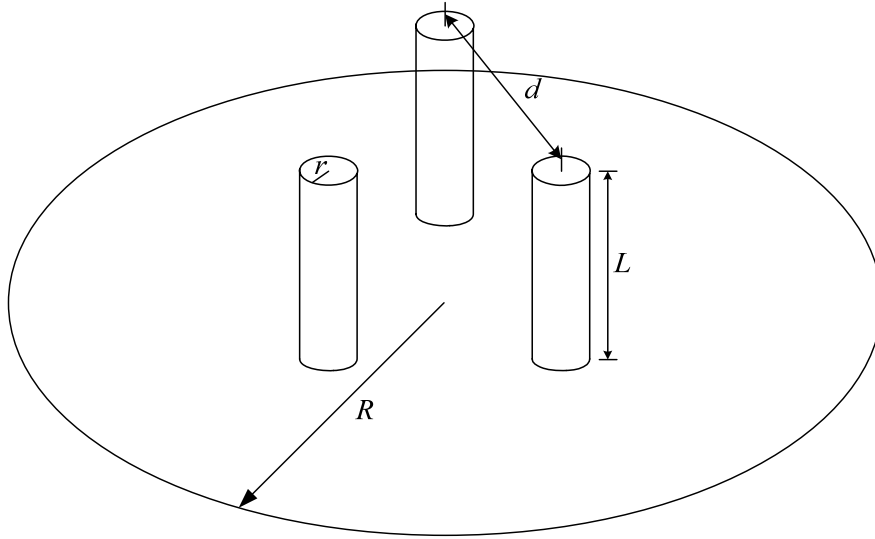


Figure 3.6 A 3-element monopole array

Table 3.1 Dimensions of the 3-element monopole array

Operational frequency f_0	2.45 GHz
Monopole length L	30.6 mm
Monopole radius r	3 mm
Array element spacing d	12.5 mm
Ground radius R	18 cm

The proposed lossless decoupling network for a 3-element array in [28] is shown in Figure 3.7. The decoupling network consists of a series section with components jX_1 and a parallel section with components jB_2 . Two analysis approaches can be used to compute the components of the decoupling network. The first approach is the eigenmode analysis while the second is the network analysis.

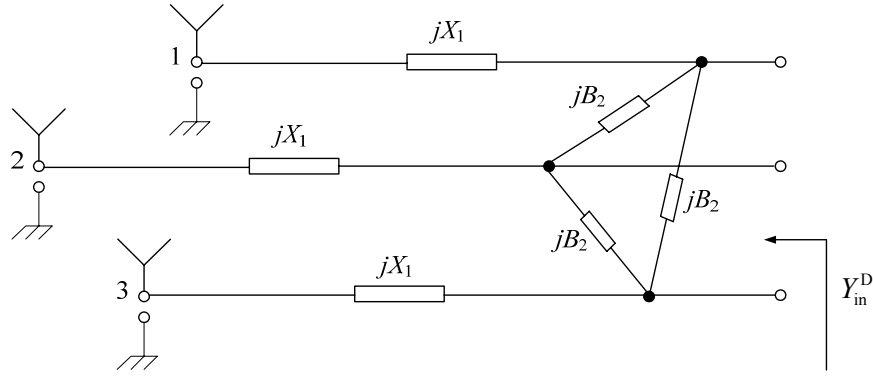


Figure 3.7 A generalized DN for a 3-element array

3.6.1.1 Eigenmode analysis

Due to symmetry, the admittance matrix of the three-element array is given by

$$\mathbf{Y} = \begin{bmatrix} Y_{11} & Y_{12} & Y_{12} \\ Y_{12} & Y_{11} & Y_{12} \\ Y_{12} & Y_{12} & Y_{11} \end{bmatrix}. \quad (3.43)$$

The eigenvalues of the admittance matrix (modal admittances) are:

$$\begin{aligned} Y_A &= Y_{11} + 2Y_{12}; \\ Y_B &= Y_C = Y_{11} - Y_{12}. \end{aligned} \quad (3.44)$$

The equivalent circuits for different modes [24] are shown in Figure 3.8. The series component is simply jX_1 . From two-port network theory, the admittance matrix of the parallel section of the decoupling network, as shown in Figure 3.7, can be obtained and is given by

$$\mathbf{Y}_{\text{DN,p}} = \begin{bmatrix} j2B_2 & -jB_2 & -jB_2 \\ -jB_2 & j2B_2 & -jB_2 \\ -jB_2 & -jB_2 & j2B_2 \end{bmatrix}. \quad (3.45)$$

Since $Y_{11}^{\text{DN,p}} + 2Y_{12}^{\text{DN,p}} = 0$, there is no parallel component in the equivalent circuit for mode A. For mode B or C, the parallel component can be computed as

$$Y_{11}^{\text{DN,p}} - Y_{12}^{\text{DN,p}} = j3B_2.$$

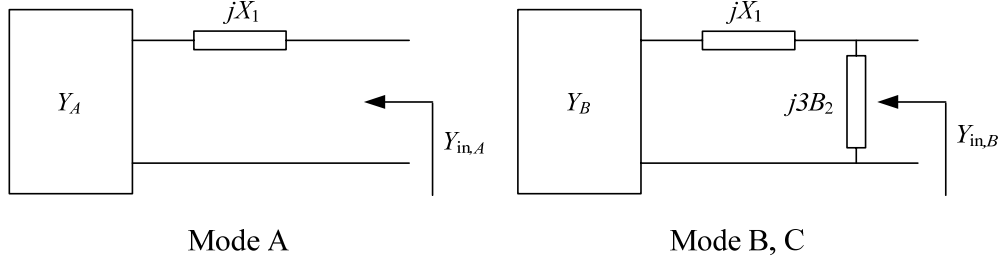


Figure 3.8 Equivalent circuits for different modes of 3-element array

Therefore, the equivalent modal admittances are:

$$Y_{in,A} = \left(\frac{1}{Y_A} + jX_1 \right)^{-1}, \quad (3.46)$$

$$Y_{in,B} = Y_{in,C} = \left(\frac{1}{Y_B} + jX_1 \right)^{-1} + j3B_2. \quad (3.47)$$

In this eigenmode analysis, the decoupling network decouples the ports of the array by matching all the mode admittances. From Equations (3.46) and (3.47), X_1 and B_2 can be obtained by numerically solving the following set of nonlinear simultaneous equations:

$$\begin{cases} \text{Re}[Y_{in,A}] = \text{Re}[Y_{in,B}] \\ \text{Im}[Y_{in,A}] = \text{Im}[Y_{in,B}] \end{cases}. \quad (3.48)$$

The analytical results or numerical results for X_1 and B_2 can be obtained using Mathematical tools such as Mathematica [46] or Matlab [47].

3.6.1.2 Network analysis

The following impedance and admittance matrices [28] describe the series and parallel sections of the decoupling network shown in Figure 3.7 respectively:

$$\mathbf{Z}_{\text{DN},s} = \begin{bmatrix} jX_1 & 0 & 0 \\ 0 & jX_1 & 0 \\ 0 & 0 & jX_1 \end{bmatrix}, \quad (3.49)$$

$$\mathbf{Y}_{\text{DN},p} = \begin{bmatrix} j2B_2 & -jB_2 & -jB_2 \\ -jB_2 & j2B_2 & -jB_2 \\ -jB_2 & -jB_2 & j2B_2 \end{bmatrix}. \quad (3.50)$$

The admittance matrix of the decoupled array can be written as:

$$\mathbf{Y}_{\text{in}}^{\text{D}} = \left(\mathbf{Y}_{\text{array}}^{-1} + \mathbf{Z}_{\text{DN},s} \right)^{-1} + \mathbf{Y}_{\text{DN},p}. \quad (3.51)$$

For decoupling to be achieved, the mutual admittance of the decoupled system, Y_{12}^{D} , should be zero. Solutions for X_1 and B_2 are obtained by solving the following set of nonlinear simultaneous equations:

$$\begin{cases} \text{Re}[Y_{12}^{\text{D}}] = 0 \\ \text{Im}[Y_{12}^{\text{D}}] = 0 \end{cases}. \quad (3.52)$$

The solutions are again obtained using Mathematical tools such as Mathematica or Matlab. It has been verified that solutions thus obtained are consistent with those obtained from the eigenmode analysis.

3.6.1.3 Matching network

The decoupled antenna array can easily be matched to any desired impedance, since the impedances looking into each port of the array are now identical. An L -network topology described by Pozar in [48], consisting of a shunt and series component, can be used for matching as shown in Figure 3.9.

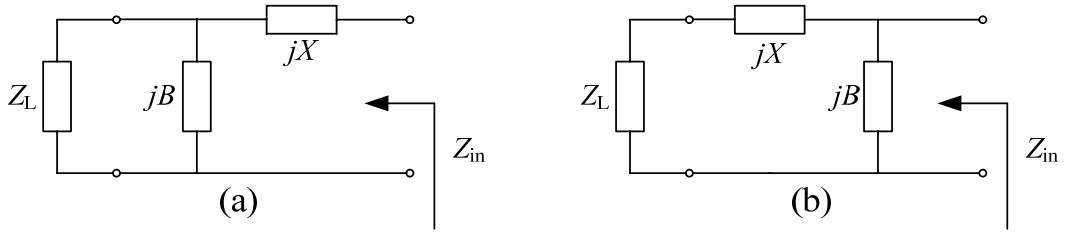


Figure 3.9 L section matching networks for cases where (a) $R_L > R_{in}$ and (b) $R_L < R_{in}$

Consider the network of Figure 3.9(a) and let $Z_L = R_L + jX_L$. The impedance seen looking into the matching network must be equal to $Z_{in} = R_{in} + jX_{in}$. Thus

$$R_{in} + jX_{in} = jX + \frac{1}{jB + 1/(R_L + jX_L)}. \quad (3.53)$$

Rearranging (3.53) and separating into real and imaginary parts gives two equations for the two unknowns X and B , which can be solved to give [48]

$$B = \frac{X_L \pm \sqrt{R_L/R_{in}} \sqrt{R_L^2 + X_L^2 - R_{in}R_L}}{R_L^2 + X_L^2}, \quad (3.54)$$

$$X = \frac{1}{B} + \frac{X_L R_{in}}{R_L} - \frac{R_{in}}{B R_L} + X_{in}.$$

Two solutions are possible for B and X . Both positive and negative values of B and X are possible (positive $X \equiv$ inductor, negative $X \equiv$ capacitor, positive $B \equiv$ capacitor, negative $B \equiv$ inductor). Therefore, both solutions are physically realizable. However, one solution may result in significantly smaller values for the reactive components and may be the preferred solution because it results in larger bandwidth.

Consider the network of Figure 3.9(b), which is used when $R_L < R_{in}$. The admittance seen looking into the matching network must be equal to $Y_{in} = G_{in} + jB_{in} = 1/Z_{in}$. Thus

$$G_{in} + jB_{in} = jB + \frac{1}{R_L + j(X + X_L)}. \quad (3.55)$$

Rearranging and separating into real and imaginary parts again give two equations for

the two unknowns X and B , which can be solved to give [48]

$$\begin{aligned} X &= \pm \sqrt{R_L (1/G_{in} - R_L)} - X_L, \\ B &= \pm G_{in} \sqrt{(1/G_{in} - R_L)/R_L} + B_{in}. \end{aligned} \quad (3.56)$$

In the case of matching the decoupled array, $Z_L = 1/Y_{11}^D$. In general, for matching to, for example, a system with Z_{in} equals 50Ω , the values for B and X can be found by Equations (3.54) or (3.56).

The completed array with decoupling and matching network [28] (case of Figure 3.9(a)) is shown in Figure 3.10.

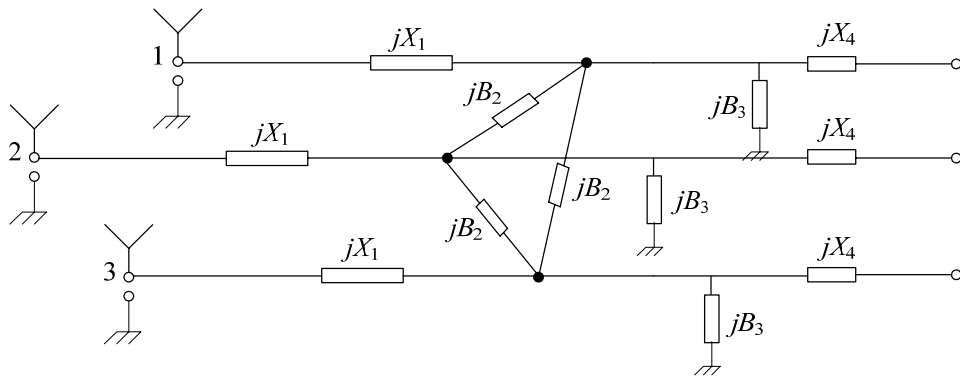


Figure 3.10 A 3-element array with decoupling and matching network

The decoupling and matching network contains only lossless components such as inductors or capacitors. There exists two possible decoupling network configurations for an array, and for each decoupling network two possible configurations can be used as matching network. One possible configuration [28] of the calculated decoupling and matching network at 2.45 GHz is shown in Table 3.2.

Table 3.2 Decoupling network and matching network configurations

Decoupling network		Matching network	
Series	Parallel	Shunt	Series
$L = 0.164 \text{ nH}$	$C = 1.149 \text{ pF}$	$C = 0.57 \text{ pF}$	$L = 4.41 \text{ nH}$
		$L = 6.29 \text{ nH}$	$C = 0.96 \text{ pF}$

3.6.1.4 DN implementation and measurement results

The decoupling and matching networks designed in the previous section are based on lossless capacitors and inductors. These ideal lumped capacitors and inductors have to be converted to realizable forms. One convenient way of realizing the decoupling and matching networks is in microstrip or stripline. Kuroda's identities [48-51] are applied to transform the lumped components into microstrip or stripline stubs. Table 3.3 [28] summarizes the realization of the ideal capacitors and inductors as microstrip stubs, with the corresponding equations required for the transformations.

Pictures of the array elements with supporting structure and the microstrip decoupling circuit in [28] are shown in Figures 3.11 and 3.12. The array elements are gold-plated brass rods. The supporting structure is made of aluminum. The circular plate acts as a large ground plane for the array. The material used for the microstrip decoupling and matching networks is Rogers RT/duroid 5880 substrate with dielectric constant of $\epsilon_r = 2.2$, thickness of 31 mil and loss tangent of 0.0009. In designing the layout of the microstrip network, the lines were meandered to reduce the size of the overall network. Meandering of the lines does not affect the performance of the network as long as the effective length of the curved lines is equivalent to the original length of the straight microstrip lines. The network was mounted on the underside of the metal

block in the supporting structure.

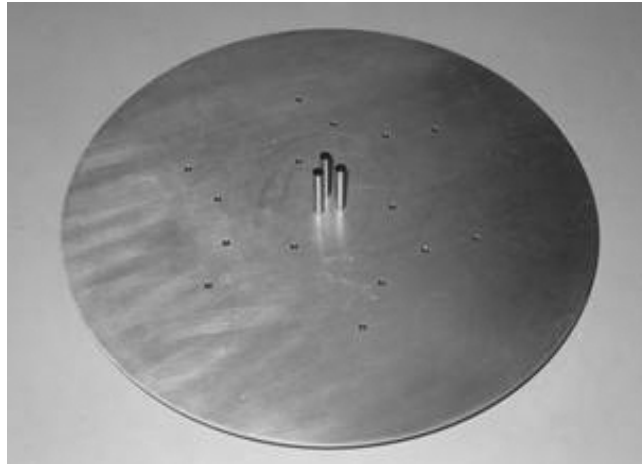


Figure 3.11 The 3-element array with supporting structure [28]

Table 3.3 Transformation of ideal components to microstrip stubs.

Initial network	Transformed network	Design equations
		$\theta^{sc} = \tan^{-1} \left(\frac{\omega L}{2Z_0 + L} \right) \pm \frac{\pi}{2}$ $Z_1 = Z_0 + \frac{L}{2}$
		$\theta^{sc} = \tan^{-1} \left(\frac{\omega}{1 - 2Z_0\omega^2 C} \right) \pm \frac{\pi}{2}$ $Z_1 = Z_0 - \frac{1}{2\omega^2 C}$
		$\theta^{sc} = \tan^{-1} \left(\frac{\omega L}{Z_0} \right)$
		$\theta^{sc} = \tan^{-1} (\omega C Z_0) \pm \frac{\pi}{2}$

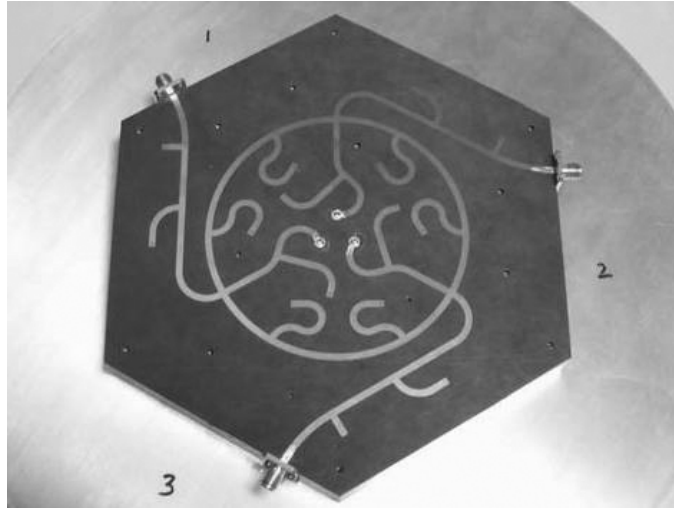


Figure 3.12 Photo of microstrip network [28]

The measured and simulated results [28] of the array to be decoupled in are shown in Figures 3.13 and 3.14.

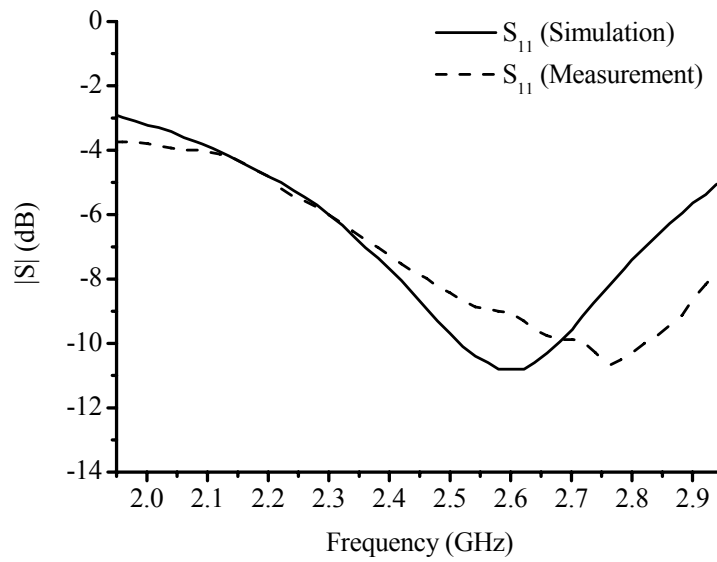


Figure 3.13 Simulated and measured S_{11} of array to be decoupled

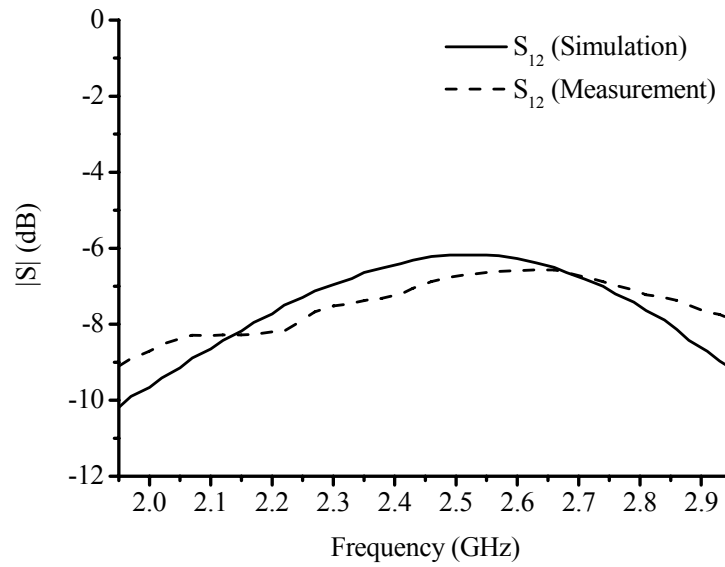


Figure 3.14 Simulated and measured S_{12} of array to be decoupled

The array with its decoupling and matching network was measured and the results were compared to those obtained from theoretical simulations [28]. The measured and simulated results are in close agreement with only slight shift in the frequency response. As shown in Figures 3.15 and 3.16, the array has successfully been decoupled since it has a low value of S_{12} (below -15 dB) over the frequency range considered. The array is also matched with a reflection coefficient of about -15 dB at the minimum of the S_{11} curve.

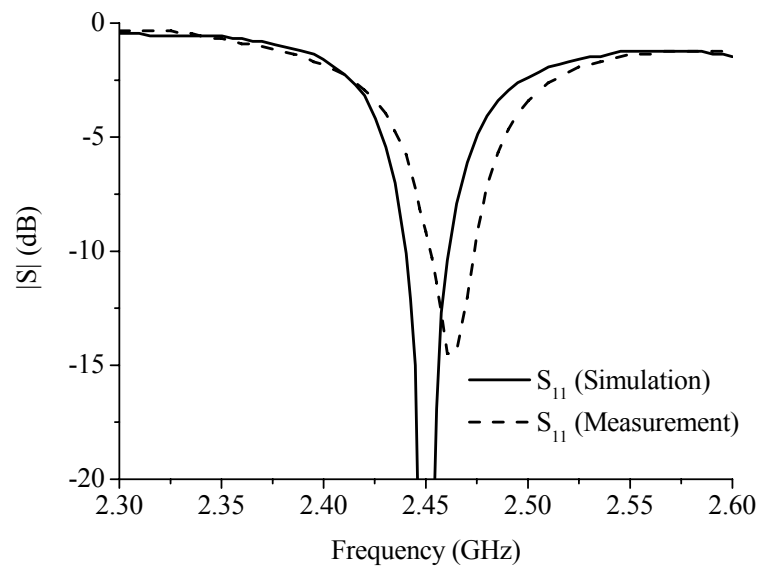


Figure 3.15 Simulated and measured S_{11} of the decoupled and matched array

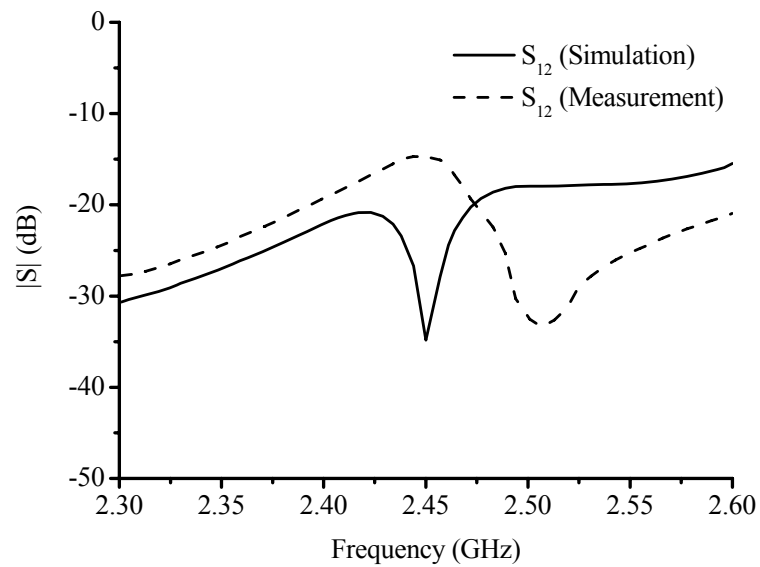


Figure 3.16 Simulated and measured S_{12} of the decoupled and matched array

3.6.2 DN for 4-port antenna array by eigenmode analysis

An array of 4 elements was designed and decoupled to verify the modal model [29].

The array was designed based on the aperture-coupled patch antenna, as shown in

Figure 3.17. Rogers RT/duroid 5870 with dielectric constant of $\epsilon_r = 2.33$, thickness of 3.175 mm and loss tangent of 0.0021 was used as the substrate of the antenna, while RO4003 with dielectric constant of $\epsilon_r = 3.38$, thickness of 0.508 mm and loss tangent of 0.0021 was used as the substrate of the feed network part. The three-layer structure makes it possible to separate the antenna design and decoupling/matching network realization on two semi-isolated layers. The dimensions of the array element [29] are shown in Table 3.4.

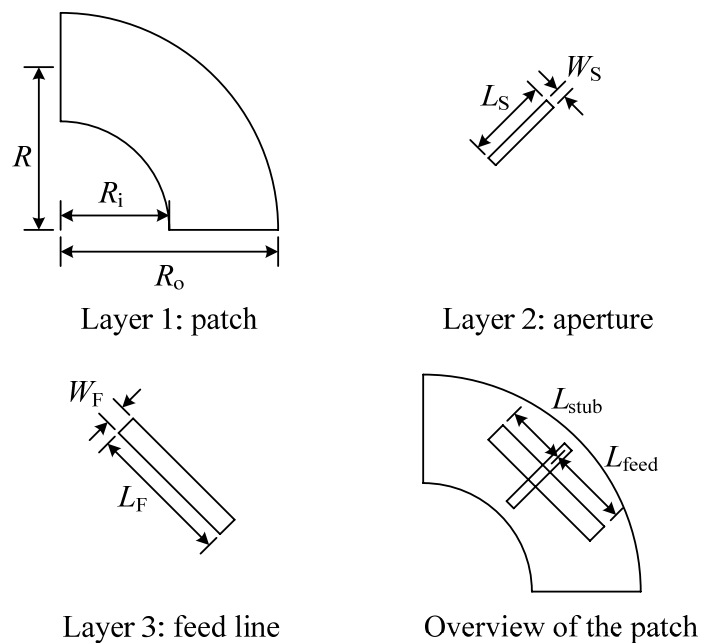


Figure 3.17 Single aperture-coupled ring patch

Four identical elements are placed closely with a gap of 2 mm between neighbouring elements to form the array in [29], as shown in Figure 3.18. Due to the strong mutual coupling, fine tuning is performed to improve the performance of the array and the S-parameters are shown in Figure 3.19. It can be seen that although the reflected power at the input port can be made quite low, the incident power actually goes back to the circuit through other ports because of the mutual coupling.

Table 3.4 Dimensions of the aperture-coupled ring patch

Operational frequency f_0	2.45 GHz
Median radius R	23.16 mm
Width of the ring R_o-R_i	18.65 mm
Length of the aperture L_S	15 mm
Width of the aperture W_S	1 mm
Length of the feed line L_F	2 mm
Width of the feed line W_F	2 mm
Length of the tuning stub L_{stub}	5.5 mm

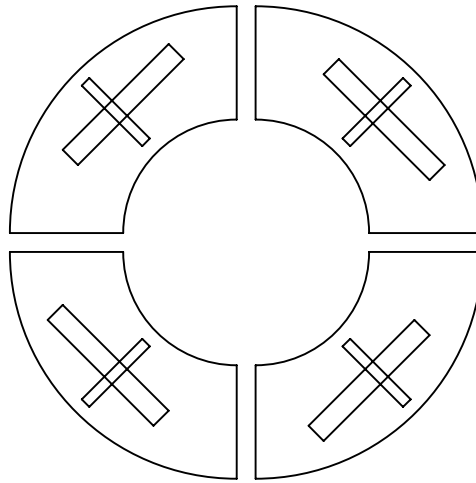


Figure 3.18 Four-element aperture-coupled ring patch array

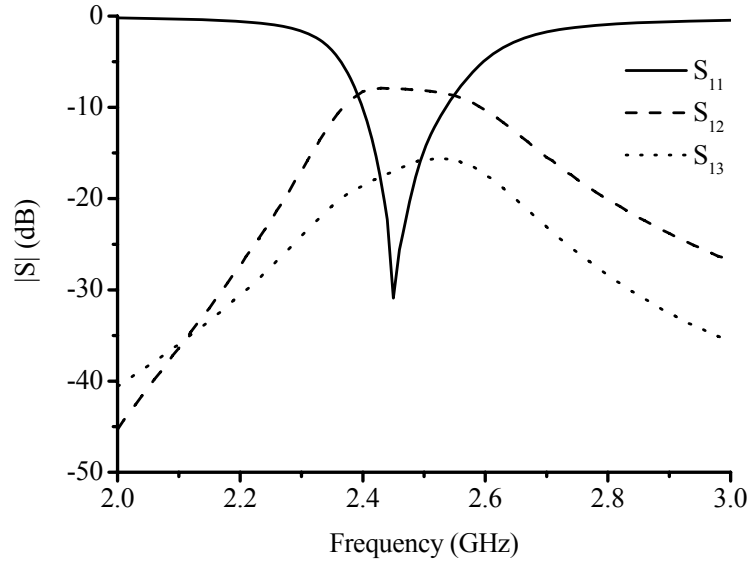


Figure 3.19 S-Parameters of the optimized array

3.6.2.1 Eigenmode analysis

To decouple the array, the modal representation described in Section 3.2 was used in [29]. The four-element array can be represented in terms of different eigenmodes. Due to the symmetry of the above array, its admittance matrix can be represented as

$$\mathbf{Y}_{4,4} = \begin{bmatrix} Y_{11} & Y_{12} & Y_{13} & Y_{12} \\ Y_{12} & Y_{11} & Y_{12} & Y_{13} \\ Y_{13} & Y_{12} & Y_{11} & Y_{12} \\ Y_{12} & Y_{13} & Y_{12} & Y_{11} \end{bmatrix} \quad (3.57)$$

It can be diagonalized as

$$\mathbf{Y}_{4,4} = \mathbf{U}_{4,4} \cdot \mathbf{y}_4 \cdot \mathbf{U}_{4,4}^T, \quad (3.58)$$

where

$$\mathbf{U}_{4,4} = 0.5 \begin{bmatrix} 1 & 1 & 1 & 1 \\ 1 & 1 & -1 & -1 \\ 1 & -1 & -1 & 1 \\ 1 & -1 & 1 & -1 \end{bmatrix}, \quad (3.59)$$

and

$$\mathbf{y}_4 = \begin{bmatrix} y_1 & 0 & 0 & 0 \\ 0 & y_2 & 0 & 0 \\ 0 & 0 & y_3 & 0 \\ 0 & 0 & 0 & y_4 \end{bmatrix}. \quad (3.60)$$

Here, y_i ($i = 1, 2, 3$ or 4) represents the i th eigenvalue (modal admittance) of the array, given as following:

$$\begin{cases} y_1 = Y_{11} + 2Y_{12} + Y_{13} \\ y_2 = y_3 = Y_{11} - Y_{13} \\ y_4 = Y_{11} - 2Y_{12} + Y_{13} \end{cases}. \quad (3.61)$$

In the case that the impedance matrix is of concern, we can also follow the same procedure as above. These two approaches are related by

$$\mathbf{Z}_{4,4} = \mathbf{U}_{4,4} \cdot \mathbf{y}_4^{-1} \cdot \mathbf{U}_{4,4}^T. \quad (3.62)$$

It can be seen from Equation (3.61) that it is impossible to match the four modal admittances to the load at the same time. Therefore, a decoupling network is going to be implemented to transform the modal admittances to equal values.

Figure 3.20 gives one possible structure of DN [29]. In this figure, four kinds of two-port networks are represented by four types of reactive elements, namely jB_{p1} , jB_0 , jB_{p2} and jB_m . The entire structure will be fed through the newly formed ports (1', 2', 3' and 4') instead of the original ports 1, 2, 3 and 4.

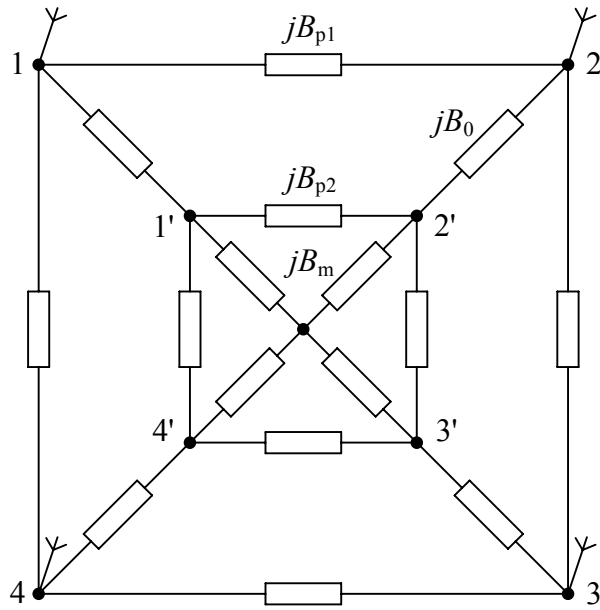


Figure 3.20 DN topology for 4-port array [29]

Before calculating the values of the reactive elements, a lemma which will be used in the design, was proved [29]. As shown in Figure 3.21, with a fixed reactive element jB_0 , for a set of circuits which have a constant conductance at the $A-A'$ reference plane, that is the real part of y' is equal to a constant value C , the conductance G and susceptance B of the admittance y should lie on a circle centered at $(B_0^2/2C, -B_0)$ with a radius of $B_0^2/2C$ in the (G, B) plane. This statement is proved as follows:

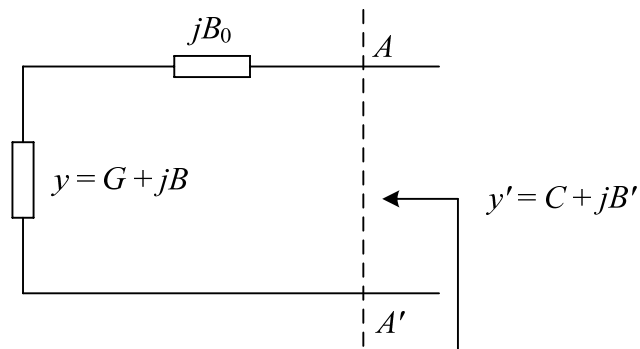


Figure 3.21 General circuit for the lemma

From the circuit theory, it can be stated that

$$\begin{aligned} y' = C + jB' &= \frac{(G + jB)jB_0}{G + j(B + B_0)} \\ &= \frac{(G + jB)jB_0[G - j(B + B_0)]}{G^2 + (B + B_0)^2}. \end{aligned} \quad (3.63)$$

Equating the real and imaginary parts at both sides of Equation (3.63), respectively, gives

$$\begin{cases} \frac{GB_0^2}{G^2 + (B + B_0)^2} = C \\ \frac{G^2B_1 + B^2B_0 + BB_0^2}{G^2 + (B + B_0)^2} = B' \end{cases}. \quad (3.64)$$

Therefore, we have

$$\left(G - \frac{B_0^2}{2C}\right)^2 + (B + B_0)^2 = \left(\frac{B_0^2}{2C}\right)^2. \quad (3.65)$$

Equation (3.65) shows that G and B is on the circle centered at $(B_0^2/2C, -B_0)$ with a radius of $B_0^2/2C$, as shown in Figure 3.22. Therefore, the lemma is proved and will be used in the design of the decoupling network.

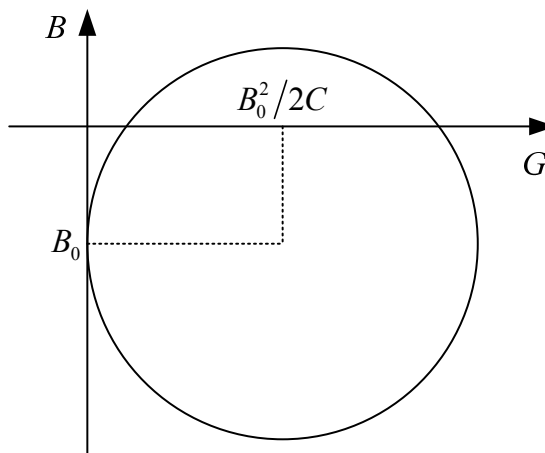
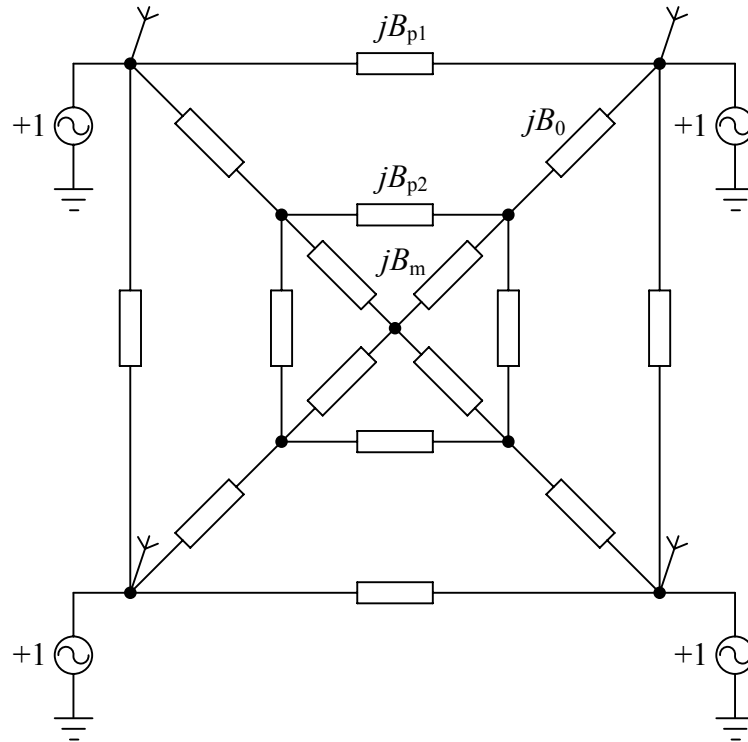
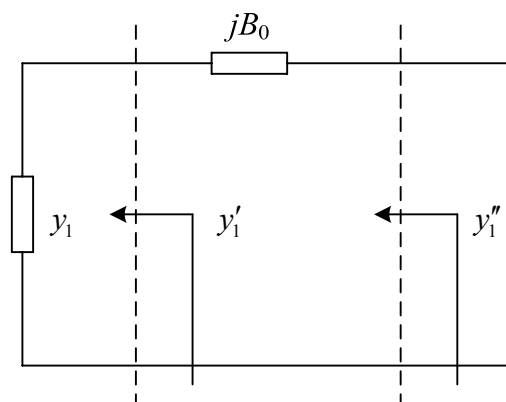


Figure 3.22 The circle defined by Equation (3.66) on GB plane

From the topology depicted in Figure 3.20, equivalent circuits for the three different modes differ from each other and were studied in [29]. Figures 3.23, 3.24 and 3.25 show the equivalent circuits for Mode 1, 2 & 3 and 4 with the DN respectively. The sub-figure (a) gives the mode voltage applied to excite a corresponding mode, while sub-figure (b) shows the simplified equivalent circuit accordingly.

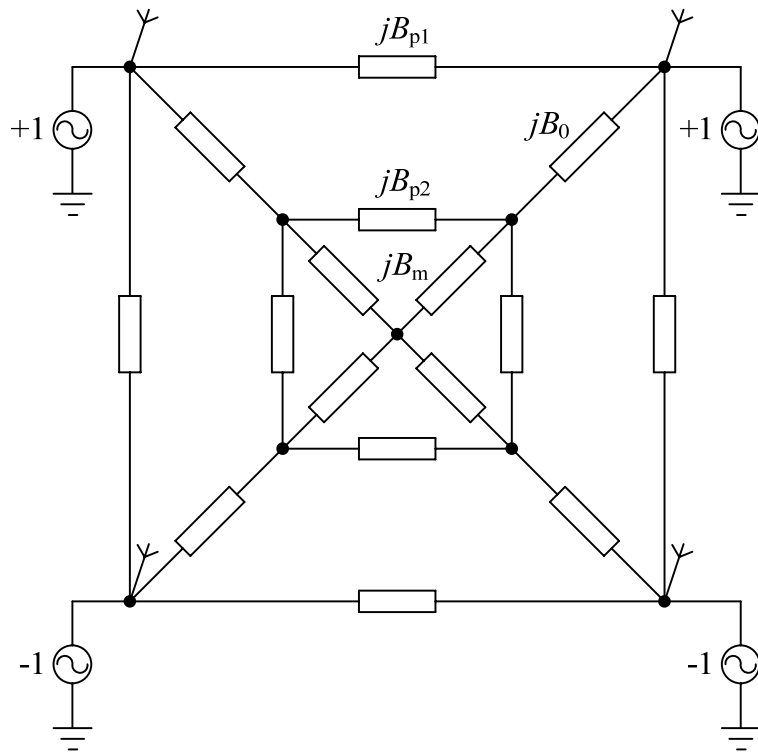


3.23(a)

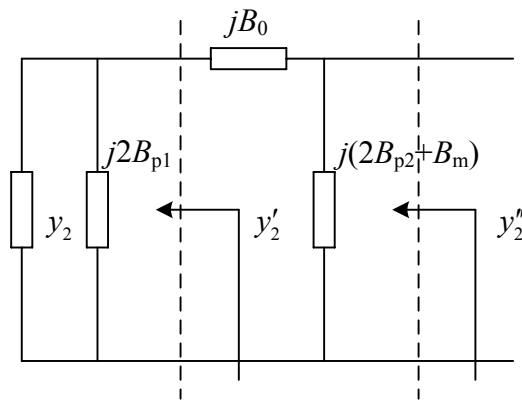


3.23(b)

Figure 3.23 Equivalent circuit for mode 1 with DN.

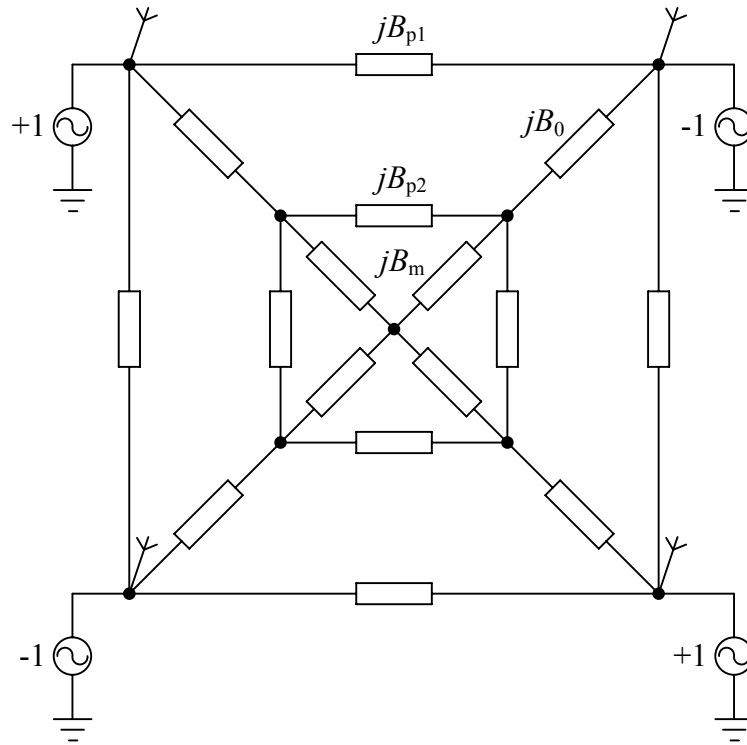


3.24(a)

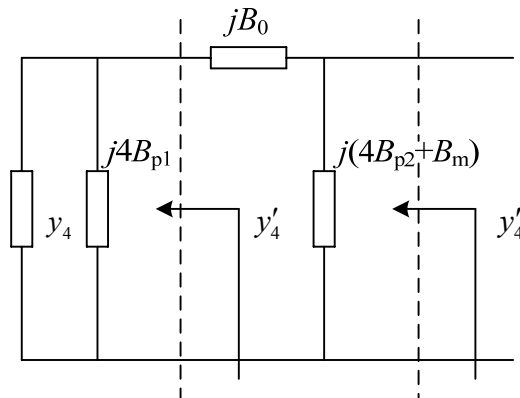


3.24(b)

Figure 3.24 Equivalent circuit for mode 2 and 3 with DN.



3.25(a)



3.25(b)

Figure 3.25 Equivalent circuit for mode 4 with DN.

To have no power reflection for all the four modes, all the four modal admittances y_1'' , y_2'' , y_3'' and y_4'' should be matched to the loads. From the figures above, we have

[29]

$$\begin{aligned}
y'_1 &= y_1 = Y_{11} + 2Y_{12} + Y_{13} \\
y'_2 = y'_3 &= y_2 + j2B_{p1} = Y_{11} - Y_{13} + j2B_{p1} \quad . \\
y'_4 &= y_4 + j4B_{p1} = Y_{11} - 2Y_{12} + Y_{13} + j4B_{p1}
\end{aligned} \tag{3.66}$$

As the parallel elements $j(2B_{p2}+B_m)$ and $j(4B_{p2}+B_m)$ can only change the imaginary part of y''_1 , y''_2 , y''_3 and y''_4 , the real part should be equal to each other to make simultaneous matching of the four modes possible. Therefore, y'_1 , y'_2 , y'_3 and y'_4 should be on one circle, according to the lemma proved earlier.

Let the center of the circle be at (m, n) . From Equation (3.65), we get [29]

$$\begin{aligned}
m &= B_0^2 / 2C \\
n &= -B_0
\end{aligned} \tag{3.67}$$

Rewrite the admittance parameters of the array as

$$\begin{aligned}
Y_{11} &= g_{11} + jb_{11} \\
Y_{12} = Y_{14} &= g_{12} + jb_{12} \quad . \\
Y_{13} &= g_{13} + jb_{13}
\end{aligned} \tag{3.68}$$

Equation (3.66) then becomes

$$\begin{aligned}
y'_1 &= g_1 + jb_1 \\
y'_2 = y'_3 &= g_2 + j(b_2 + B_p), \\
y'_4 &= g_4 + j(b_4 + 2B_p)
\end{aligned} \tag{3.69}$$

where

$$\begin{aligned}
g_1 &= g_{11} + 2g_{12} + g_{13} \\
g_2 &= g_3 = g_{11} - g_{13} \\
g_4 &= g_{11} - 2g_{12} + g_{13} \\
b_1 &= b_{11} + 2b_{12} + b_{13} \quad . \\
b_2 &= b_3 = b_{11} - b_{13} \\
b_4 &= b_{11} - 2b_{12} + b_{13} \\
B_p &= 2B_{p1}
\end{aligned} \tag{3.70}$$

From the lemma we have [29]

$$\begin{aligned}
(g_1 - m)^2 + (b_1 - n)^2 &= m^2 \\
(g_2 - m)^2 + (b_2 + B_p - n)^2 &= m^2 \quad , \\
(g_4 - m)^2 + (b_4 + 2B_p - n)^2 &= m^2
\end{aligned} \tag{3.71}$$

which leads to

$$\begin{aligned}
g_1^2 - 2mg_1 + b_1^2 + n^2 - 2nb_1 &= 0 \\
g_2^2 - 2mg_2 + b_2^2 + B_p^2 + n^2 + 2b_2B_p - 2b_2n - 2B_pn &= 0 \quad . \\
g_4^2 - 2mg_4 + b_4^2 + 4B_p^2 + n^2 + 4b_4B_p - 2b_4n - 4B_pn &= 0
\end{aligned} \tag{3.72}$$

From the first equation of (3.72), we have

$$m = \frac{g_1^2 + b_1^2 + n^2 - 2nb_1}{2g_1} . \tag{3.73}$$

Substituting (3.73) into the last two equations of (3.72), we have

$$\begin{aligned}
ax_1^2 - 2x_1x_2 + x_2^2 + bx_1 + 2b_2x_2 + c &= 0 \\
dx_1^2 - 4x_1x_2 + 4x_2^2 + ex_1 + 4b_3x_2 + f &= 0 \quad ,
\end{aligned} \tag{3.74}$$

where x_1 and x_2 are unknowns defined as

$$\begin{aligned}
x_1 &= n \\
x_2 &= B_p = 2B_{p1} \quad ,
\end{aligned} \tag{3.75}$$

while coefficients are defined as

$$\begin{aligned}
a &= \frac{g_1 - g_2}{g_1} \\
b &= \frac{2g_2b_1 - 2g_1b_2}{g_1} \\
c &= g_2^2 - g_1g_2 - \frac{g_2b_1^2}{g_1} + b_2^2 \\
d &= \frac{g_1 - g_4}{g_1} \\
e &= \frac{2g_4b_1 - 2g_1b_4}{g_1} \\
f &= g_4^2 - g_1g_4 - \frac{g_4b_1^2}{g_1} + b_4^2
\end{aligned} \tag{3.76}$$

Given the conclusions of the lemma, and solving the Equation (3.74), we have [29]

$$\begin{aligned}
B_{p1} &= \frac{x_2}{2} \\
B_0 &= -n = -x_1 \\
C &= \frac{n^2}{2m} = \frac{x_1^2 g_1}{g_1^2 + b_1^2 + x_1^2 - 2x_1b_1}
\end{aligned} \tag{3.77}$$

From Equation (3.64), we have

$$\begin{aligned}
b_1'' &= \frac{g_1'^2 B_0 + b_1'^2 B_0 + b_1' B_0^2}{g_1'^2 + (b_1' + B_0)^2} \\
b_2'' = b_3'' &= \frac{g_2'^2 B_0 + b_2'^2 B_0 + b_2' B_0^2}{g_2'^2 + (b_2' + B_0)^2} + 2B_{p2} + B_m, \\
b_4'' &= \frac{g_4'^2 B_0 + b_4'^2 B_0 + b_4' B_0^2}{g_4'^2 + (b_4' + B_0)^2} + 4B_{p2} + B_m
\end{aligned} \tag{3.78}$$

where b_1'' , b_2'' , b_3'' and b_4'' are defined as

$$\begin{aligned}
y_1'' &= g_1'' + jb_1'' \\
y_2'' = y_3'' &= g_2'' + jb_2'' \\
y_4'' &= g_4'' + jb_4''
\end{aligned} \tag{3.79}$$

It is noted that y_1'' , y_2'' , y_3'' and y_4'' have the same real parts and it is only needed to equate their imaginary parts for matching, that is,

$$b_1'' = b_2'' = b_4'' . \quad (3.80)$$

Solving Equation (3.80) to get [29]

$$B_{p2} = \frac{1}{2} \left[\frac{g_2'^2 B_0 + b_2'^2 B_0 + b_2' B_0^2}{g_2'^2 + (b_2' + B_0)^2} - \frac{g_4'^2 B_0 + b_4'^2 B_0 + b_4' B_0^2}{g_4'^2 + (b_4' + B_0)^2} \right] \quad (3.81)$$

$$B_m = \frac{g_1'^2 B_0 + b_1'^2 B_0 + b_1' B_0^2}{g_1'^2 + (b_1' + B_0)^2} + \frac{g_4'^2 B_0 + b_4'^2 B_0 + b_4' B_0^2}{g_4'^2 + (b_4' + B_0)^2} - 2 \frac{g_2'^2 B_0 + b_2'^2 B_0 + b_2' B_0^2}{g_2'^2 + (b_2' + B_0)^2}$$

Here all the values of the elements in the DN have been calculated [29] and multiple solutions exist for an array.

For the array designed and optimized previously, at the centre frequency of 2.45 GHz, the admittance parameters are given [29] as

$$Y_{11} = 1 \times 10^{-2} + j2.598 \times 10^{-3} \Omega^{-1}$$

$$Y_{12} = 9.397 \times 10^{-5} + j1.161 \times 10^{-2} \Omega^{-1} .$$

$$Y_{13} = -5.183 \times 10^{-3} + j1.009 \times 10^{-3} \Omega^{-1}$$

After solving the equations above, one set of the component values of the DN at center frequency are [29]

$$B_{p1} = 8.036 \times 10^{-3}$$

$$B_{p2} = -1.743 \times 10^{-2}$$

$$B_0 = -1.960 \times 10^{-2}$$

$$B_m = -4.271 \times 10^{-3}$$

The decoupled array can be matched using the L section matching network introduced in section 3.6.1.3. Figure 3.26 shows the calculated port scattering parameters of the decoupled and matched array [29]. It can be seen that S_{12} and S_{13} are reduced to -50 dB from a level of -10 dB in the original array. The DN can be realized by a set of lumped reactive elements, i.e., capacitors or inductors.

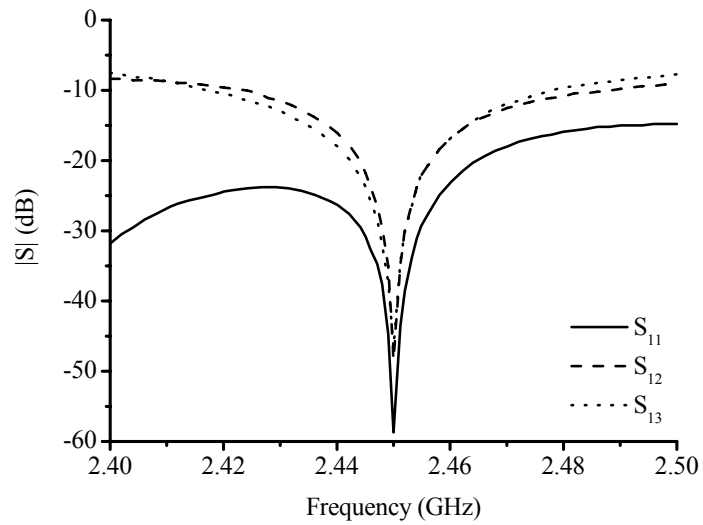


Figure 3.26 S-parameters of the array with decoupling and matching network

3.6.2.1 Measurement results

Photographs of the front and back of the fabricated antenna in [29] are shown in Figures 3.27 and 3.28. The dimension for the ground plane is 10 cm \times 10 cm. The three layers of the structure were etched on two substrates, and these were joined with plastic screws, as shown in the photos. The S-parameters are shown in Figure 3.29. It can be seen that the values of S_{12} and S_{13} are successfully reduced to below -15 dB over the frequency range considered. The array is also matched with a reflection coefficient of about -25 dB at the center frequency.



Figure 3.27 Photo of the front of the array [29]

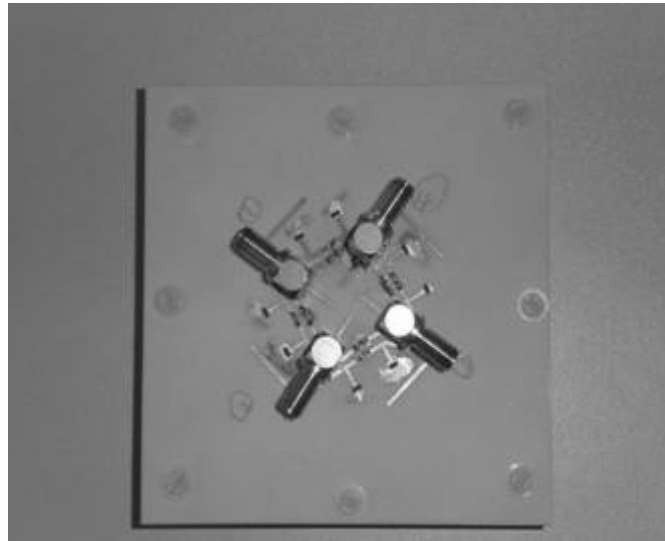


Figure 3.28 Photo of the back of the array [29]

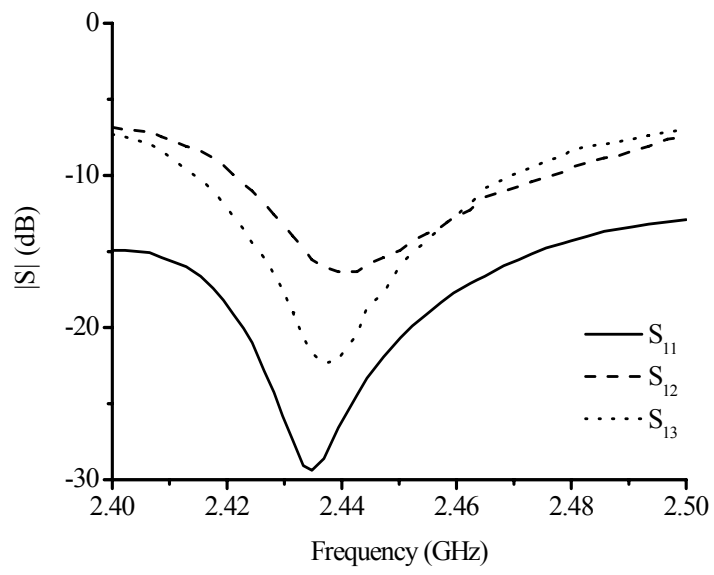


Figure 3.29 Measured S-parameters of the decoupled and matched array

Chapter 4 Closed-form Design Equations for Decoupling Network of Circulant Symmetric Dense Array

4.1 Introduction

Decoupling networks for arrays with arbitrary complex mutual admittances using eigenmode analysis were described in Chapter 3. In this chapter, closed-form design equations for the decoupling network elements of circulant symmetric dense arrays are presented. Design equations for small arrays are described first and are then extended to larger arrays.

4.2 Design of decoupling networks for small arrays

A symmetrical array of $n = 3$ identical elements is characterized by a scattering matrix \mathbf{S}^a given by

$$\mathbf{S}^a = \begin{bmatrix} \begin{bmatrix} S_{11}^a & S_{12}^a \\ S_{12}^a & S_{11}^a \end{bmatrix} & S_{12}^a \\ S_{12}^a & \begin{bmatrix} S_{12}^a & S_{11}^a \end{bmatrix} \end{bmatrix}. \quad (4.1)$$

For an array with $n = 2$ elements, the scattering matrix will be the 2×2 sub-matrix indicated in Equation (4.1). The corresponding impedance matrix can in both cases be calculated from [48]

$$\mathbf{Z}^a = Z_0(\mathbf{I} + \mathbf{S}^a)(\mathbf{I} - \mathbf{S}^a)^{-1}, \quad (4.2)$$

where \mathbf{I} is an $n \times n$ identity matrix and Z_0 is the characteristic impedance of the system.

If $n = 2$, the eigenvalues of the impedance matrix are given by

$$\begin{aligned} Z_a &= R_a + jX_a = Z_{11}^a + Z_{12}^a \\ Z_b &= R_b + jX_b = Z_{11}^a - Z_{12}^a \end{aligned}, \quad (4.3)$$

while the corresponding orthogonal eigenvectors are

$$\begin{aligned}\mathbf{e}_a &= [1, 1]^T \\ \mathbf{e}_b &= [1, -1]^T\end{aligned}\quad (4.4)$$

For $n = 3$, the eigenvalues are

$$\begin{aligned}Z_a &= R_a + jX_a = Z_{11}^a + 2Z_{12}^a \\ Z_b &= R_b + jX_b = Z_{11}^a - Z_{12}^a = Z_c\end{aligned},\quad (4.5)$$

with eigenvectors

$$\begin{aligned}\mathbf{e}_a &= [1, 1, 1]^T \\ \mathbf{e}_b &= [2, -1, -1]^T \\ \mathbf{e}_c &= [0, 1, -1]^T\end{aligned}\quad (4.6)$$

These arrays can be decoupled using the circuits shown in Figure 4.1(a) and (b) respectively. Using the characteristic circuits for the eigenmodes [10, 23, 28], the modal admittances as seen from the new input ports ($1'$, $2'$, etc.) are given by

$$\begin{aligned}Y'_a &= (Z_a + jX_1)^{-1} \\ Y'_b &= (Z_b + jX_1)^{-1} + jnB_2\end{aligned}\quad (4.7)$$

For $n = 3$, note that $Y'_b = Y'_c$.

The array can be decoupled by ensuring that the modal admittances are equal. Setting $Y'_a = Y'_b$ and evaluating the real and imaginary parts give the following closed-form results for the elements of the decoupling network:

$$X_1 = \frac{-B \pm \sqrt{B^2 - 4AC}}{2A}$$

$$B_2 = \frac{1}{n} \left(\frac{X_b + X_1}{R_b^2 + (X_b + X_1)^2} - \frac{X_a + X_1}{R_a^2 + (X_a + X_1)^2} \right), \quad (4.8)$$

where

$$A = R_a - R_b$$

$$B = 2(R_a X_b - R_b X_a)$$

$$C = R_a(R_b^2 + X_b^2) - R_b(R_a^2 + X_a^2)$$
(4.9)

The input impedance at each port will then be equal to the modal impedances defined in Equation (4.7). The ports can be matched to the system impedance Z_0 using L section impedance matching networks [48] described in section 3.6.1.3.

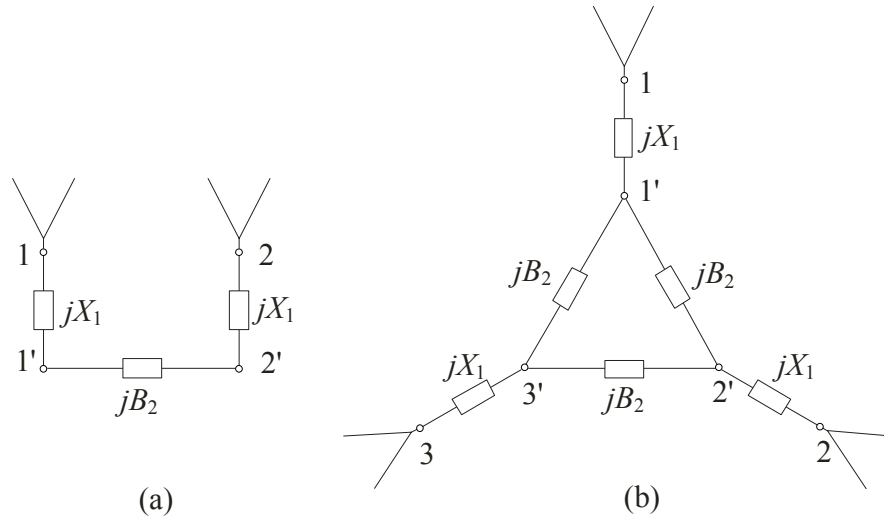


Figure 4.1 Decoupling networks for (a) a 2-element array and (b) a symmetrical 3-element array

To verify the theory, decoupling networks for 2-element and 3-element monopole arrays were designed. The dimensions of the two arrays are given in Table 4.1.

Table 4.1 Dimensions of the 2-element and 3-element monopole arrays

Monopole length	$\lambda/4$
Monopole diameter	0.025λ
Array element spacing	0.1λ

The scattering parameters of the arrays were calculated using IE3D [52] and converted into impedance parameters using Equation (4.2) and assuming a system impedance of $Z_0 = 50\Omega$. The impedance parameters at the centre frequency f_0 and decoupling network elements as calculated using Equation (4.8) are given in Table 4.2. The elements of the L section impedance matching networks are also shown, with X being the reactance of a series element and B the susceptance of a parallel element to ground.

Table 4.2 Calculated decoupling and matching network elements for small arrays

	2-element array	3-element array
Array impedance parameters	$Z_{11}^a = 50.70 + j15.34\Omega$ $Z_{12}^a = 47.05 - j7.02\Omega$	$Z_{11}^a = 48.48 + j9.45\Omega$ $Z_{12}^a = 44.96 - j12.61\Omega$
Decoupling network elements	$X_1 = -41.98$ $B_2 = -0.023$	$X_1 = -45.95$ $B_2 = -0.0128$
Decoupled port impedance	$Z'_a = 97.75 - j33.66\Omega$	$Z'_a = 138.4 - j61.71\Omega$
Matching network elements	$B_3 = 0.00681$ $X_4 = 54.47$	$B_3 = 0.00649$ $X_4 = 76.13$

Again using IE3D, the scattering parameters of the arrays were calculated over a frequency range of $0.95f_0$ to $1.05f_0$ and the results are shown in Figure 4.2 and 4.3.

S_{11}^a and S_{12}^a are scattering parameters of the original array, while S_{11} and S_{12} are the scattering parameters of the decoupled and matched array.

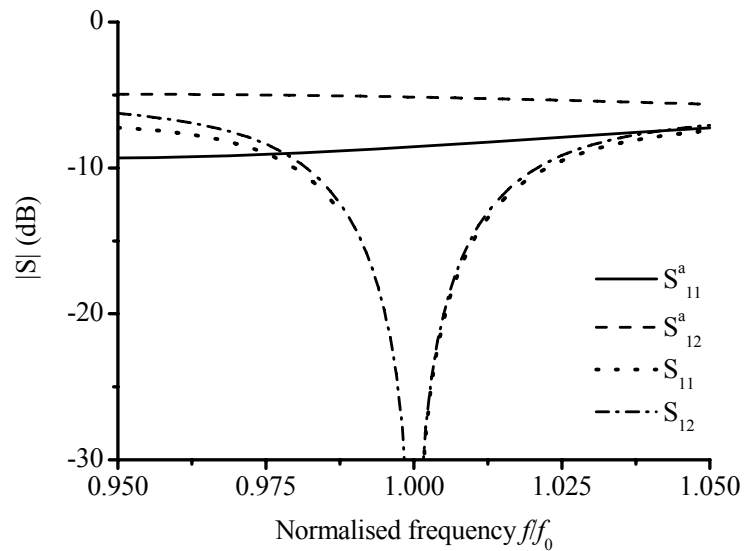


Figure 4.2 Scattering parameters of the 2-element monopole array

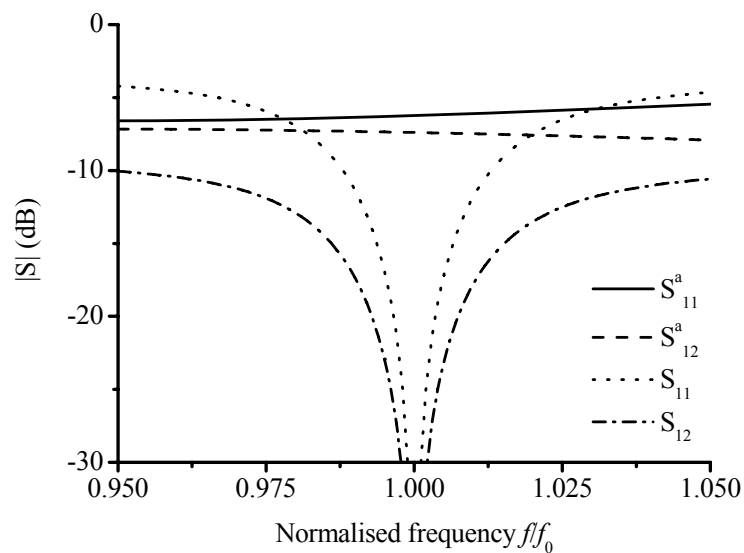


Figure 4.3 Scattering parameters of the 3-element monopole array

The results clearly illustrate the validity of the theory. Simulations for the normalized azimuth radiation pattern of the decoupled 2-element and 3-element arrays when fed at port 1 are shown in Figures 4.4 and 4.5, respectively. When feeding port 2 of the 2-element array, the radiation pattern is rotated by 180° . For excitation at ports 2 or 3 of the 3-element array, the radiation pattern is rotated by $\pm 120^\circ$. The arrays have superdirective radiation patterns suitable for applications in frequency multiplexing, direction finding and adaptive nulling.

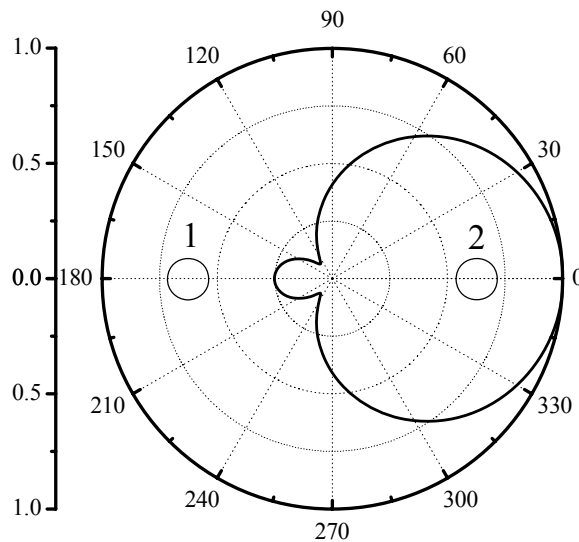


Figure 4.4 Normalized azimuth radiation pattern of the 2-element array

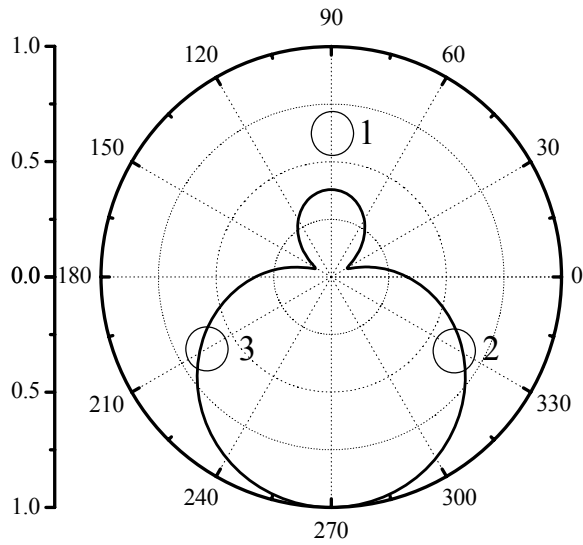


Figure 4.5 Normalized azimuth radiation pattern of the 3-element array

4.3 Design of decoupling networks for larger arrays

To compensate the effect of mutual coupling on system performance degradation, various implementations of passive and lossless decoupling and matching networks have been introduced in literature [23-29, 53-56]. However, all reported investigations have been limited to a maximum of three or four radiators. For maximum versatility, the number of elements in an adaptive array needs to be as large as possible. Extended from Section 4.2, the design of decoupling networks for larger arrays is explored here. For arrays with elements evenly distributed on the circumference of a circle, also called circulant symmetric arrays, a systematic design approach can be formulated. It involves the step-by-step decoupling of the characteristic eigenmodes of the array. The procedure is illustrated by considering the examples of a 6-element and an 8-element circular symmetrical monopole arrays.

4.3.1 Basic circuit model

In order to establish a basic model which can be used to decouple eigenmodes of an array, we first consider the general circuit models shown in Figure 4.6.

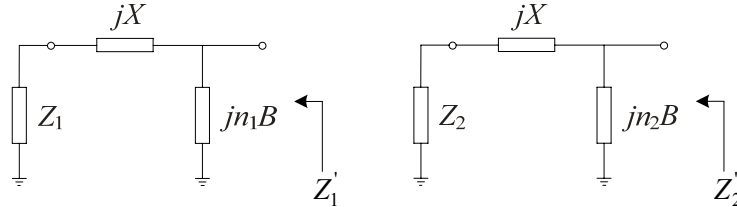


Figure 4.6 General circuit model for matching two distinct terminating impedances

The circuits are terminated in impedances $Z_1 = R_1 + jX_1$ and $Z_2 = R_2 + jX_2$. A series element of impedance of jX and parallel elements with admittances of jn_1B and jn_2B are used to transform Z_1 and Z_2 to produce input admittances of Y_1' and Y_2' . The input admittances are given by

$$\begin{aligned} Y_1' &= (Z_1 + jX)^{-1} + jn_1B \\ Y_2' &= (Z_2 + jX)^{-1} + jn_2B \end{aligned} \quad (4.10)$$

The aim is to match the input admittances. Setting $Y_1' = Y_2'$ and evaluating the real and imaginary parts give

$$X = g(Z_1, Z_2) = \frac{-b \pm \sqrt{b^2 - 4ac}}{2a} \quad (4.11)$$

and

$$\begin{aligned} B &= h(Z_1, n_1, Z_2, n_2, X) \\ &= \frac{1}{(n_1 - n_2)} \left(\frac{X_1 + X}{R_1^2 + (X_1 + X)^2} - \frac{X_2 + X}{R_2^2 + (X_2 + X)^2} \right), \end{aligned} \quad (4.12)$$

where

$$\begin{aligned}
a &= R_1 - R_2 \\
b &= 2(R_1 X_2 - R_2 X_1) \\
c &= R_1(R_2^2 + X_2^2) - R_2(R_1^2 + X_1^2)
\end{aligned} \tag{4.13}$$

This basic circuit can be used to design a decoupling network for a larger array.

4.3.2 Decoupling of large arrays

Decoupling of an array involves a process of modifying its impedance matrix to reduce all the off-diagonal elements to zero. Alternatively, it can also be regarded as a process of equalizing the eigenmode impedances (i.e. the eigenvalues of the impedance matrix). The corresponding eigenvectors can be viewed as the port voltages under the conditions when a specific mode is excited. In general, an N -element array characterized by an impedance matrix with k distinct eigenvalues would require a decoupling network with $2(k-1)$ independent parameters. Decoupling of a symmetrical array can be accomplished in $(k-1)$ stages by using a ladder of circulant symmetric network configurations (henceforth referred to as *stage networks*) which each consist of N identical series reactive elements followed by N identical parallel reactive elements. The parallel elements can be arranged in the shape of polygons (a single N -sided polygon or a set of smaller polygons rotated with respect to one another) or in the shape of a star (with or without a common node at the center). We need to identify $(k-1)$ suitable stage networks. The stage networks will reduce to equivalent circuits resembling those in Figure 4.6 for every eigenmode. We can determine the parameter n of a stage network for each mode by assuming port voltages corresponding to the appropriate eigenvector and using circuit analysis to obtain the equivalent network. Two modes with distinct eigenmode impedances can then be decoupled during each stage. We may use the relations provided in Equations

(4.11) and (4.12) to determine the values of the network elements.

This principle is best illustrated by considering examples of circulant symmetric 6-element and 8-element monopole arrays with elements regularly spaced on the circumference of a circle.

4.3.2.1 Decoupling of a circular symmetrical 6-element array

For such an array, mutual coupling is only a function of the distance between elements, and therefore the scattering parameters of the array are given by

$$\mathbf{S}^a = \begin{bmatrix} S_{11}^a & S_{12}^a & S_{13}^a & S_{14}^a & S_{13}^a & S_{12}^a \\ S_{12}^a & S_{11}^a & S_{12}^a & S_{13}^a & S_{14}^a & S_{13}^a \\ S_{13}^a & S_{12}^a & S_{11}^a & S_{12}^a & S_{13}^a & S_{14}^a \\ S_{14}^a & S_{13}^a & S_{12}^a & S_{11}^a & S_{12}^a & S_{13}^a \\ S_{13}^a & S_{14}^a & S_{13}^a & S_{12}^a & S_{11}^a & S_{12}^a \\ S_{12}^a & S_{13}^a & S_{14}^a & S_{13}^a & S_{12}^a & S_{11}^a \end{bmatrix}. \quad (4.14)$$

The corresponding impedance matrix can be computed from Equation (4.2). The eigenvalues of the impedance matrix (viz. the eigenmode impedances) are given by

$$\begin{aligned} Z_a &= Z_{11}^a + 2Z_{12}^a + 2Z_{13}^a + Z_{14}^a \\ Z_b &= Z_{11}^a - 2Z_{12}^a + 2Z_{13}^a - Z_{14}^a \\ Z_c &= Z_d = Z_{11}^a - Z_{12}^a - Z_{13}^a + Z_{14}^a \\ Z_e &= Z_f = Z_{11}^a + Z_{12}^a - Z_{13}^a - Z_{14}^a \end{aligned}. \quad (4.15)$$

The corresponding eigenvectors are

$$\begin{aligned}
\mathbf{e}_a &= [1, 1, 1, 1, 1, 1]^T \\
\mathbf{e}_b &= [1, -1, 1, -1, 1, -1]^T \\
\mathbf{e}_c &= [1, 0, -1, 1, 0, -1]^T \\
\mathbf{e}_d &= [1, -1, 0, 1, -1, 0]^T \\
\mathbf{e}_e &= [1, 0, -1, -1, 0, 1]^T \\
\mathbf{e}_f &= [1, 1, 0, -1, -1, 0]^T
\end{aligned} \tag{4.16}$$

In order to decouple the array, we use a combination of the circuits shown in Figure 4.7 to decouple sets of eigenmodes. The equivalent circuit for each mode is defined in Figure 4.8.

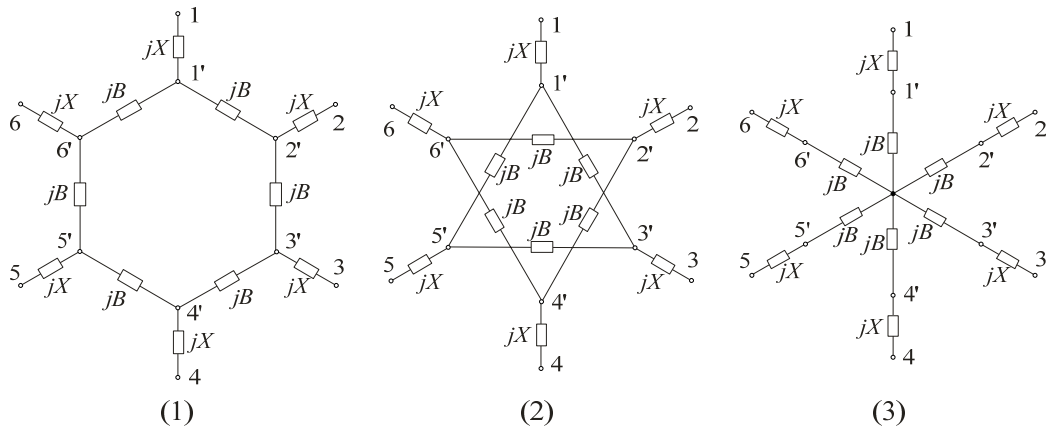


Figure 4.7 Stage network configurations for 6-element array

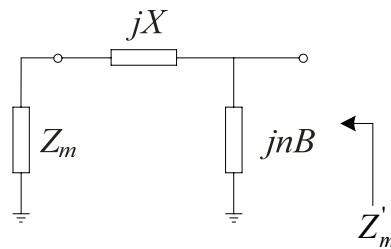
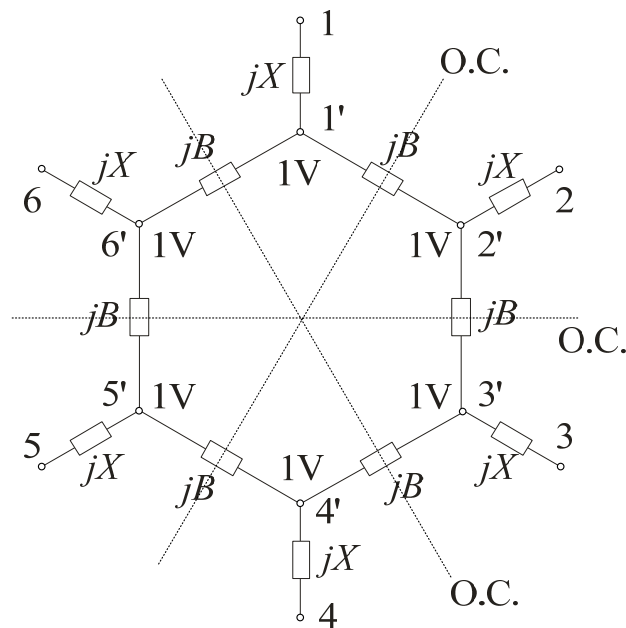
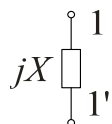


Figure 4.8 Equivalent network of the circuits in Figure 4.7 when mode m is excited

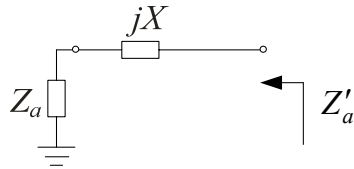
The derivation of the parameter n in the equivalent circuits for each mode is best illustrated by considering the circuits in Figure 4.7 and assuming port voltages corresponding to the respective eigenvectors. Note that “O.C.” stands for open circuit while “S.C.” stands for short circuit to the ground. First, let’s consider the first circuit in Figure 4.7 and mode a . Since the eigenvector is $\mathbf{e}_a = [1, 1, 1, 1, 1, 1]^T$, an excitation vector $\mathbf{V} = [1, 1, 1, 1, 1, 1]$ Volt is applied to ports 1'-6' as shown in Figure 4.9(a). The circuit reduces to the one shown in Figure 4.9(b), resulting in the equivalent circuit of Figure 4.9(c). From inspection, it follows that the parameter $n = 0$ for mode a .



(a) Mode a of the first circuit in Figure 4.7



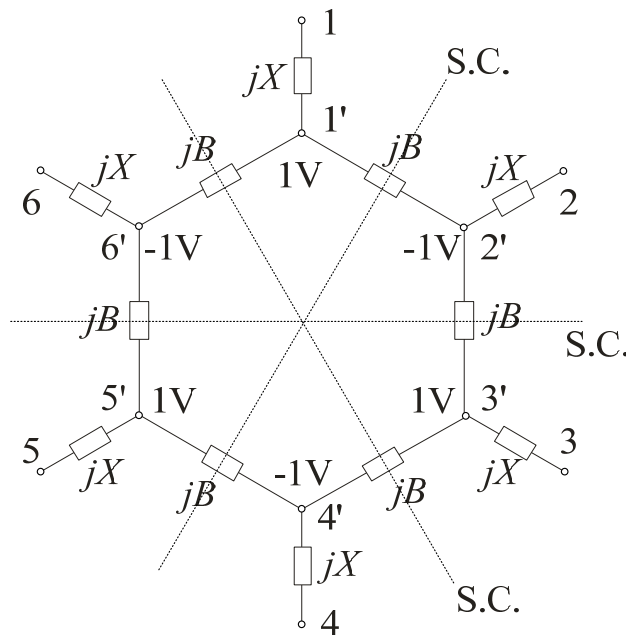
(b) Intermediate equivalent circuit for mode a



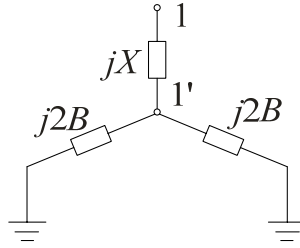
(c) Equivalent circuit for mode a

Figure 4.9 Equivalent circuit of the first circuit in Figure 4.7 for mode a

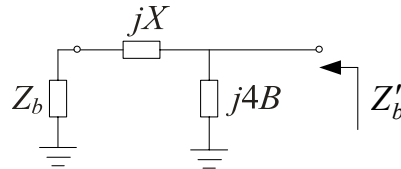
Then we consider mode b of the first circuit in Figure 4.7. Since the eigenvector is $\mathbf{e}_b = [1, -1, 1, -1, 1, -1]^T$, $\mathbf{V} = [1, -1, 1, -1, 1, -1]$ Volt is applied to ports $1'-6'$ as shown in Figure 4.10(a). The circuit reduces to the one shown in Figure 4.10(b), resulting in the equivalent circuit of Figure 4.10(c). From inspection, it follows that the parameter $n = 4$ for mode b .



(a) Mode b of the first circuit in Figure 4.7



(b) Intermediate equivalent circuit for mode b

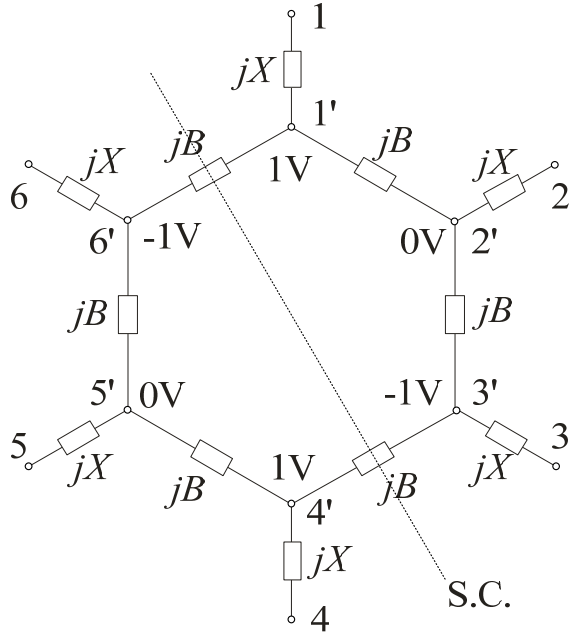


(c) Equivalent circuit for mode b

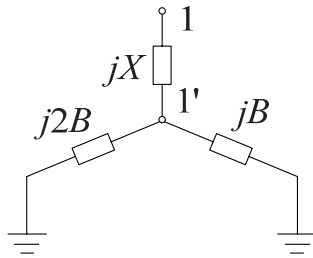
Figure 4.10 Equivalent circuit of the first circuit in Figure 4.7 for mode b

Next, we consider modes c and d of the first circuit in Figure 4.7. Since the eigenvector is $\mathbf{e}_c = [1, 0, -1, 1, 0, -1]^T$, $\mathbf{V} = [1, 0, -1, 1, 0, -1]$ Volt is applied to ports 1'-6' as shown in Figure 4.11(a). Note that when a port has a voltage of 0 V, it can be grounded to earth. The circuit reduces to the one shown in Figure 4.11(b), resulting in the equivalent circuit of Figure 4.11(c). From inspection, it follows that the parameter $n = 3$ for mode c and d .

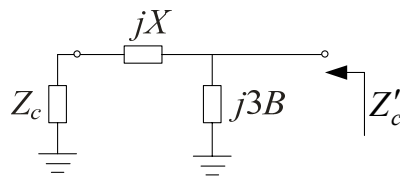
Finally, we consider modes e and f of the first circuit in Figure 4.7. Since the eigenvector is $\mathbf{e}_e = [1, 0, -1, -1, 0, 1]^T$, $\mathbf{V} = [1, 0, -1, -1, 0, 1]$ Volt is applied to ports 1'-6' as shown in Figure 4.12(a). The circuit reduces to the one shown in Figure 4.12(b), resulting in the equivalent circuit of Figure 4.12(c). From inspection, it follows that the parameter $n = 1$ for mode e and f .



(a) Modes *c* and *d* of the first circuit in Figure 4.7

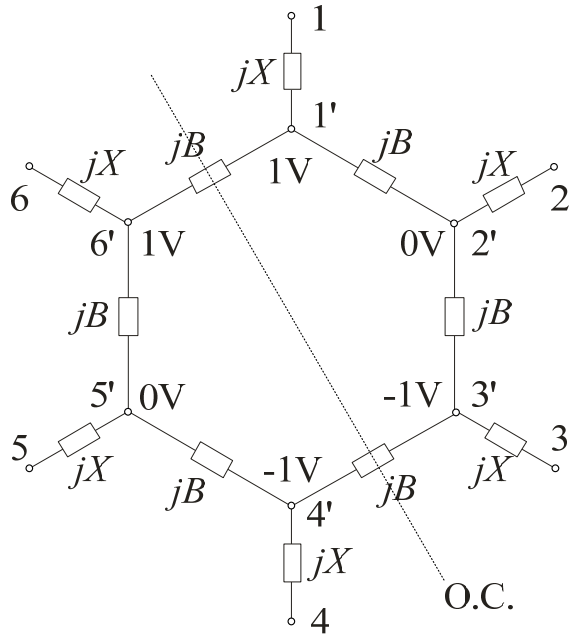


(b) Intermediate equivalent circuit for modes *c* and *d*

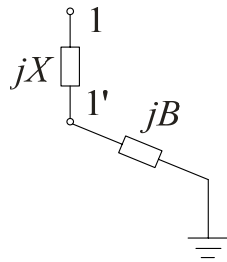


(c) Equivalent circuit for modes *c* and *d*

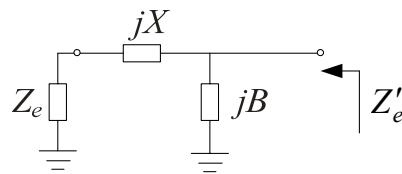
Figure 4.11 Equivalent circuit of the first circuit in Figure 4.7 for modes *c* and *d*



(a) Modes e and f of the first circuit in Figure 4.7



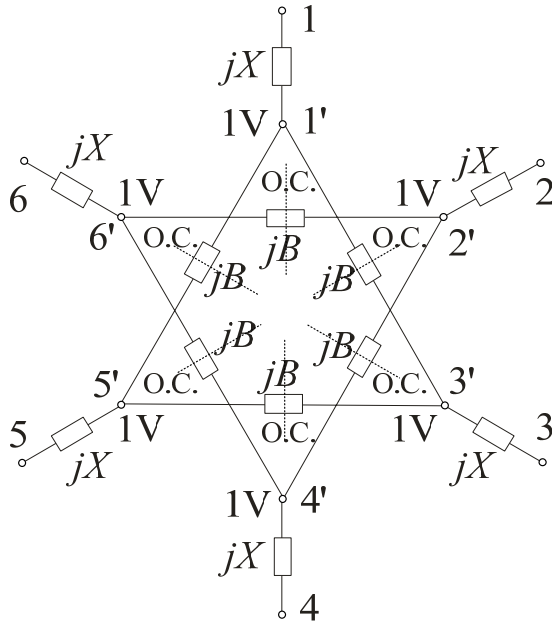
(b) Intermediate equivalent circuit for modes e and f



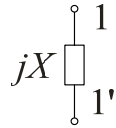
(c) Equivalent circuit for modes e and f

Figure 4.12 Equivalent circuit of the first circuit in Figure 4.7 for modes e and f

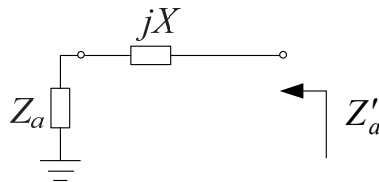
Now the equivalent circuits of the first circuit in Figure 4.7 for all modes have been derived. Similarly, the equivalent circuits of the second and the third circuits in Figure 4.7 for different modes can be obtained and are shown in Figures 4.13-4.16 and Figures 4.17-4.20 respectively. The results are summarized in Table 4.3.



(a) Mode a of the second circuit in Figure 4.7

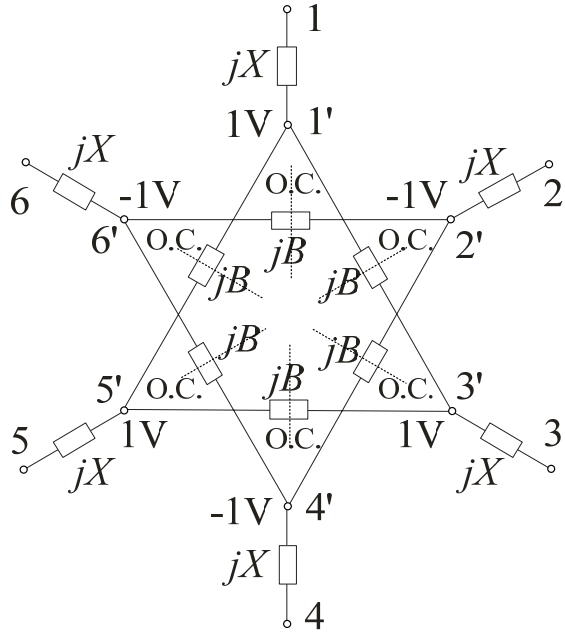


(b) Intermediate equivalent circuit for mode a

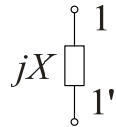


(c) Equivalent circuit for mode a

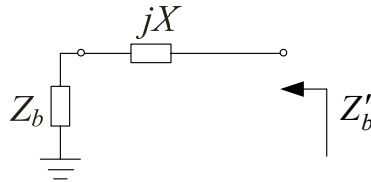
Figure 4.13 Equivalent circuit of the second circuit in Figure 4.7 for mode a



(a) Mode b of the second circuit in Figure 4.7

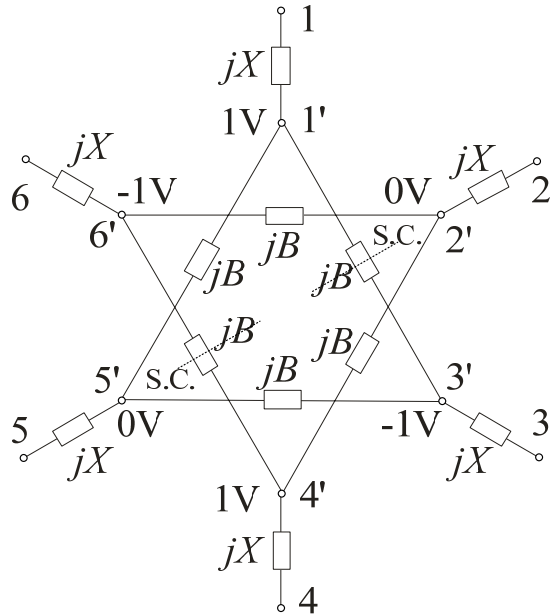


(b) Intermediate equivalent circuit for mode b

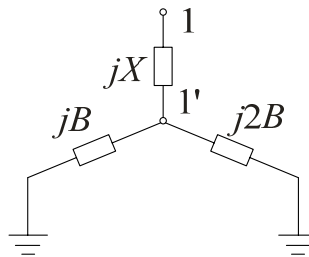


(c) Equivalent circuit for mode b

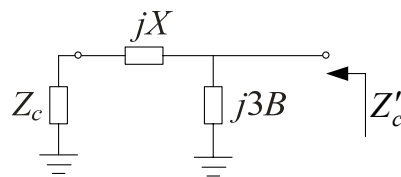
Figure 4.14 Equivalent circuit of the second circuit in Figure 4.7 for mode b



(a) Modes *c* and *d* of the second circuit in Figure 4.7

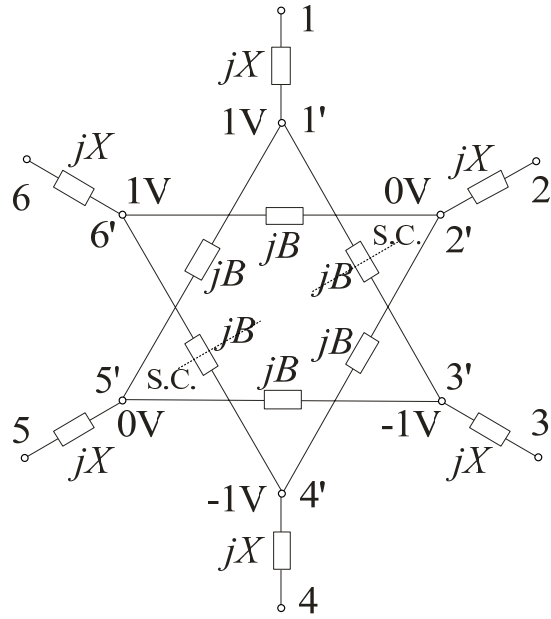


(b) Intermediate equivalent circuit for modes *c* and *d*

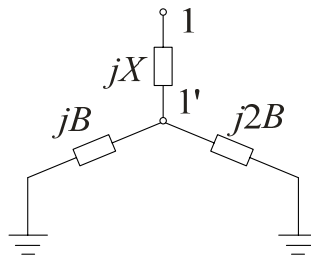


(c) Equivalent circuit for modes *c* and *d*

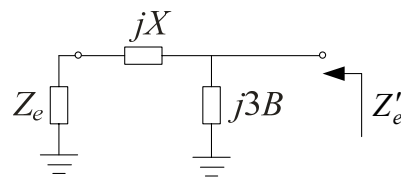
Figure 4.15 Equivalent circuit of the second circuit in Figure 4.7 for modes *c* and *d*



(a) Modes e and f of the second circuit in Figure 4.7

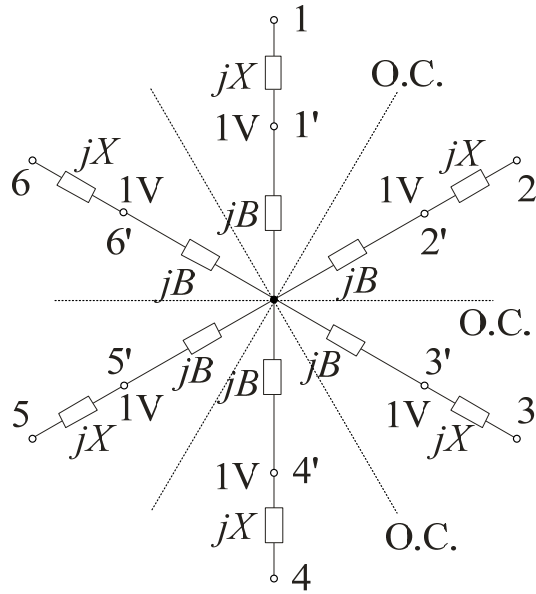


(b) Intermediate equivalent circuit for modes e and f

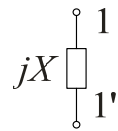


(c) Equivalent circuit for modes e and f

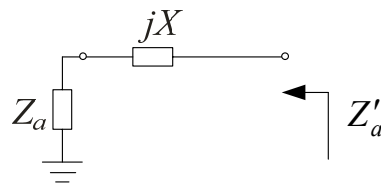
Figure 4.16 Equivalent circuit of the second circuit in Figure 4.7 for modes e and f



(a) Mode a of the third circuit in Figure 4.7

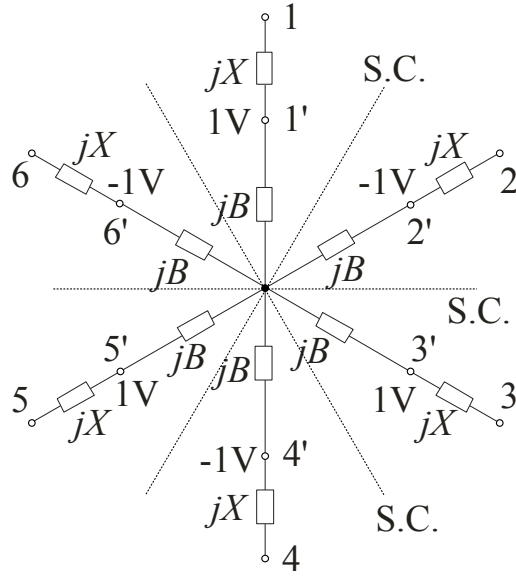


(b) Intermediate equivalent circuit for mode a

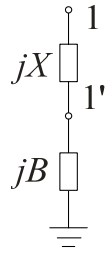


(c) Equivalent circuit for mode a

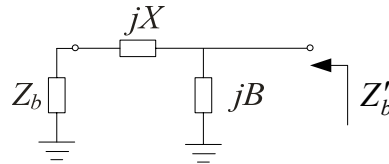
Figure 4.17 Equivalent circuit of the third circuit in Figure 4.7 for mode a



(a) Mode *b* of the third circuit in Figure 4.7

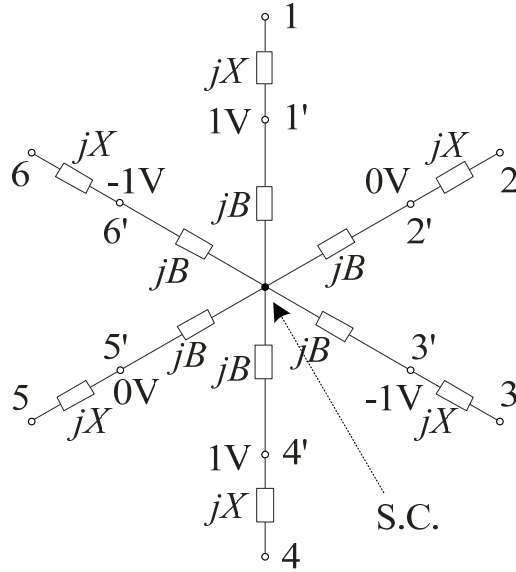


(b) Intermediate equivalent circuit for mode *b*

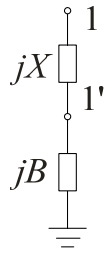


(c) Equivalent circuit for mode *b*

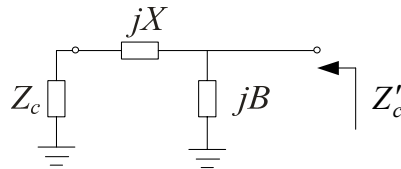
Figure 4.18 Equivalent circuit of the third circuit in Figure 4.7 for mode *b*



(a) Modes c and d of the third circuit in Figure 4.7

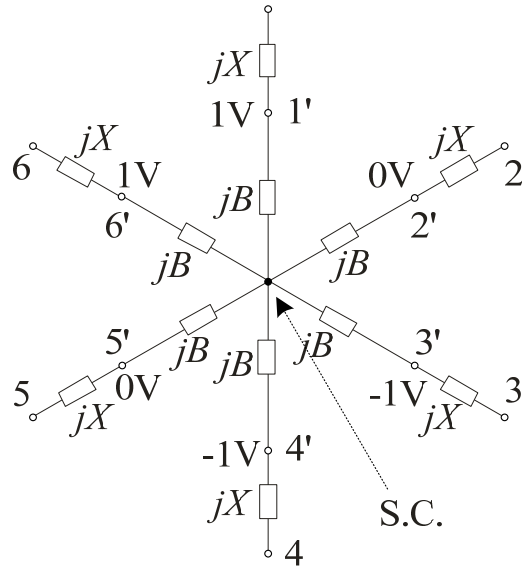


(b) Intermediate equivalent circuit for modes c and d

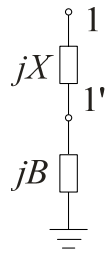


(c) Equivalent circuit for modes c and d

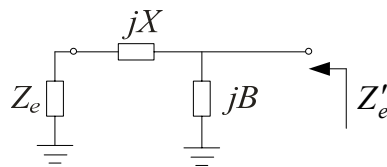
Figure 4.19 Equivalent circuit of the third circuit in Figure 4.7 for modes c and d



(a) Modes e and f of the third circuit in Figure 4.7



(b) Intermediate equivalent circuit for modes e and f

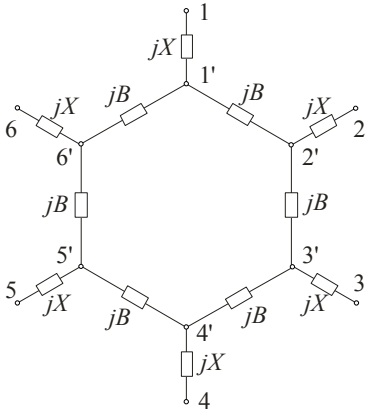
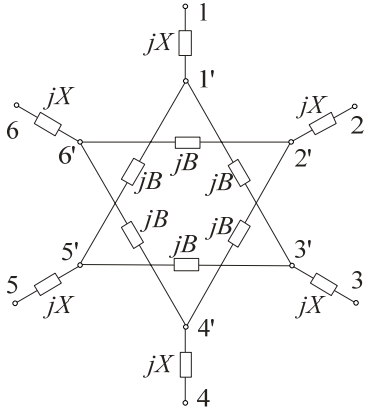
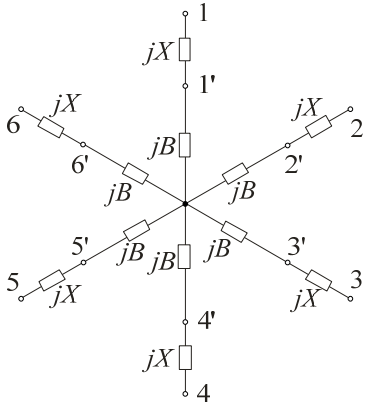


(c) Equivalent circuit for modes e and f

Figure 4.20 Equivalent circuit of the third circuit in Figure 4.7 for modes e and f

From Table 4.3, it is clear that we can use the first circuit to decouple mode groups (c , d) and (e , f), the second circuit to decouple mode groups b and (c , d , e , f) and finally the third circuit for decoupling mode groups a and (b , c , d , e , f). The complete decoupling network is shown in Figure 4.21.

Table 4.3 Basic circuit configurations for mode decoupling

Circuit	Parameter n
	<p>Mode a: $n = 0$</p> <p>Mode b: $n = 4$</p> <p>Modes c, d: $n = 3$</p> <p>Modes e, f: $n = 1$</p>
	<p>Modes a, b: $n = 0$</p> <p>Modes c, d, e, f: $n = 3$</p>
	<p>Mode a: $n = 0$</p> <p>Modes b, c, d, e, f: $n = 1$</p>

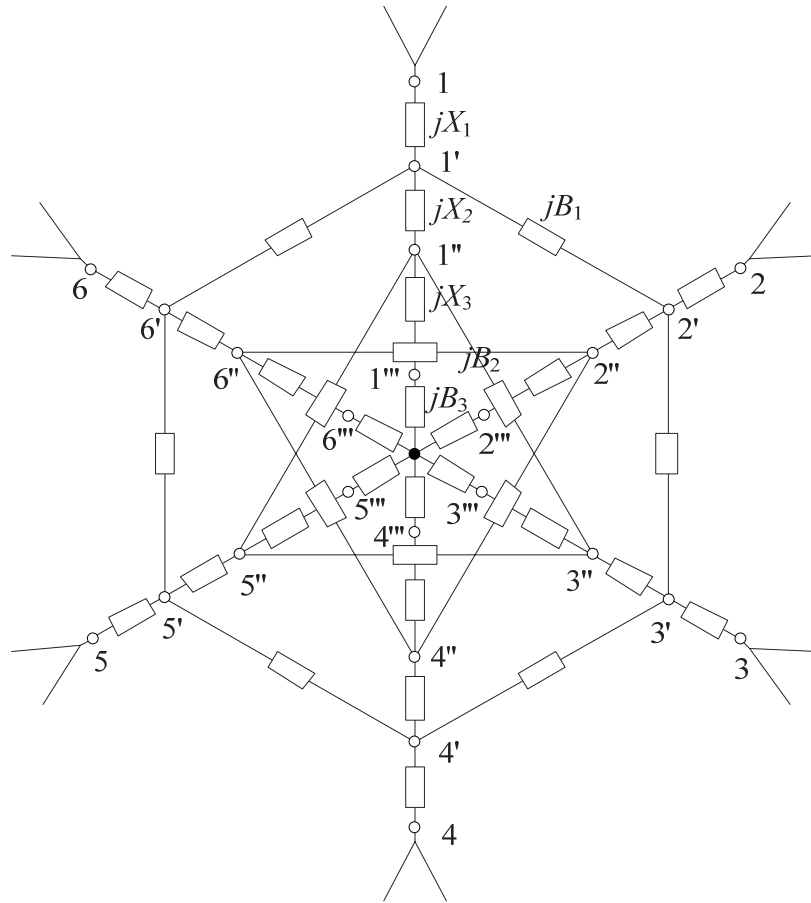


Figure 4.21 Complete decoupling network for a symmetrical 6-element array

Comparing the relevant equivalent circuits for mode groups (c, d) and (e, f) with those shown in Figure 4.6, it follows that $X_1 = g(Z_c, Z_e)$ and $B_1 = h(Z_c, 3, Z_e, 1, X_1)$, with g and h as defined in Equations (4.11) and (4.12). The new impedance parameters as seen from ports 1', 2', 3', 4', 5' and 6' in Figure 4.21 are given by

$$\mathbf{Z}' = ((\mathbf{Z}^a + \mathbf{Z}_1)^{-1} + \mathbf{Y}_1)^{-1}. \quad (4.17)$$

The terms \mathbf{Z}_1 and \mathbf{Y}_1 in (4.17) are defined by

$$\mathbf{Z}_1 = \text{diag}[jX_1, jX_1, jX_1, jX_1, jX_1, jX_1], \quad (4.18)$$

and

$$\mathbf{Y}_1 = \begin{bmatrix} j2B_1 & -jB_1 & 0 & 0 & 0 & -jB_1 \\ -jB_1 & j2B_1 & -jB_1 & 0 & 0 & 0 \\ 0 & -jB_1 & j2B_1 & -jB_1 & 0 & 0 \\ 0 & 0 & -jB_1 & j2B_1 & -jB_1 & 0 \\ 0 & 0 & 0 & -jB_1 & j2B_1 & -jB_1 \\ -jB_1 & 0 & 0 & 0 & -jB_1 & j2B_1 \end{bmatrix}. \quad (4.19)$$

The eigenvalues for \mathbf{Z}' are then obtained as

$$\begin{aligned} Z'_a &= Z'_{11} + 2Z'_{12} + 2Z'_{13} + Z'_{14} \\ Z'_b &= Z'_{11} - 2Z'_{12} + 2Z'_{13} - Z'_{14} \\ Z'_c &= Z'_d = Z'_e = Z'_f = Z'_{11} - Z'_{12} - Z'_{13} + Z'_{14} \end{aligned}. \quad (4.20)$$

Note that modes c , d , e and f are now decoupled.

Subsequently, we decouple mode groups b and (c, d, e, f) using circuit elements X_2 and B_2 . Comparing the equivalent circuits with those shown in Figure 4.6 gives $X_2 = g(Z'_b, Z'_c)$ and $B_2 = h(Z'_b, 0, Z'_c, 3, X_2)$. The impedance parameters as seen from ports 1", 2", 3", 4", 5" and 6" in Figure 4.21 are given by

$$\mathbf{Z}'' = ((\mathbf{Z}' + \mathbf{Z}_2)^{-1} + \mathbf{Y}_2)^{-1}, \quad (4.21)$$

where \mathbf{Z}_2 is defined by Equation (4.18), and

$$\mathbf{Y}_2 = \begin{bmatrix} j2B_2 & 0 & -jB_2 & 0 & -jB_2 & 0 \\ 0 & j2B_2 & 0 & -jB_2 & 0 & -jB_2 \\ -jB_2 & 0 & j2B_2 & 0 & -jB_2 & 0 \\ 0 & -jB_2 & 0 & j2B_2 & 0 & -jB_2 \\ -jB_2 & 0 & -jB_2 & 0 & j2B_2 & 0 \\ 0 & -jB_2 & 0 & -jB_2 & 0 & j2B_2 \end{bmatrix}. \quad (4.22)$$

The eigenvalues of \mathbf{Z}'' are found as

$$\begin{aligned} Z''_a &= Z''_{11} + 2Z''_{12} + 2Z''_{13} + Z''_{14} \\ Z''_b &= Z''_c = Z''_d = Z''_e = Z''_f = Z''_{11} - 2Z''_{12} + 2Z''_{13} - Z''_{14} \end{aligned}. \quad (4.23)$$

Finally, mode groups a and (b, c, d, e, f) are decoupled. From the equivalent circuits for these modes, it follows that $X_3 = g(Z_a'', Z_b'')$ and $B_3 = h(Z_a'', 0, Z_b'', 1, X_3)$. The impedance parameters as seen from ports 1''', 2''', 3''', 4''', 5''' and 6''' are then given by

$$\mathbf{Z}''' = ((\mathbf{Z}'' + \mathbf{Z}_3) + \mathbf{Y}_3)^{-1}, \quad (4.24)$$

where \mathbf{Z}_3 is defined by Equation (4.18) and

$$\mathbf{Y}_3 = \begin{bmatrix} j\frac{5}{6}B_3 & -\frac{j}{6}B_3 & -\frac{j}{6}B_3 & -\frac{j}{6}B_3 & -\frac{j}{6}B_3 & -\frac{j}{6}B_3 \\ -\frac{j}{6}B_3 & j\frac{5}{6}B_3 & -\frac{j}{6}B_3 & -\frac{j}{6}B_3 & -\frac{j}{6}B_3 & -\frac{j}{6}B_3 \\ -\frac{j}{6}B_3 & -\frac{j}{6}B_3 & j\frac{5}{6}B_3 & -\frac{j}{6}B_3 & -\frac{j}{6}B_3 & -\frac{j}{6}B_3 \\ -\frac{j}{6}B_3 & -\frac{j}{6}B_3 & -\frac{j}{6}B_3 & j\frac{5}{6}B_3 & -\frac{j}{6}B_3 & -\frac{j}{6}B_3 \\ -\frac{j}{6}B_3 & -\frac{j}{6}B_3 & -\frac{j}{6}B_3 & -\frac{j}{6}B_3 & j\frac{5}{6}B_3 & -\frac{j}{6}B_3 \\ -\frac{j}{6}B_3 & -\frac{j}{6}B_3 & -\frac{j}{6}B_3 & -\frac{j}{6}B_3 & -\frac{j}{6}B_3 & j\frac{5}{6}B_3 \end{bmatrix}. \quad (4.25)$$

All modes are then matched, since

$$Z_a''' = Z_b''' = Z_c''' = Z_d''' = Z_e''' = Z_f''' = Z_{11}'''. \quad (4.26)$$

The new input ports will also be decoupled and will have the same input impedance. Again, the ports can be matched to the system impedance Z_0 using L section impedance matching networks [48] described in Section 3.6.1.3.

To verify the theory, a decoupling network for a specific 6-element monopole array was designed and analyzed. The six elements of the array were evenly distributed on a circle with radius of 15 mm (0.125λ at a center frequency of $f_0 = 2.5$ GHz). Each monopole had a length of 28 mm (0.23λ) and a diameter of 1 mm (0.0083λ). With a system impedance of $Z_0 = 50 \Omega$, the array's S-parameters were computed using IE3D [52] and converted into impedance parameters using Equation (4.2). The scattering

parameters of the array at f_0 and the computed decoupling network elements are specified in Table 4.4. The elements of the L section impedance matching networks are also shown, with B_4 being the susceptance of a parallel element to ground and X_4 the reactance of a series element.

Table 4.4 S-parameters and decoupling network elements for the 6-element array

Array scattering parameter	$S_{11}^a = -6.79 \text{ dB } \angle 159.3^\circ$ $S_{12}^a = -7.96 \text{ dB } \angle 4.5^\circ$ $S_{13}^a = -15.33 \text{ dB } \angle -53.4^\circ$ $S_{14}^a = -17.93 \text{ dB } \angle -101.5^\circ$
Decoupling network elements	$X_1 = 4.4123, B_1 = 0.05184$ $X_2 = -2.2399, B_2 = -0.06078$ $X_3 = 2.7955, B_3 = 0.1087$
Decoupled port impedance	$Z_a''' = 142.661 - j69.2205\Omega$
Matching network elements	$B_4 = 0.006263, X_4 = 79.4505$

The scattering parameters of the decoupled and matched array were calculated over a frequency range of $0.98f_0$ to $1.02f_0$ and shown in Figures 4.22. The results shown clearly illustrate the validity of the theory. Simulations for the normalized azimuth radiation pattern of the decoupled 6-element array obtained by feeding the port 1 are shown in Figure 4.23. For excitation at successive ports, the radiation pattern will be rotated by 60° . The array is suitable for applications in frequency multiplexing, direction finding and adaptive nulling.

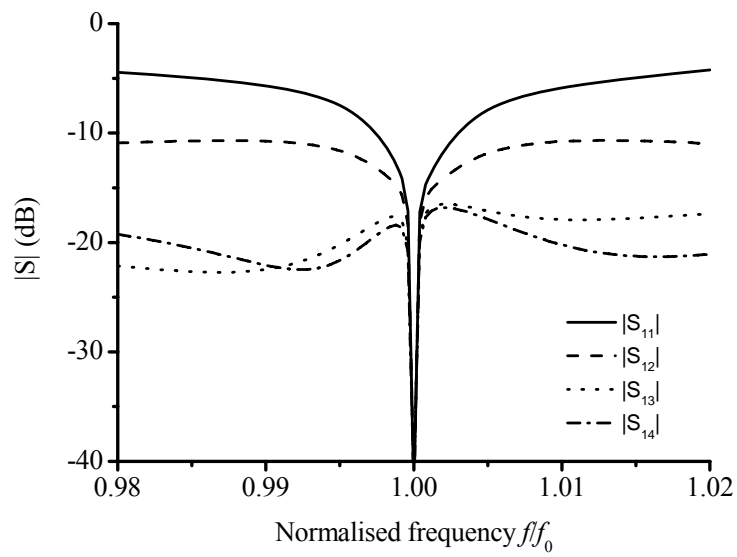


Figure 4.22 Scattering parameters of the decoupled and matched 6-element array

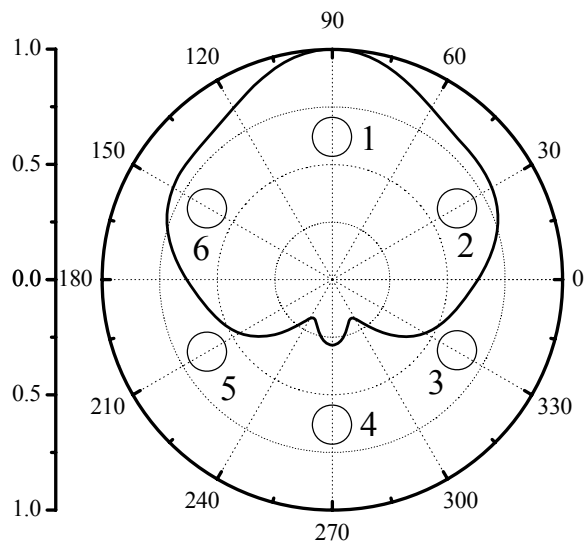


Figure 4.23 Normalized azimuth radiation pattern of the decoupled 6-element array

4.3.2.2 Decoupling of a circular symmetrical 8-element array

The scattering parameters of the circular symmetrical 8-element array are given by

$$\mathbf{S}^a = \begin{bmatrix} S_{11}^a & S_{12}^a & S_{13}^a & S_{14}^a & S_{15}^a & S_{14}^a & S_{13}^a & S_{12}^a \\ S_{12}^a & S_{11}^a & S_{12}^a & S_{13}^a & S_{14}^a & S_{15}^a & S_{14}^a & S_{13}^a \\ S_{13}^a & S_{12}^a & S_{11}^a & S_{12}^a & S_{13}^a & S_{14}^a & S_{15}^a & S_{14}^a \\ S_{14}^a & S_{13}^a & S_{12}^a & S_{11}^a & S_{12}^a & S_{13}^a & S_{14}^a & S_{15}^a \\ S_{15}^a & S_{14}^a & S_{13}^a & S_{12}^a & S_{11}^a & S_{12}^a & S_{13}^a & S_{14}^a \\ S_{14}^a & S_{15}^a & S_{14}^a & S_{13}^a & S_{12}^a & S_{11}^a & S_{12}^a & S_{13}^a \\ S_{13}^a & S_{14}^a & S_{15}^a & S_{14}^a & S_{13}^a & S_{12}^a & S_{11}^a & S_{12}^a \\ S_{12}^a & S_{13}^a & S_{14}^a & S_{15}^a & S_{14}^a & S_{13}^a & S_{12}^a & S_{11}^a \end{bmatrix}. \quad (4.27)$$

Again, the corresponding impedance matrix can be computed from Equation (4.2).

The eigenvalues of the impedance matrix are given by

$$\begin{aligned} Z_a &= Z_{11}^a + 2Z_{12}^a + 2Z_{13}^a + 2Z_{14}^a + Z_{15}^a \\ Z_b &= Z_{11}^a - 2Z_{12}^a + 2Z_{13}^a - 2Z_{14}^a + Z_{15}^a \\ Z_c &= Z_d = Z_{11}^a - 2Z_{13}^a + Z_{15}^a \\ Z_e &= Z_f = Z_{11}^a - \sqrt{2}Z_{12}^a + \sqrt{2}Z_{14}^a - Z_{15}^a \\ Z_g &= Z_h = Z_{11}^a + \sqrt{2}Z_{12}^a - \sqrt{2}Z_{14}^a - Z_{15}^a \end{aligned}, \quad (4.28)$$

and the corresponding eigenvectors are

$$\begin{aligned} \mathbf{e}_a &= [1, 1, 1, 1, 1, 1, 1, 1]^T \\ \mathbf{e}_b &= [1, -1, 1, -1, 1, -1, 1, -1]^T \\ \mathbf{e}_c &= [1, 1, -1, -1, 1, 1, -1, -1]^T \\ \mathbf{e}_d &= [1, -1, -1, 1, 1, -1, -1, 1]^T \\ \mathbf{e}_e &= [\sqrt{2}, -1, 0, 1, -\sqrt{2}, 1, 0, -1]^T \\ \mathbf{e}_f &= [1, -\sqrt{2}, -1, 0, -1, \sqrt{2}, -1, 0]^T \\ \mathbf{e}_g &= [\sqrt{2}, 1, 0, -1, -\sqrt{2}, -1, 0, 1]^T \\ \mathbf{e}_h &= [1, \sqrt{2}, 1, 0, -1, -\sqrt{2}, -1, 0]^T \end{aligned}. \quad (4.29)$$

In order to decouple the eigenmodes, we need to ensure that their modal impedances, i.e. eigenvalues of impedance matrix, are equal. Similar to the previous example of 6-element array, we use a combination of the circuits shown in Figure 4.24 to decouple sets of eigenmodes. The equivalent circuit for each mode is also defined in Figure 4.8.

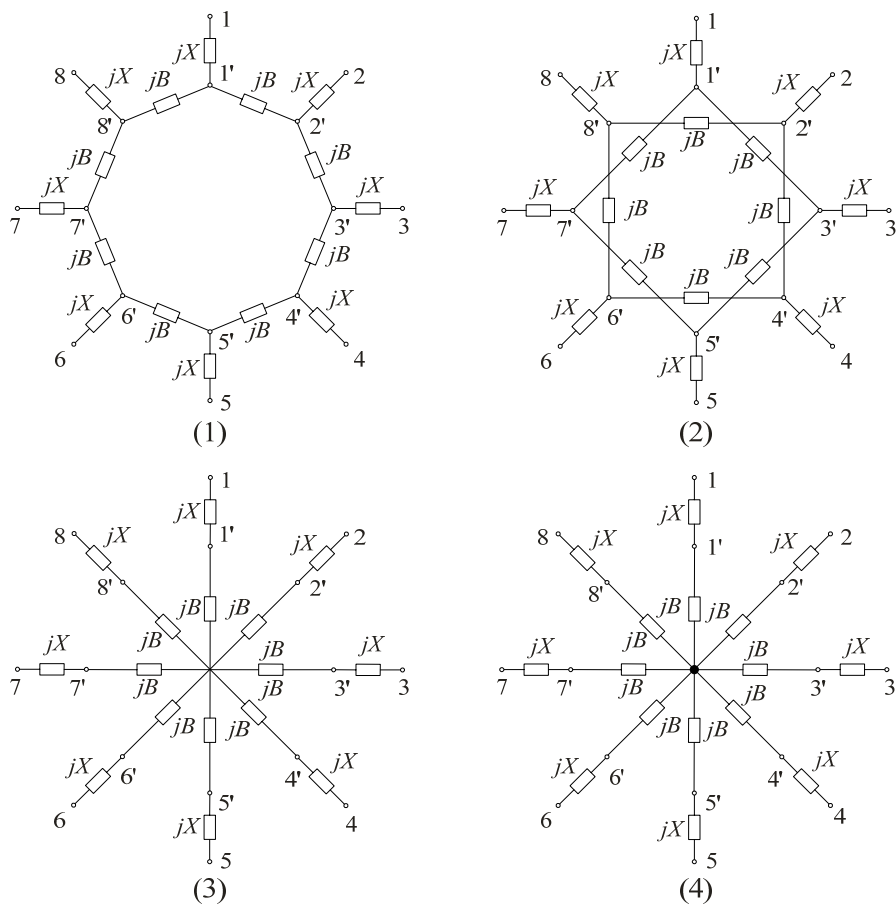
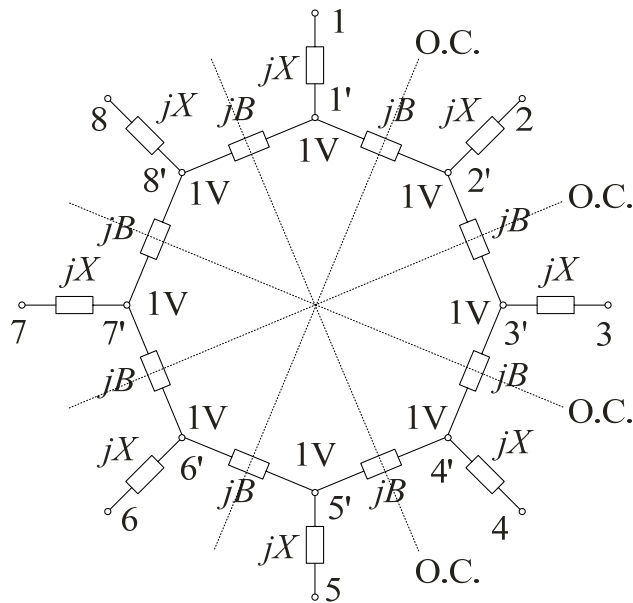


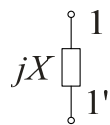
Figure 4.24 Stage network configurations for 8-element array

Before calculating the values of components in each circuit, we show the derivation of the parameter n in the equivalent circuits for each mode. Please note that “O.C.” stands for open circuit while “S.C.” stands for short circuit to the ground.

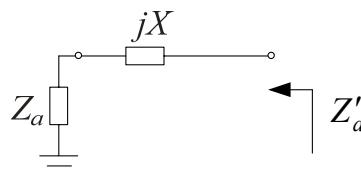
First, let's consider the first circuit in Figure 4.24 and mode a . Since the eigenvector is $\mathbf{e}_a = [1, 1, 1, 1, 1, 1, 1, 1]^T$, an excitation vector $\mathbf{V} = [1, 1, 1, 1, 1, 1, 1, 1]$ Volt is applied to ports 1'-8' as shown in Figure 4.25(a). The circuit reduces to the one shown in Figure 4.25(b), resulting in the equivalent circuit of Figure 4.25(c). From inspection, it follows that the parameter $n = 0$ for mode a .



(a) Mode a of the first circuit in Figure 4.24



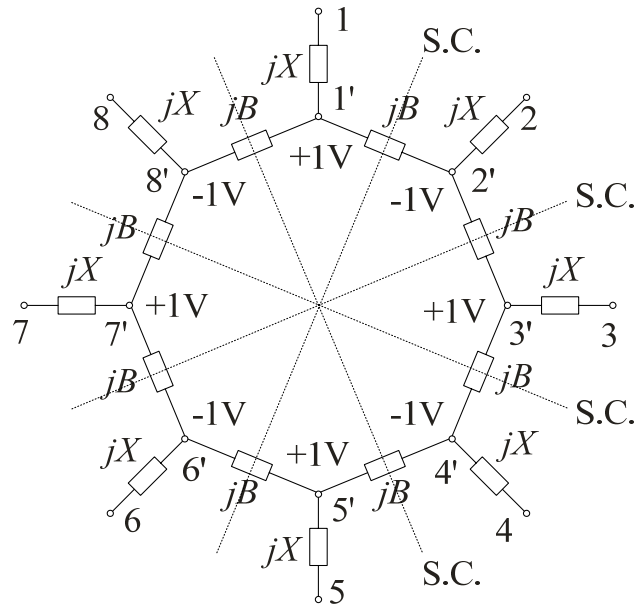
(b) Intermediate equivalent circuit for mode a



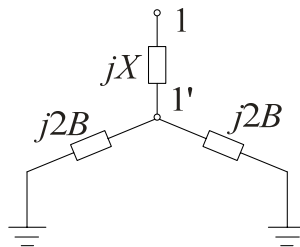
(c) Equivalent circuit for mode a

Figure 4.25 Equivalent circuit of the first circuit in Figure 4.24 for mode a

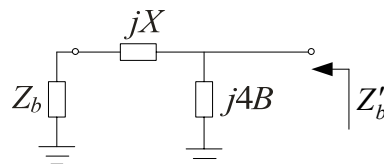
Next, we consider mode b of the first circuit in Figure 4.24. Since the eigenvector is $\mathbf{e}_b = [1, -1, 1, -1, 1, -1, 1, -1]^T$, $\mathbf{V} = [1, -1, 1, -1, 1, -1, +1, -1]$ Volt is applied to ports 1'-8' as shown in Figure 4.26(a). The circuit reduces to the one shown in Figure 4.26(b), resulting in the equivalent circuit of Figure 4.26(c). From inspection, it follows that the parameter $n = 4$ for mode b .



(a) Mode b of the first circuit in Figure 4.24



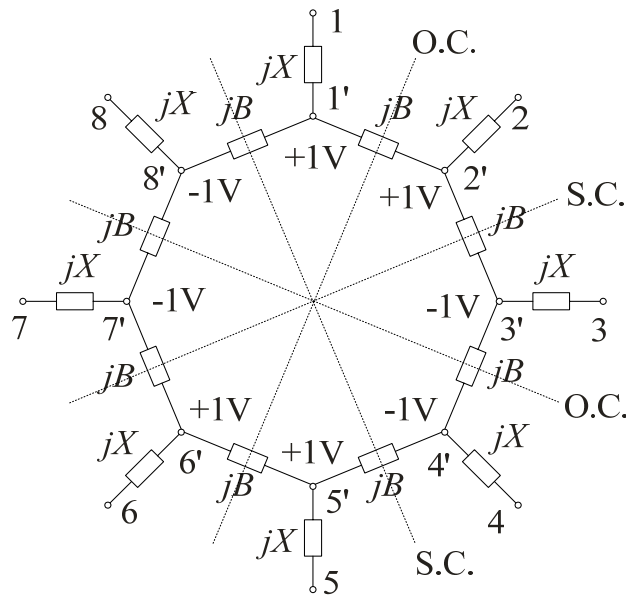
(b) Intermediate equivalent circuit for mode b



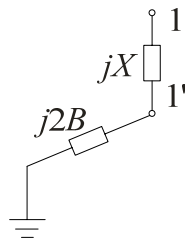
(c) Equivalent circuit for mode b

Figure 4.26 Equivalent circuit of the first circuit in Figure 4.24 for mode b

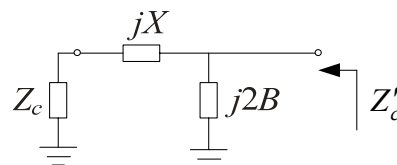
Then, we consider modes c and d of the first circuit in Figure 4.24. Since the eigenvector is $\mathbf{e}_c = [1, 1, -1, -1, 1, 1, -1, -1]^T$, $\mathbf{V} = [1, 1, -1, -1, 1, 1, -1, -1]$ Volt is applied to ports 1'-8' as shown in Figure 4.27(a). The circuit reduces to the one shown in Figure 4.27(b), resulting in the equivalent circuit of Figure 4.27(c). From inspection, it follows that the parameter $n = 2$ for modes c and d .



(a) Modes c and d of the first circuit in Figure 4.24



(b) Intermediate equivalent circuit for modes c and d



(c) Equivalent circuit for modes c and d

Figure 4.27 Equivalent circuit of the first circuit in Figure 4.24 for modes c and d

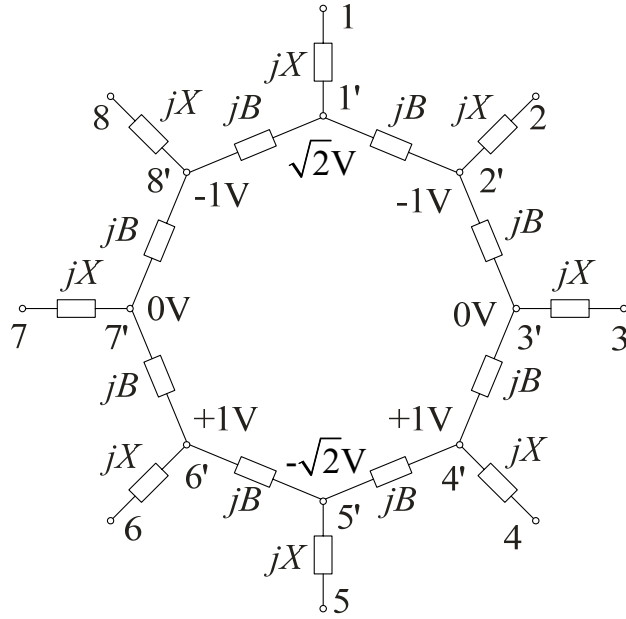
However, for modes e, f, g and h of the first circuit in Figure 4.24, we have to use a different approach to obtain the equivalent circuit. Let's consider modes e and f first. Since the eigenvector of mode e is $\mathbf{e}_e = [\sqrt{2}, -1, 0, 1, -\sqrt{2}, 1, 0, -1]^T$, an excitation vector $\mathbf{V} = [\sqrt{2}, -1, 0, 1, -\sqrt{2}, 1, 0, -1]$ Volt is applied to ports 1'-8' as shown in Figure 4.28(a). If a port has a voltage of 0 V, it can be grounded to earth. Assume the ports 1-8 are terminated in an impedance of Z_e . Then the circuit in Figure 4.28(a) reduces to the one in Figure 4.28(b). Therefore, the current I can be calculated as

$$\begin{aligned} I &= \frac{\sqrt{2}}{Z_e + jX} + 2 \times (\sqrt{2} + 1)jB \\ &= \frac{\sqrt{2}}{Z_e + jX} + \sqrt{2} \times (2 + \sqrt{2})jB \end{aligned} \quad (4.30)$$

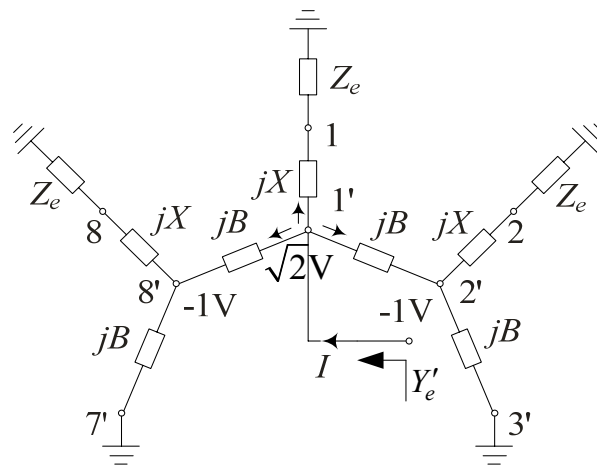
Then the input admittance is

$$Y'_e = \frac{I}{\sqrt{2}} = \frac{1}{Z_e + jX} + (2 + \sqrt{2})jB. \quad (4.31)$$

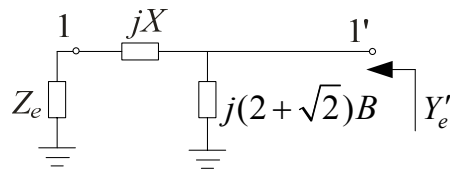
From the Equation (4.31) and Figure 4.28(c), it can be concluded that the equivalent circuit for modes e and f is the circuit in Figure 4.28(d). From inspection, it follows that the parameter $n = 2 + \sqrt{2}$ for modes e and f .



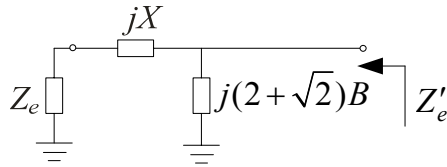
(a) Modes e and f of the first circuit in Figure 4.24



(b) Intermediate circuit



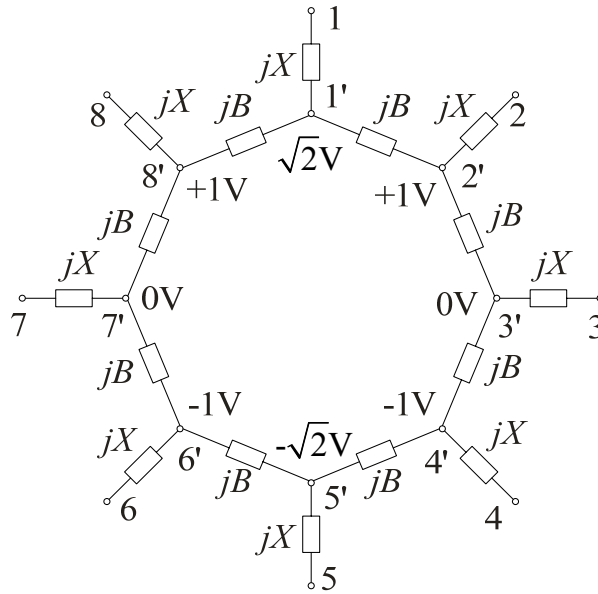
(c) Equivalent circuit of intermediate circuit



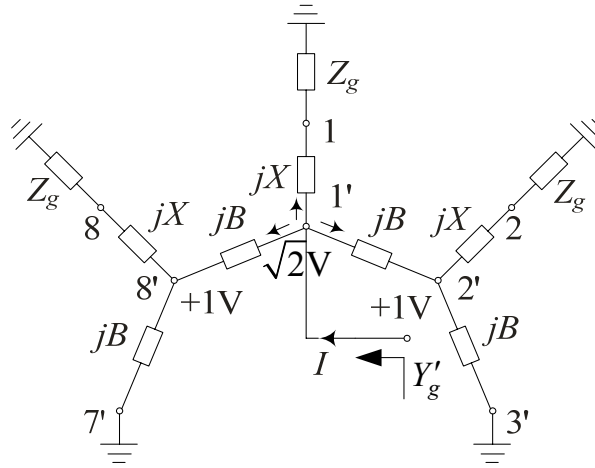
(d) Equivalent circuit for modes e and f

Figure 4.28 Equivalent circuit of the first circuit in Figure 4.24 for modes e and f

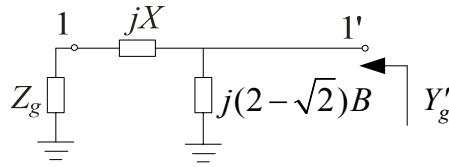
Finally, let us consider modes g and h of the first circuit in Figure 4.24. Since the eigenvector of mode g is $\mathbf{e}_g = [\sqrt{2}, 1, 0, -1, -\sqrt{2}, -1, 0, 1]^T$, an excitation vector $\mathbf{V} = [\sqrt{2}, 1, 0, -1, -\sqrt{2}, -1, 0, 1]$ Volt is applied to ports 1'-8' as shown in Figure 4.29(a). The circuit reduces to the one in Figure 4.29(b)



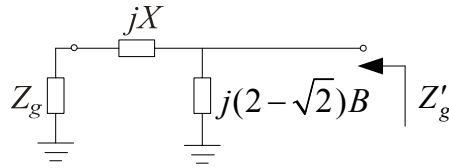
(a) Modes g and h of the first circuit in Figure 4.24



(b) Intermediate circuit



(c) Equivalent circuit of intermediate circuit



(d) Equivalent circuit for modes g and h

Figure 4.29 Equivalent circuit of the first circuit in Figure 4.24 for modes g and h

Similar to modes e and f , the current I can be calculated as

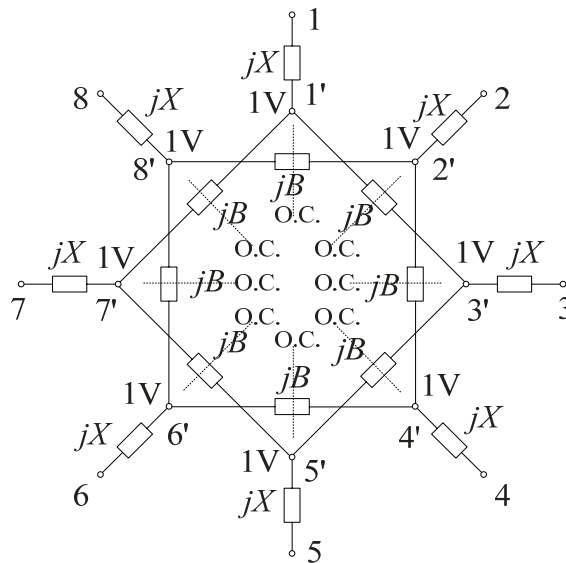
$$\begin{aligned}
 I &= \frac{\sqrt{2}}{Z_g + jX} + 2 \times (\sqrt{2} - 1)jB \\
 &= \frac{\sqrt{2}}{Z_g + jX} + \sqrt{2} \times (2 - \sqrt{2})jB
 \end{aligned} \tag{4.32}$$

Then the input admittance is

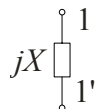
$$Y'_g = \frac{I}{\sqrt{2}} = \frac{1}{Z_g + jX} + (2 - \sqrt{2})jB. \tag{4.33}$$

From the Equation (4.33) and Figure 4.29(c), it can be concluded that the equivalent circuit for modes g and h is the circuit in Figure 4.29(d). From inspection, it follows that the parameter $n = 2 - \sqrt{2}$ for modes g and h .

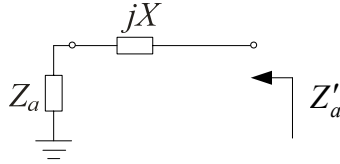
Now the equivalent circuits of the first circuit in Figure 4.24 have been derived for all modes. In the same way, the equivalent circuits of other circuits in Figure 4.24 for different modes can be obtained and are shown in Figures 4.30-4.34, Figures 4.35-4.39 and Figures 4.40-4.44 respectively. The results are then summarized in Table 4.5.



(a) Mode a of the second circuit in Figure 4.24

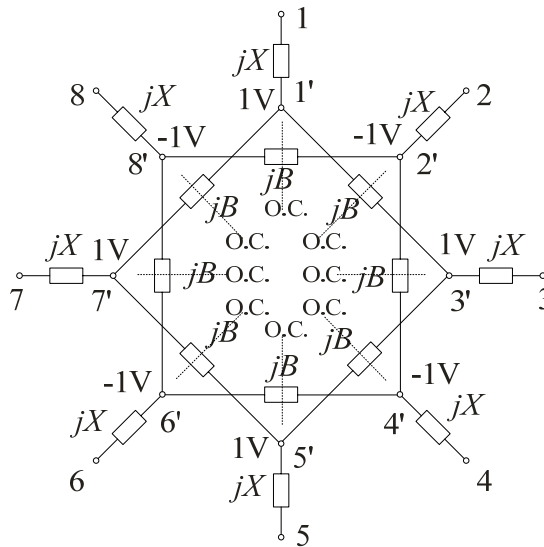


(b) Intermediate equivalent circuit for mode a

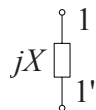


(c) Equivalent circuit for mode a

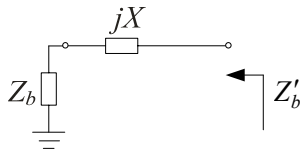
Figure 4.30 Equivalent circuit of the second circuit in Figure 4.24 for mode a



(a) Mode b of the second circuit in Figure 4.24

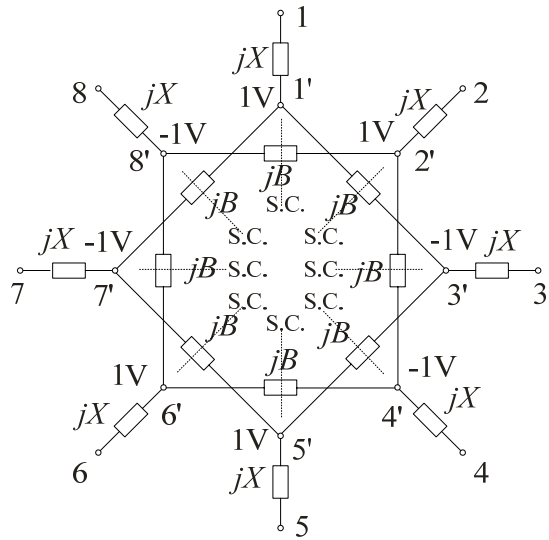


(b) Intermediate equivalent circuit for mode b

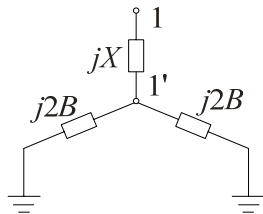


(c) Equivalent circuit for mode b

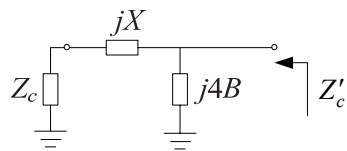
Figure 4.31 Equivalent circuit of the second circuit in Figure 4.24 for mode b



(a) Modes *c* and *d* of the second circuit in Figure 4.24

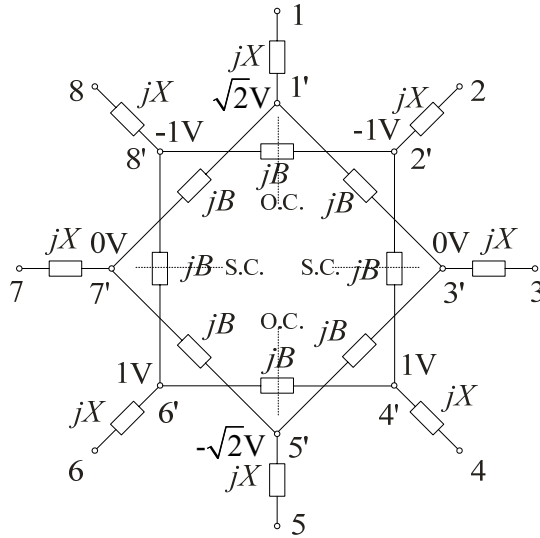


(b) Intermediate equivalent circuit for modes *c* and *d*

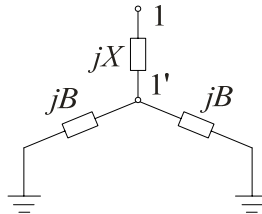


(c) Equivalent circuit for modes *c* and *d*

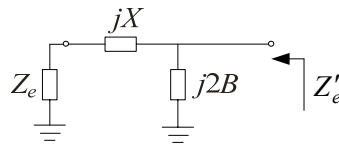
Figure 4.32 Equivalent circuit of the second circuit in Figure 4.24 for modes *c* and *d*



(a) Modes e and f of the second circuit in Figure 4.24

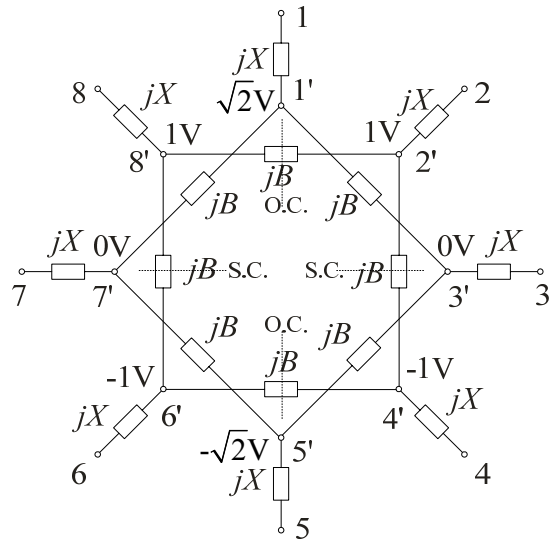


(b) Intermediate equivalent circuit for modes e and f

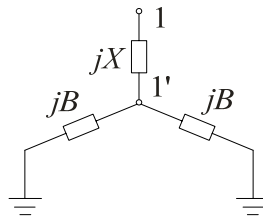


(c) Equivalent circuit for modes e and f

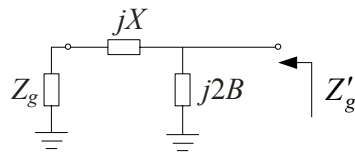
Figure 4.33 Equivalent circuit of the second circuit in Figure 4.24 for modes e and f



(a) Modes g and h of the second circuit in Figure 4.24

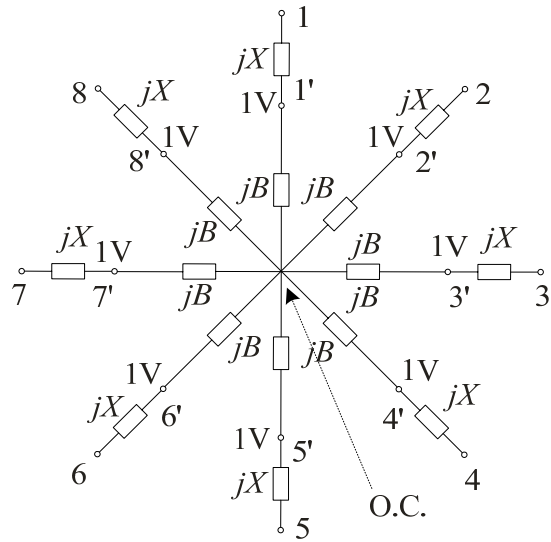


(b) Intermediate equivalent circuit for modes g and h

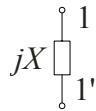


(c) Equivalent circuit for modes g and h

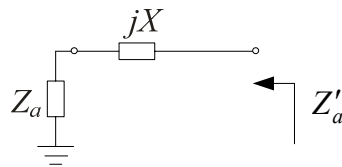
Figure 4.34 Equivalent circuit of the second circuit in Figure 4.24 for modes g and h



(a) Mode a of the third circuit in Figure 4.24

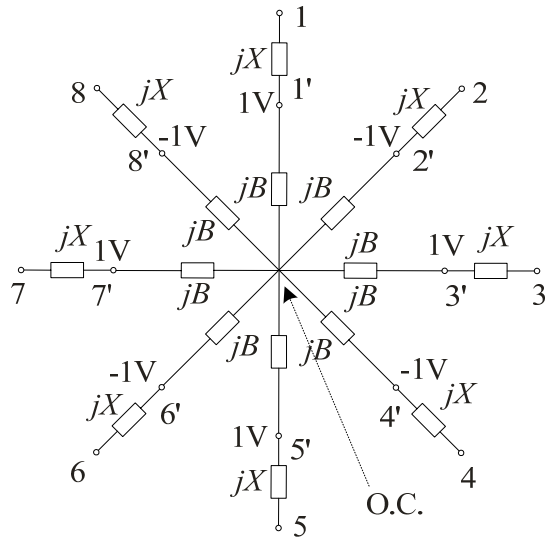


(b) Intermediate equivalent circuit for mode a

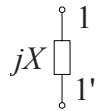


(c) Equivalent circuit for mode a

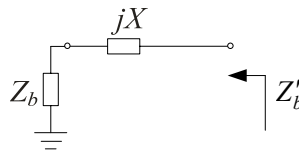
Figure 4.35 Equivalent circuit of the third circuit in Figure 4.24 for mode a



(a) Mode b of the third circuit in Figure 4.24

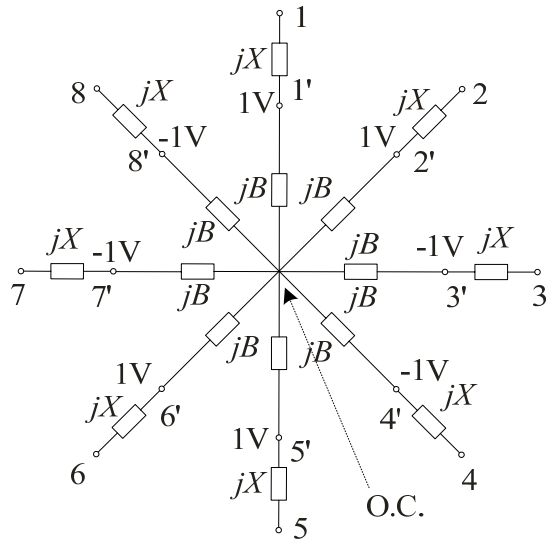


(b) Intermediate equivalent circuit for mode b

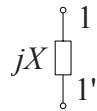


(c) Equivalent circuit for mode b

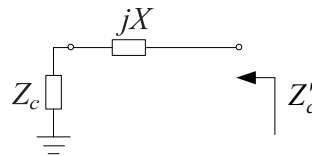
Figure 4.36 Equivalent circuit of the third circuit in Figure 4.24 for mode b



(a) Modes *c* and *d* of the third circuit in Figure 4.24

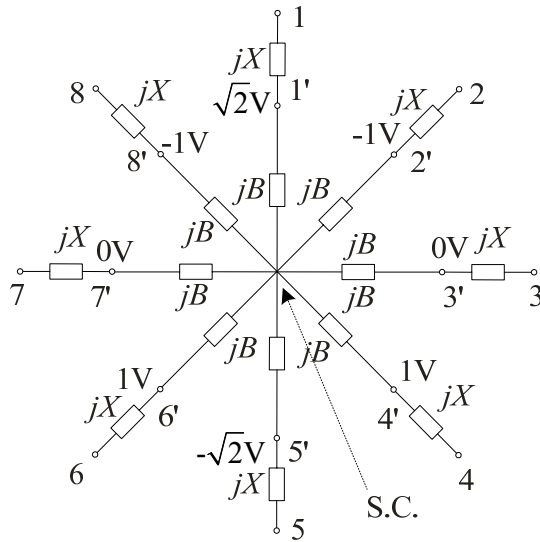


(b) Intermediate equivalent circuit for modes *c* and *d*

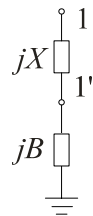


(c) Equivalent circuit for modes *c* and *d*

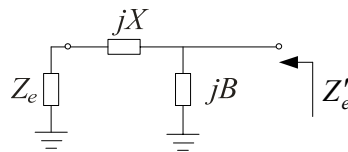
Figure 4.37 Equivalent circuit of the third circuit in Figure 4.24 for modes *c* and *d*



(a) Modes e and f of the third circuit in Figure 4.24

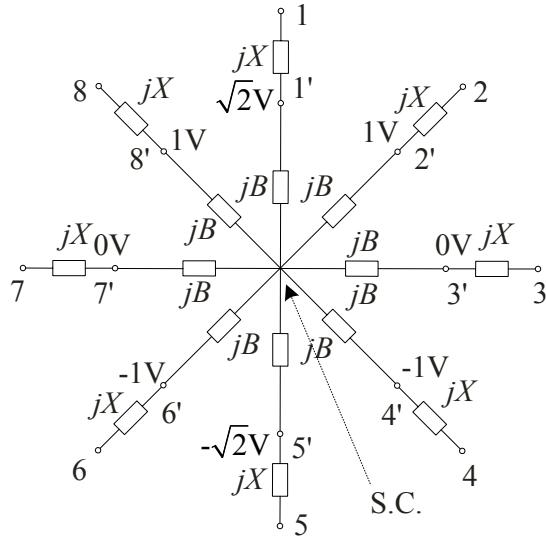


(b) Intermediate equivalent circuit for modes e and f

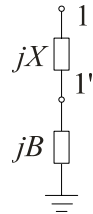


(c) Equivalent circuit for modes e and f

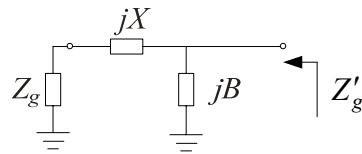
Figure 4.38 Equivalent circuit of the third circuit in Figure 4.24 for modes e and f



(a) Modes g and h of the third circuit in Figure 4.24

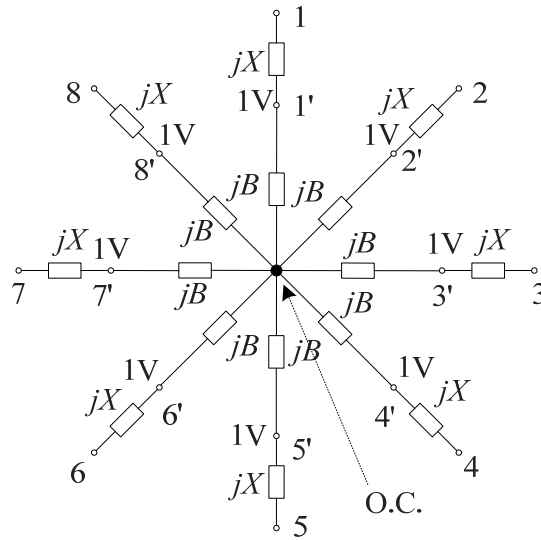


(b) Intermediate equivalent circuit for modes g and h

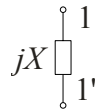


(c) Equivalent circuit for modes g and h

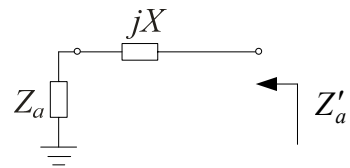
Figure 4.39 Equivalent circuit of the third circuit in Figure 4.24 for modes g and h



(a) Mode a of the fourth circuit in Figure 4.24

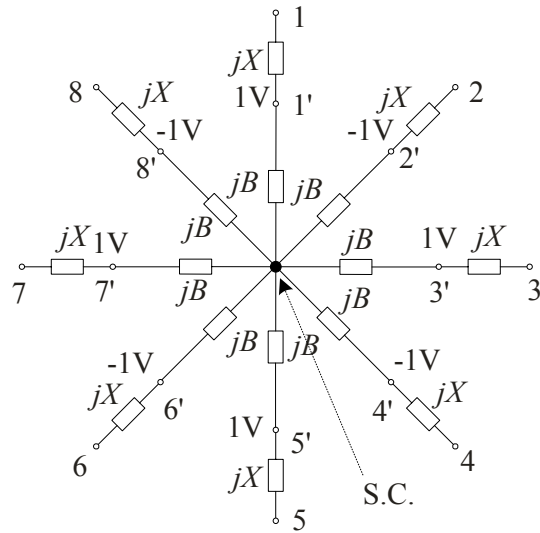


(b) Intermediate equivalent circuit for mode a

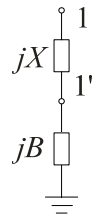


(c) Equivalent circuit for mode a

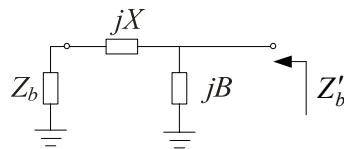
Figure 4.40 Equivalent circuit of the fourth circuit in Figure 4.24 for mode a



(a) Mode b of the fourth circuit in Figure 4.24

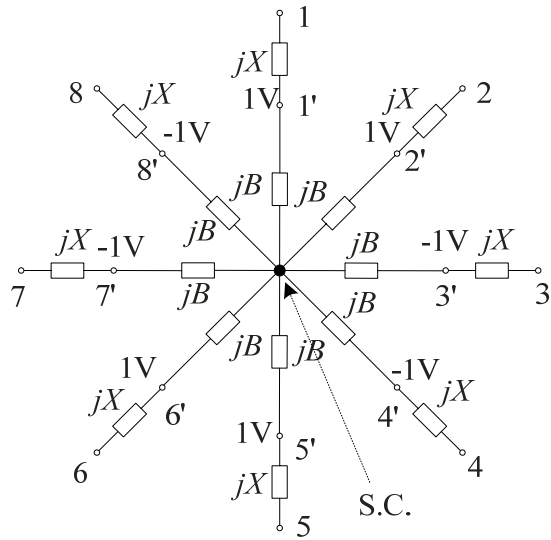


(b) Intermediate equivalent circuit for mode b

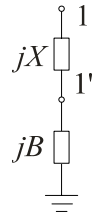


(c) Equivalent circuit for mode b

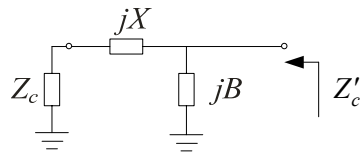
Figure 4.41 Equivalent circuit of the fourth circuit in Figure 4.24 for mode b



(a) Modes c and d of the forth circuit in Figure 4.24

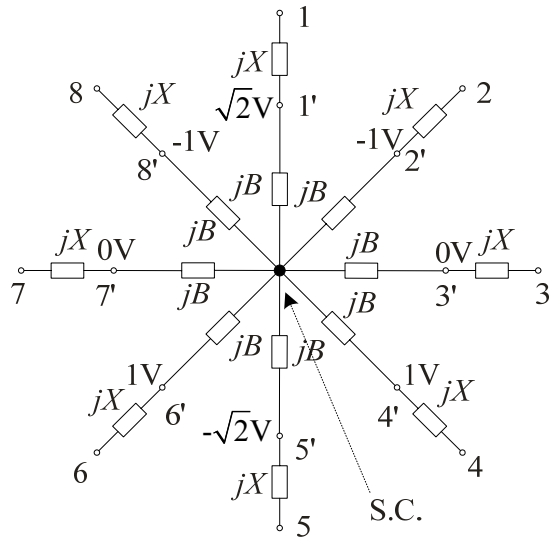


(b) Intermediate equivalent circuit for modes c and d

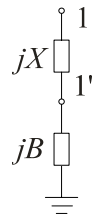


(c) Equivalent circuit for modes c and d

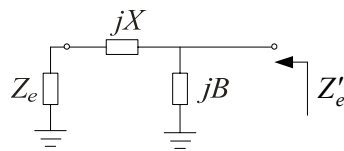
Figure 4.42 Equivalent circuit of the forth circuit in Figure 4.24 for modes c and d



(a) Modes e and f of the fourth circuit in Figure 4.24

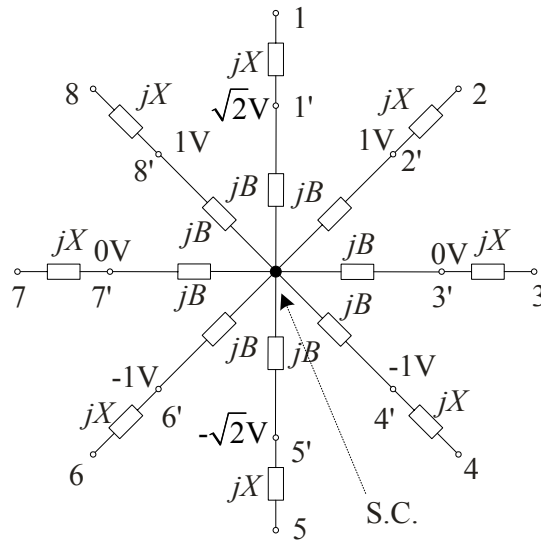


(b) Intermediate equivalent circuit for modes e and f

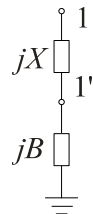


(c) Equivalent circuit for modes e and f

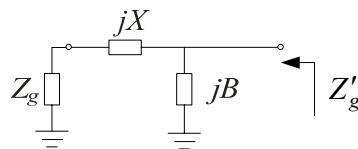
Figure 4.43 Equivalent circuit of the fourth circuit in Figure 4.24 for modes e and f



(a) Modes g and h of the forth circuit in Figure 4.24



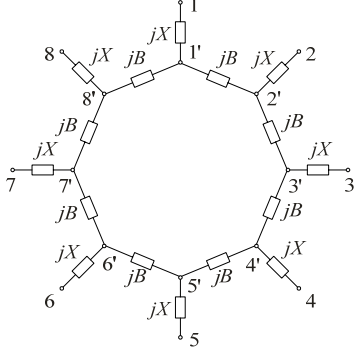
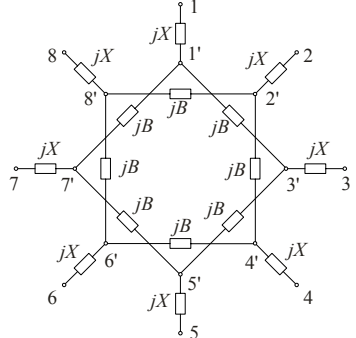
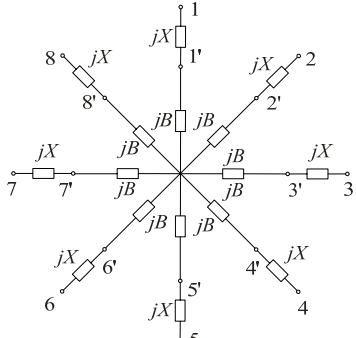
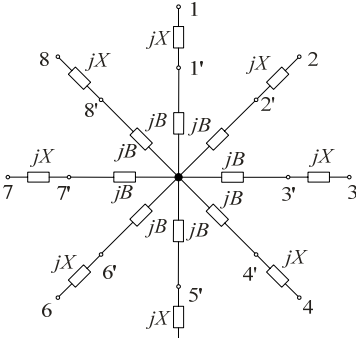
(b) Intermediate equivalent circuit for modes g and h



(c) Equivalent circuit for modes g and h

Figure 4.44 Equivalent circuit of the forth circuit in Figure 4.24 for modes g and h

Table 4.5 Basic circuit configurations for mode decoupling

Circuit	Parameter n
	<p>Mode a: $n = 0$</p> <p>Mode b: $n = 4$</p> <p>Modes c, d: $n = 2$</p> <p>Modes e, f: $n = 2 + \sqrt{2}$</p> <p>Modes g, h: $n = 2 - \sqrt{2}$</p>
	<p>Modes a, b: $n = 0$</p> <p>Modes c, d: $n = 4$</p> <p>Modes e, f, g, h: $n = 2$</p>
	<p>Modes a, b, c, d: $n = 0$</p> <p>Modes e, f, g, h: $n = 1$</p>
	<p>Mode a: $n = 0$</p> <p>Modes b, c, d, e, f, g, h: $n = 1$</p>

From Table 4.5, it is clear that the first circuit can be used to decouple mode groups (e , f) and (g , h), the second circuit to decouple mode groups b and (c , d), then the third circuit to decouple mode groups (b , c , d) and (e , f , g , h) and finally the fourth circuit to decouple mode groups a and (b , c , d , e , f , g , h). Details of the design of decoupling circuit are as follows.

Circuit shown in Figure 4.45(1) is used to decouple mode groups (e , f) and (g , h). Based on the equivalent circuits for these modes, the circuit elements are given by $X_1 = g(Z_e, Z_g)$ and $B_1 = h(Z_e, 2 + \sqrt{2}, Z_g, 2 - \sqrt{2}, X_1)$, where functions g and h are defined in Equations (4.11) and (4.12).

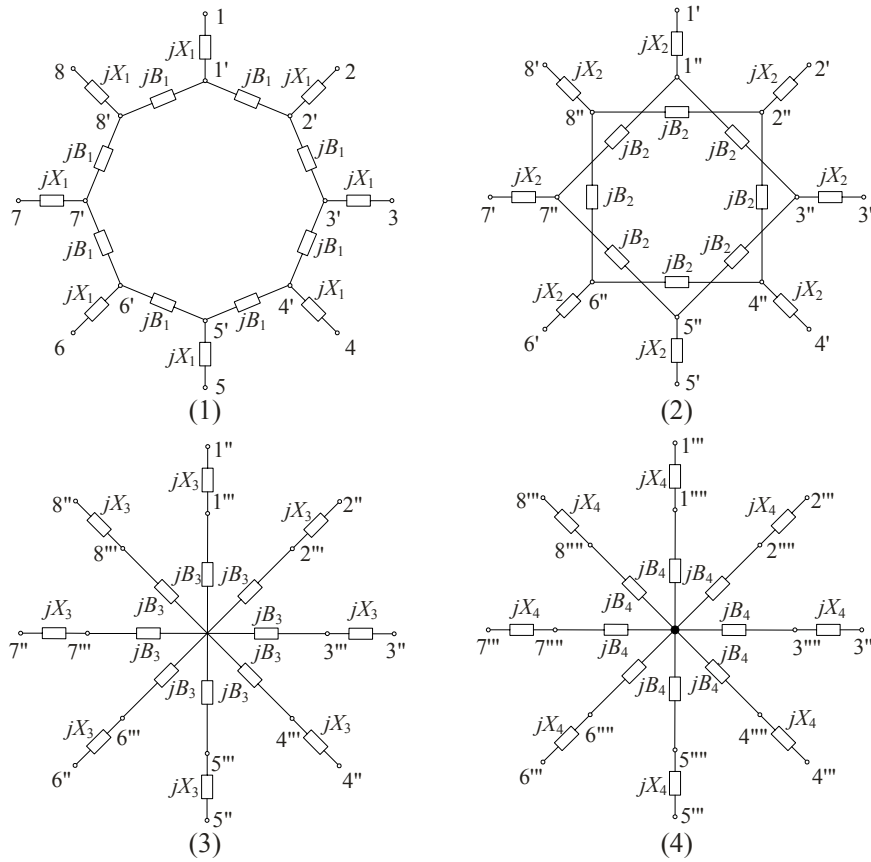


Figure 4.45 Decoupling circuit for 8-element array

The new impedance parameters as seen from ports 1'-8' in Figure 4.45(1) are given by

$$\mathbf{Z}' = ((\mathbf{Z}^a + \mathbf{Z}_1)^{-1} + \mathbf{Y}_1)^{-1}, \quad (4.34)$$

where \mathbf{Z}_1 and \mathbf{Y}_1 in (4.34) are defined by

$$\mathbf{Z}_1 = \text{diag}[jX_i, jX_i, jX_i, jX_i, jX_i, jX_i, jX_i, jX_i], \quad (4.35)$$

and

$$\mathbf{Y}_1 = \begin{bmatrix} j2B_1 & -jB_1 & 0 & 0 & 0 & 0 & 0 & -jB_1 \\ -jB_1 & j2B_1 & -jB_1 & 0 & 0 & 0 & 0 & 0 \\ 0 & -jB_1 & j2B_1 & -jB_1 & 0 & 0 & 0 & 0 \\ 0 & 0 & -jB_1 & j2B_1 & -jB_1 & 0 & 0 & 0 \\ 0 & 0 & 0 & -jB_1 & j2B_1 & -jB_1 & 0 & 0 \\ 0 & 0 & 0 & 0 & -jB_1 & j2B_1 & -jB_1 & 0 \\ 0 & 0 & 0 & 0 & 0 & -jB_1 & j2B_1 & -jB_1 \\ -jB_1 & 0 & 0 & 0 & 0 & 0 & -jB_1 & j2B_1 \end{bmatrix}. \quad (4.36)$$

The eigenvalues for \mathbf{Z}' are then obtained as

$$\begin{aligned} Z'_a &= Z'_{11} + 2Z'_{12} + 2Z'_{13} + 2Z'_{14} + Z'_{15} \\ Z'_b &= Z'_{11} - 2Z'_{12} + 2Z'_{13} - 2Z'_{14} + Z'_{15} \\ Z'_c &= Z'_d = Z'_{11} - 2Z'_{13} + Z'_{15} \\ Z'_e &= Z'_f = Z'_g = Z'_h = Z'_{11} - \sqrt{2}Z'_{12} + \sqrt{2}Z'_{14} - Z'_{15} \end{aligned} \quad (4.37)$$

Note that modes e, f, g and h are now decoupled.

Subsequently, we decouple mode groups b and (c, d) using the circuit shown in Figure 4.45(2). From the equivalent circuits for these modes, circuit elements X_2 and B_2 can be calculated by $X_2 = g(Z'_b, Z'_c)$ and $B_2 = h(Z'_b, 0, Z'_c, 4, X_2)$. The impedance parameters as seen from ports 1''-8'' in Figure 4.45(2) are given by

$$\mathbf{Z}'' = ((\mathbf{Z}' + \mathbf{Z}_2)^{-1} + \mathbf{Y}_2)^{-1}, \quad (4.38)$$

where \mathbf{Z}_2 is defined by Equation (4.35), and

$$\mathbf{Y}_2 = \begin{bmatrix} j2B_2 & 0 & -jB_2 & 0 & 0 & 0 & -jB_2 & 0 \\ 0 & j2B_2 & 0 & -jB_2 & 0 & 0 & 0 & -jB_2 \\ -jB_2 & 0 & j2B_2 & 0 & -jB_2 & 0 & 0 & 0 \\ 0 & -jB_2 & 0 & j2B_2 & 0 & -jB_2 & 0 & 0 \\ 0 & 0 & -jB_2 & 0 & j2B_2 & 0 & -jB_2 & 0 \\ 0 & 0 & 0 & -jB_2 & 0 & j2B_2 & 0 & -jB_2 \\ -jB_2 & 0 & 0 & 0 & -jB_2 & 0 & j2B_2 & 0 \\ 0 & -jB_2 & 0 & 0 & 0 & -jB_2 & 0 & j2B_2 \end{bmatrix}. \quad (4.39)$$

Then, the eigenvalues of \mathbf{Z}'' are as

$$\begin{aligned} Z''_a &= Z''_{11} + 2Z''_{12} + 2Z''_{13} + 2Z''_{14} + Z''_{15} \\ Z''_b &= Z''_c = Z''_d = Z''_{11} - 2Z''_{12} + 2Z''_{13} - 2Z''_{14} + Z''_{15} \\ Z''_e &= Z''_f = Z''_g = Z''_h = Z''_{11} - \sqrt{2}Z''_{12} + \sqrt{2}Z''_{14} - Z''_{15} \end{aligned} \quad (4.40)$$

Then, mode groups (b, c, d) and (e, f, g, h) are decoupled with circuit shown in Figure 4.45(3). From the equivalent circuits for these modes, it follows that $X_3 = g(Z''_b, Z''_e)$ and $B_3 = h(Z''_b, 0, Z''_e, 1, X_3)$. The impedance parameters as seen from ports 1''-8'' are then given by

$$\mathbf{Z}''' = ((\mathbf{Z}'' + \mathbf{Z}_3)^{-1} + \mathbf{Y}_3)^{-1}, \quad (4.41)$$

where \mathbf{Z}_3 is defined by Equation (4.35) and

$$\mathbf{Y}_3 = \begin{bmatrix} \frac{j}{2}B_3 & 0 & 0 & 0 & -\frac{j}{2}B_3 & 0 & 0 & 0 \\ 0 & \frac{j}{2}B_3 & 0 & 0 & 0 & -\frac{j}{2}B_3 & 0 & 0 \\ 0 & 0 & \frac{j}{2}B_3 & 0 & 0 & 0 & -\frac{j}{2}B_3 & 0 \\ 0 & 0 & 0 & \frac{j}{2}B_3 & 0 & 0 & 0 & -\frac{j}{2}B_3 \\ -\frac{j}{2}B_3 & 0 & 0 & 0 & \frac{j}{2}B_3 & 0 & 0 & 0 \\ 0 & -\frac{j}{2}B_3 & 0 & 0 & 0 & \frac{j}{2}B_3 & 0 & 0 \\ 0 & 0 & -\frac{j}{2}B_3 & 0 & 0 & 0 & \frac{j}{2}B_3 & 0 \\ 0 & 0 & 0 & -\frac{j}{2}B_3 & 0 & 0 & 0 & \frac{j}{2}B_3 \end{bmatrix}. \quad (4.42)$$

The eigenvalues of \mathbf{Z}''' are as

$$\begin{aligned} Z_a''' &= Z_{11}''' + 2Z_{12}''' + 2Z_{13}''' + 2Z_{14}''' + Z_{15}''' \\ Z_b''' = Z_c''' = Z_d''' = Z_e''' = Z_f''' = Z_g''' = Z_h''' &= Z_{11}''' - 2Z_{12}''' + 2Z_{13}''' - 2Z_{14}''' + Z_{15}''' \end{aligned} \quad (4.43)$$

Finally, mode groups a and (b, c, d, e, f, g, h) are decoupled using the circuit shown in Figure 4.45(4). Based on the equivalent circuits for these modes, circuit elements X_4 and B_4 can be got by $X_4 = g(Z_a''', Z_b''')$ and $B_4 = h(Z_a''', 0, Z_b''', 1, X_4)$. The impedance parameters as seen from ports 1''''-8'''' are then given by

$$\mathbf{Z}'''' = ((\mathbf{Z}''' + \mathbf{Z}_4)^{-1} + \mathbf{Y}_4)^{-1}, \quad (4.44)$$

where \mathbf{Z}_4 is defined by Equation (4.35) and

$$\mathbf{Y}_4 = \begin{bmatrix} j\frac{7}{8}B_4 & -\frac{j}{8}B_4 & -\frac{j}{8}B_4 & -\frac{j}{8}B_4 & -\frac{j}{8}B_4 & -\frac{j}{8}B_4 & -\frac{j}{8}B_4 & -\frac{j}{8}B_4 \\ -\frac{j}{8}B_4 & j\frac{7}{8}B_4 & -\frac{j}{8}B_4 & -\frac{j}{8}B_4 & -\frac{j}{8}B_4 & -\frac{j}{8}B_4 & -\frac{j}{8}B_4 & -\frac{j}{8}B_4 \\ -\frac{j}{8}B_4 & -\frac{j}{8}B_4 & j\frac{7}{8}B_4 & -\frac{j}{8}B_4 & -\frac{j}{8}B_4 & -\frac{j}{8}B_4 & -\frac{j}{8}B_4 & -\frac{j}{8}B_4 \\ -\frac{j}{8}B_4 & -\frac{j}{8}B_4 & -\frac{j}{8}B_4 & j\frac{7}{8}B_4 & -\frac{j}{8}B_4 & -\frac{j}{8}B_4 & -\frac{j}{8}B_4 & -\frac{j}{8}B_4 \\ -\frac{j}{8}B_4 & -\frac{j}{8}B_4 & -\frac{j}{8}B_4 & -\frac{j}{8}B_4 & j\frac{7}{8}B_4 & -\frac{j}{8}B_4 & -\frac{j}{8}B_4 & -\frac{j}{8}B_4 \\ -\frac{j}{8}B_4 & -\frac{j}{8}B_4 & -\frac{j}{8}B_4 & -\frac{j}{8}B_4 & -\frac{j}{8}B_4 & j\frac{7}{8}B_4 & -\frac{j}{8}B_4 & -\frac{j}{8}B_4 \\ -\frac{j}{8}B_4 & -\frac{j}{8}B_4 & -\frac{j}{8}B_4 & -\frac{j}{8}B_4 & -\frac{j}{8}B_4 & -\frac{j}{8}B_4 & j\frac{7}{8}B_4 & -\frac{j}{8}B_4 \\ -\frac{j}{8}B_4 & -\frac{j}{8}B_4 & -\frac{j}{8}B_4 & -\frac{j}{8}B_4 & -\frac{j}{8}B_4 & -\frac{j}{8}B_4 & -\frac{j}{8}B_4 & j\frac{7}{8}B_4 \end{bmatrix}. \quad (4.45)$$

Now, all modes are then matched since

$$Z_a'''' = Z_b'''' = Z_c'''' = Z_d'''' = Z_e'''' = Z_f'''' = Z_g'''' = Z_h'''' = Z_{11}'''' . \quad (4.46)$$

The new input ports will also be decoupled and will have the same input impedance. Again, the ports can be matched to the system impedance Z_0 using L section impedance matching networks [48] described in Section 3.6.1.3.

To verify the theory, a decoupling network for a specific 8-element monopole array was designed. The eight elements of the array were evenly distributed on a circle with radius of 15 mm (0.125λ at a center frequency of $f_0 = 2.5$ GHz). Each monopole had a length of 28 mm (0.23λ) and a diameter of 1mm (0.0083λ). With a system impedance of $Z_0 = 50 \Omega$, the array's S-parameters were computed using IE3D [52] and converted into impedance parameters using Equation (4.2). The scattering parameters of the array at f_0 and the computed decoupling network elements are specified in Table 4.6. The elements of the L section impedance matching networks are also shown, with B_5

being the susceptance of a parallel element to ground and X_5 the reactance of a series element.

Table 4.6 S-parameters and decoupling network elements for the 8-element array

Array scattering parameter	$S_{11}^a = -5.92 \text{ dB } \angle 167.6^\circ$ $S_{12}^a = -7.73 \text{ dB } \angle 13.8^\circ$ $S_{13}^a = -13.42 \text{ dB } \angle -27.9^\circ$ $S_{14}^a = -19.95 \text{ dB } \angle -85.0^\circ$ $S_{15}^a = -20.97 \text{ dB } \angle -126.5^\circ$
Decoupling network elements	$X_1 = -0.0602, B_1 = -0.1427$ $X_2 = -2.8225, B_2 = -1.3181$ $X_3 = -0.3403, B_3 = 58.6733$ $X_4 = -2.8642, B_4 = -0.3385$
Decoupled port impedance	$Z_a''' = 180.374 - j115.258\Omega$
Matching network elements	$B_5 = 0.005437, X_5 = 101.001$

The scattering parameters of the decoupled and matched array were calculated over a frequency range of $0.99f_0$ to $1.01f_0$ and shown in Figures 4.46. Again, the results shown clearly illustrate the validity of the theory. Simulations for the normalized azimuth radiation pattern of the 8-element array obtained by feeding the port 1 are shown in Figure 4.47. For excitation at successive ports, the radiation pattern will be rotated by 45° .

We successfully demonstrated the design of a decoupling network for an array with more than four elements, albeit over a narrow frequency range. The principles

presented in this chapter provide a framework for the systematic design of decoupling networks for symmetrical arrays. The procedure would theoretically be applicable to arrays of various sizes. However, implementation of the decoupling network for the examples of 6-element and 8-element array would require the use of multilayer circuits, and would be even more challenging for arrays with more elements.

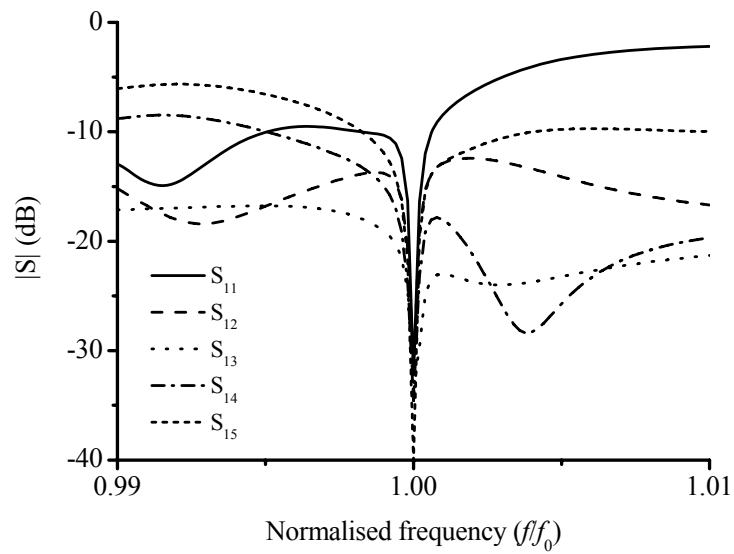


Figure 4.46 Scattering parameters of the decoupled and matched 8-element array

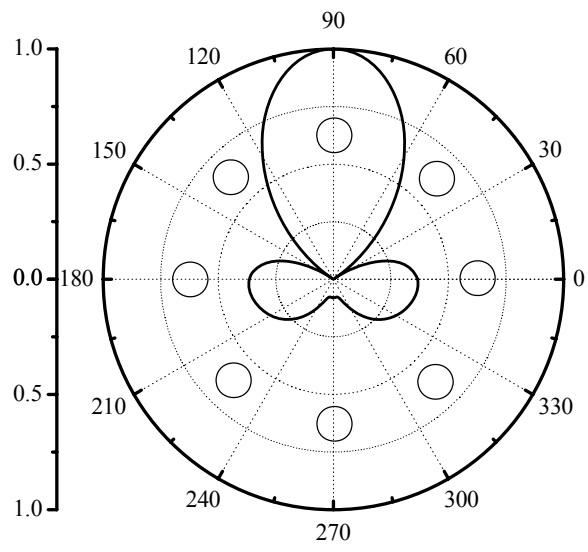


Figure 4.47 Normalized azimuth radiation pattern of the 8-element array

Chapter 5 Decoupling Network Design Using Modal Feed Network

5.1 Introduction

Design of decoupling network for arrays with arbitrary complex mutual admittances by applying eigenmode analysis and/or network analysis of the DN/array combination has been described in previous chapters. In this chapter, an alternative approach making use of the orthogonality of the eigenmodes of the array to achieve port decoupling is described and verified with experimental results.

5.2 The inspiration of the alternative design of decoupling network

The decoupling networks for 2- to 4-element arrays with arbitrary complex mutual admittances presented in [23-29] and previous two chapters are symmetrical networks with lossless reactive elements. These network elements were obtained by applying either an eigenmode analysis or a complete network analysis of the DN/array combination. Although those designs work well in decoupling an array, they still have some shortcomings need to improve.

The decoupling and matching network proposed before contains only lossless components such as inductors or capacitors. The values of those components are obtained by solving a number of equations. However, there may be no such commercial components with the calculated values when implementing the network. Therefore, the circuit has to be recalculated if lumped elements are going to be used. However, it is not guaranteed that suitable values can be obtained every time. Usually the lossless reactive components have to be converted to realizable microstrip line or stripline by exploiting Kuroda's identities [48-51]. Although the lines can be

meandered, the overall size of the decoupling and matching network is usually relatively large and it makes the design difficult to be applied in many mobile handsets, as in [28].

Therefore, new decoupling technique is demanded. An alternative approach was developed to achieve port decoupling which involves the use of a modal feed network. Isolation between the new input ports is achieved by exploiting the inherent orthogonality of the eigenmodes of the array [53-56]. The input ports to the feed network and array combination can then be matched independently. In digital beam forming applications, the required element weights are obtained as a linear combination of the orthogonal eigenmode vectors. This new approach is easy to understand and provides a simple design procedure of decoupling. Details of this decoupling approach will be described in the following sections.

5.3 Theory and design of modal feed network

5.3.1 S-parameters of feed network and array combination

Consider an $(M+N)$ -port passive feed network connected to an N -element array, as shown in Figure 5.1. We denote the first M ports as the external ports and the remaining N ports as the internal ports, which are connected to the array. We assume that the array can be modeled as an N -port network with scattering parameter matrix \mathbf{S}^a , which is independent of the element excitation. The scattering parameters of the combination of the feed network and the array can then be obtained by following the multiport connection method [57]. The scattering parameter relation $\mathbf{b} = \mathbf{S}\mathbf{a}$ for the feed network is separated into two groups, the first corresponding to the M external ports (denoted by \mathbf{e}) and the second corresponding to the N internally connected ports

(denoted by \mathbf{i}):

$$\begin{bmatrix} \mathbf{b}_e \\ \mathbf{b}_i \end{bmatrix} = \begin{bmatrix} \mathbf{S}_{ee} & \mathbf{S}_{ei} \\ \mathbf{S}_{ie} & \mathbf{S}_{ii} \end{bmatrix} \begin{bmatrix} \mathbf{a}_e \\ \mathbf{a}_i \end{bmatrix}, \quad (5.1)$$

where \mathbf{S}_{ee} , $\mathbf{S}_{ei} = \mathbf{S}_{ie}^T$ and \mathbf{S}_{ii} are $M \times M$, $M \times N$ and $N \times N$ sub-matrices, while \mathbf{a}_e , \mathbf{b}_e and \mathbf{a}_i , \mathbf{b}_i are column vectors of dimension M and N respectively. Since the internal ports are connected directly to the array, we have that

$$\mathbf{a}_i = \mathbf{S}^a \mathbf{b}_i. \quad (5.2)$$

Combining (5.2) and the second relation of (5.1) yields

$$(\mathbf{S}^a)^{-1} \mathbf{a}_i = \mathbf{S}_{ie} \mathbf{a}_e + \mathbf{S}_{ii} \mathbf{a}_i, \quad (5.3)$$

so that

$$\mathbf{a}_i = [(\mathbf{S}^a)^{-1} - \mathbf{S}_{ii}]^{-1} \mathbf{S}_{ie} \mathbf{a}_e. \quad (5.4)$$

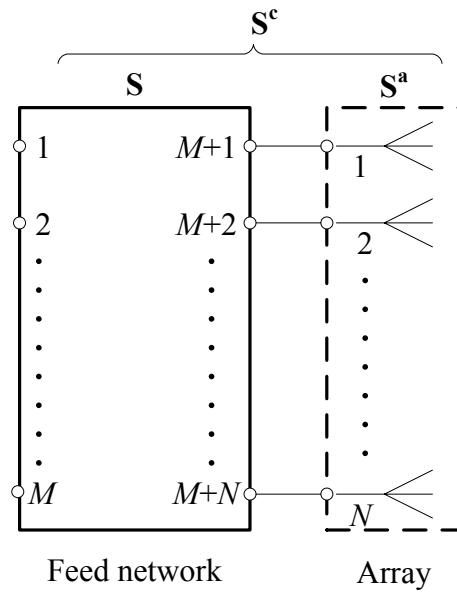


Figure 5.1 $(M+N)$ -port feed network connected to an N -element array

Substituting (5.4) into the first relation of (5.1) gives

$$\mathbf{b}_e = \left\{ \mathbf{S}_{ee} + \mathbf{S}_{ei} [(\mathbf{S}^a)^{-1} - \mathbf{S}_{ii}]^{-1} \mathbf{S}_{ie} \right\} \mathbf{a}_e = \mathbf{S}^c \mathbf{a}_e, \quad (5.5)$$

where \mathbf{S}^c is the $M \times M$ scattering parameter matrix of the feed network and array combination.

5.3.2 Ideal modal feed network

Now consider a so-called modal feed network with $2N$ ports. The modal feed network has N external ports and the remaining N internal ports are connected to an N -port array of uniformly spaced, identical elements. The feed network produces the n th eigenvector of \mathbf{S}^a at the internal ports in response to an input signal at external port n .

An ideal modal feed network will have the following characteristics:

$$\mathbf{S}_{ee} = \mathbf{S}_{ii} = \mathbf{0}, \quad (5.6)$$

$$\mathbf{S}_{ie} = [\mathbf{e}_1 \ \mathbf{e}_2 \ \dots \ \mathbf{e}_N], \quad (5.7)$$

$$\mathbf{S}_{ei} = \mathbf{S}_{ie}^T = \mathbf{S}_{ie}^{-1}, \quad (5.8)$$

where column vector \mathbf{e}_m is the m th orthonormal eigenvector of the array scattering parameter matrix \mathbf{S}^a . Note that \mathbf{S}_{ie} is the orthogonal matrix which diagonalizes \mathbf{S}^a .

The S-parameters of the combined feed network and array are obtained by substituting (5.6), (5.7) and (5.8) into (5.5) to obtain

$$\begin{aligned} \mathbf{S}^c &= \mathbf{0} + \mathbf{S}_{ei}[(\mathbf{S}^a)^{-1} - \mathbf{0}]^{-1} \mathbf{S}_{ie} \\ &= \mathbf{S}_{ie}^{-1} \mathbf{S}^a \mathbf{S}_{ie} \\ &= \text{diag}[\lambda_1, \lambda_2, \dots, \lambda_N], \end{aligned} \quad (5.9)$$

where λ_m is the m th eigenvalue of \mathbf{S}^a . The input ports of the combined network are therefore decoupled ($\mathbf{S}_{ij}^c = 0, i \neq j$) but mismatched ($\mathbf{S}_{ii}^c \neq 0$). They can be matched individually by introducing appropriate matching networks.

For a desired element excitation $\mathbf{y} = [y_1, y_2, \dots, y_N]^T$, the signals required at the external ports of the modal feed network, $\mathbf{x} = [x_1, x_2, \dots, x_N]^T$, are obtained from

$$\mathbf{x} = \mathbf{S}_{ie}^{-1} \mathbf{y} = \mathbf{S}_{ei} \mathbf{y}. \quad (5.10)$$

To verify the modal feed network proposed, a symmetrical 2×2 monopole array is considered. The inter-element spacing for the monopoles is 15 mm. Each monopole consists of a copper wire which is 1 mm in diameter and 29 mm in length. The S-parameter at 2.6 GHz is

$$\mathbf{S}^a = \begin{bmatrix} 0.276 - j0.191 & -0.347 + j0.038 & -0.038 + j0.225 & -0.347 + j0.038 \\ -0.347 + j0.038 & 0.276 - j0.191 & -0.347 + j0.038 & -0.038 + j0.225 \\ -0.038 + j0.225 & -0.347 + j0.038 & 0.276 - j0.191 & -0.347 + j0.038 \\ -0.347 + j0.038 & -0.038 + j0.225 & -0.347 + j0.038 & 0.276 - j0.191 \end{bmatrix}. \quad (5.11)$$

Two different sets of S-parameters of the combination of the feed network and the array obtained from direct calculation and ADS [58] simulation are presented.

1). Direct calculation from Equation (5.9):

$$\begin{aligned} \mathbf{S}^c &= \text{diag}[\lambda_1, \lambda_2, \dots, \lambda_4] \\ &= \text{diag}[S_{11}^a + S_{12}^a + S_{13}^a + S_{14}^a, S_{11}^a + S_{12}^a - S_{13}^a - S_{14}^a, \\ &\quad S_{11}^a - S_{12}^a - S_{13}^a + S_{14}^a, S_{11}^a - S_{12}^a + S_{13}^a - S_{14}^a] \\ &= \begin{bmatrix} -0.456 + j0.11 & 0 & 0 & 0 \\ 0 & 0.314 - j0.416 & 0 & 0 \\ 0 & 0 & 0.314 - j0.416 & 0 \\ 0 & 0 & 0 & 0.932 - j0.042 \end{bmatrix} \end{aligned} \quad (5.12)$$

2). ADS simulation:

From (5.6)-(5.8), the ideal modal feed network for a 4-element array has S-parameters given by

$$\mathbf{S} = \frac{1}{2} \begin{bmatrix} 0 & 0 & 0 & 0 & 1 & 1 & 1 & 1 \\ 0 & 0 & 0 & 0 & 1 & 1 & -1 & -1 \\ 0 & 0 & 0 & 0 & 1 & -1 & -1 & 1 \\ 0 & 0 & 0 & 0 & 1 & -1 & 1 & -1 \\ 1 & 1 & 1 & 1 & 0 & 0 & 0 & 0 \\ 1 & 1 & -1 & -1 & 0 & 0 & 0 & 0 \\ 1 & -1 & -1 & 1 & 0 & 0 & 0 & 0 \\ 1 & -1 & 1 & -1 & 0 & 0 & 0 & 0 \end{bmatrix}. \quad (5.13)$$

The network configuration in ADS is shown in Figure 5.2. The 4-port block represents the antenna array and contains the data of (5.11), while the 8-port block represents the modal feed network and contains the data of (5.13). The S-parameter of the combination of feed network and array from ADS is shown in Table 5.1.

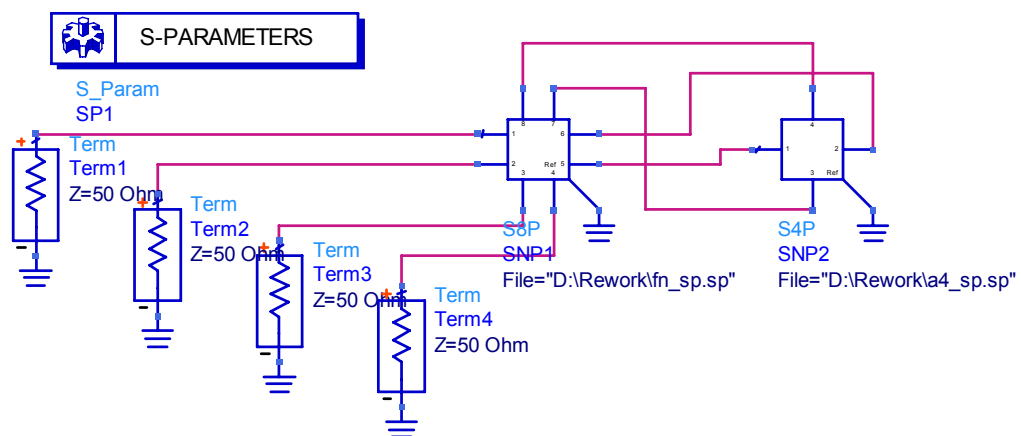


Figure 5.2 Network setup in ADS to verify modal feed network.

Table 5.1 Simulation results in ADS

freq	S(1,1)	S(1,2)	S(1,3)	S(1,4)
2.600 GHz	0.469 / 166.438	6.206E-17 / -26.565	1.522E-16 / -114.2...	1.299E-16 / -171.1...
freq	S(2,1)	S(2,2)	S(2,3)	S(2,4)
2.600 GHz	1.475E-16 / -48.814	0.521 / -52.954	1.388E-17 / 0.000	5.043E-17 / 63.435
freq	S(3,1)	S(3,2)	S(3,3)	S(3,4)
2.600 GHz	2.178E-16 / -30.651	1.739E-16 / 118.610	0.521 / -52.954	1.093E-16 / 1.818
freq	S(4,1)	S(4,2)	S(4,3)	S(4,4)
2.600 GHz	9.930E-16 / -116.56...	0.000 / 0.000	4.965E-16 / 153.435	0.933 / -2.580

The result in Table 5.1 is written in matrix as

$$\mathbf{S}^c = \begin{bmatrix} 0.469 \angle 166.44^\circ & 0 & 0 & 0 \\ 0 & 0.521 \angle -52.95^\circ & 0 & 0 \\ 0 & 0 & 0.521 \angle -52.95^\circ & 0 \\ 0 & 0 & 0 & 0.933 \angle -2.58^\circ \end{bmatrix}$$

$$= \begin{bmatrix} -0.456 + j0.11 & 0 & 0 & 0 \\ 0 & 0.314 - j0.416 & 0 & 0 \\ 0 & 0 & 0.314 - j0.416 & 0 \\ 0 & 0 & 0 & 0.932 - j0.042 \end{bmatrix}$$

(5.14)

It can be seen that Equation (5.14) is exactly the same as Equation (5.12), which was obtained from direct calculation.

5.3.3 Practical modal feed network

It is often more practical to implement a modal feed network which produces orthogonal output vectors, but with an additional phase shift ϕ_m associated with mode m . We still assume that $\mathbf{S}_{ee} \approx \mathbf{0}$ and $\mathbf{S}_{ii} \approx \mathbf{0}$, but here we have

$$\mathbf{S}_{ie} = \mathbf{P} \mathbf{\Phi}, \quad (5.15)$$

$$\mathbf{S}_{ei} = \mathbf{S}_{ie}^T = \mathbf{\Phi} \mathbf{P}^{-1}, \quad (5.16)$$

where

$$\mathbf{\Phi} = \text{diag}[e^{j\phi_1}, e^{j\phi_2}, \dots, e^{j\phi_N}], \quad (5.17)$$

and

$$\mathbf{P} = [\mathbf{e}_1 \ \mathbf{e}_2 \ \dots \ \mathbf{e}_N]. \quad (5.18)$$

The S-parameters of the N -port network resulting from connecting the modal feed network to the array are then given by

$$\begin{aligned} \mathbf{S}^c &= \mathbf{S}_{ei} \mathbf{S}^a \mathbf{S}_{ie} \\ &= \mathbf{\Phi} \mathbf{P}^{-1} \mathbf{S}^a \mathbf{P} \mathbf{\Phi} \\ &= \text{diag}[\lambda_1 e^{j2\phi_1}, \lambda_2 e^{j2\phi_2}, \dots, \lambda_N e^{j2\phi_N}]. \end{aligned} \quad (5.19)$$

The signals required at the external ports of the modal feed network are related to the desired element excitations via

$$\mathbf{x} = \mathbf{S}_{ie}^{-1} \mathbf{y} = \mathbf{\Phi}^* \mathbf{P}^T \mathbf{y}, \quad (5.20)$$

where $\mathbf{\Phi}^*$ is the conjugate of matrix $\mathbf{\Phi}$.

5.4 Results of design examples and discussion

To illustrate the principle, two practical examples are examined: a 2-element linear array and a 2×2 planar array. In both cases, the array elements are monopoles consisting of brass rods mounted on a 62 mil FR4 ($\epsilon_r = 4.4$) substrate. The upper metallization of the substrate acts as the ground plane, as shown in Figure 5.3. The elements are excited via microstrip lines etched on the bottom surface of the substrate.

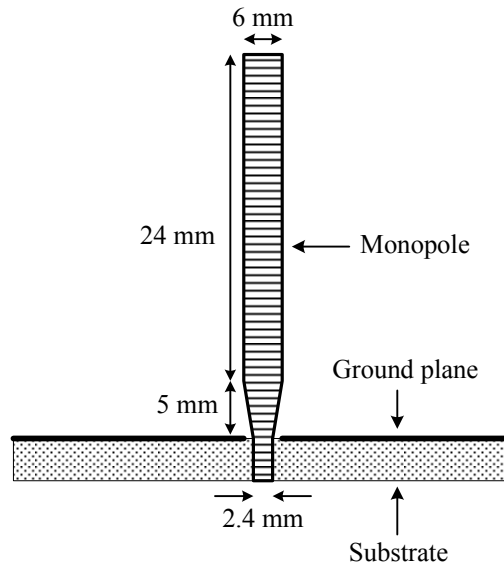


Figure 5.3 Monopole array element used in the construction of prototype arrays

5.4.1 Modal feed network for 2-element monopole array

The S-parameters of an array with two identical elements are given by

$$\mathbf{S}^a = \begin{bmatrix} S_{11}^a & S_{12}^a \\ S_{12}^a & S_{11}^a \end{bmatrix}. \quad (5.21)$$

The eigenvalues of \mathbf{S}^a are

$$\begin{aligned} \lambda_1 &= S_{11}^a + S_{12}^a \\ \lambda_2 &= S_{11}^a - S_{12}^a \end{aligned}, \quad (5.22)$$

while the orthonormal eigenvectors are given by

$$\begin{aligned} \mathbf{e}_1 &= \frac{1}{\sqrt{2}} \begin{bmatrix} 1 \\ 1 \end{bmatrix} \\ \mathbf{e}_2 &= \frac{1}{\sqrt{2}} \begin{bmatrix} 1 \\ -1 \end{bmatrix} \end{aligned}. \quad (5.23)$$

The modal feed network for such an array may be implemented as a rat-race 180°

hybrid. With port numbering as defined in Figure 5.4, the S-parameters of the hybrid are given by

$$\mathbf{S} = \frac{-j}{\sqrt{2}} \begin{bmatrix} 0 & 0 & 1 & 1 \\ 0 & 0 & 1 & -1 \\ 1 & 1 & 0 & 0 \\ 1 & -1 & 0 & 0 \end{bmatrix}. \quad (5.24)$$

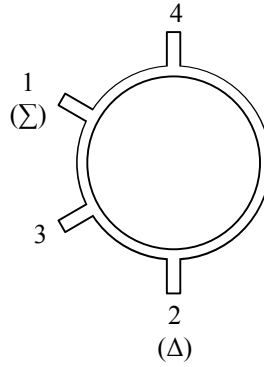


Figure 5.4 Port numbering for a rat-race 180° hybrid coupler which acts as modal feed network for the 2-element array

In this case, we find that in (5.17)

$$\phi_1 = \phi_2 = -90^\circ. \quad (5.25)$$

The S-parameters of the 2-port network resulting from connecting the hybrid to the array are obtained from (5.19) as

$$\mathbf{S}^c = \begin{bmatrix} -S_{11}^a - S_{12}^a & 0 \\ 0 & S_{12}^a - S_{11}^a \end{bmatrix}. \quad (5.26)$$

The combined network may then be matched by providing suitable matching circuits at ports 1 and 2.

A prototype monopole array with an element spacing of 0.1λ was fabricated, as

shown in Figure 5.5. The dimensions of antenna element of the monopole array are as what shown in Figure 5.3. The upper metallization of the substrate acts as the ground plane.

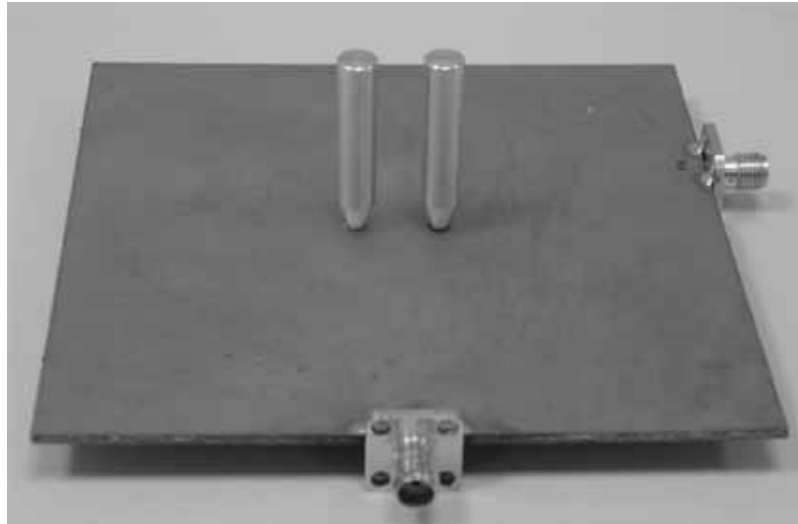


Figure 5.5 2-element monopole array mounted on a substrate

The scattering parameters of the array were measured using an Agilent Technologies 8510C Network Analyzer. The measured scattering parameters of the array are shown in Figure 5.6. The reflection coefficient is small, but a high level of mutual coupling of approximately -5 dB at 2.6 GHz is observed.

The modal feed network shown in Figure 5.7 (but without the matching stubs) was fabricated on the lower surface of the substrate and connected to the array. The S-parameters were again measured and the results are shown in Figure 5.8. The two ports are no longer matched, but according to (5.26), this is to be expected. However, the two ports are isolated, with the mutual coupling being less than -20 dB across the frequency band.

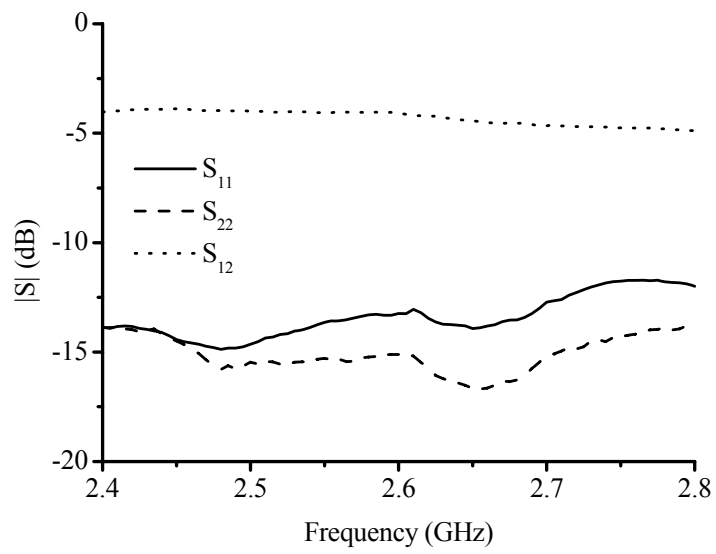


Figure 5.6 Measured S-parameters of the 2-element monopole array

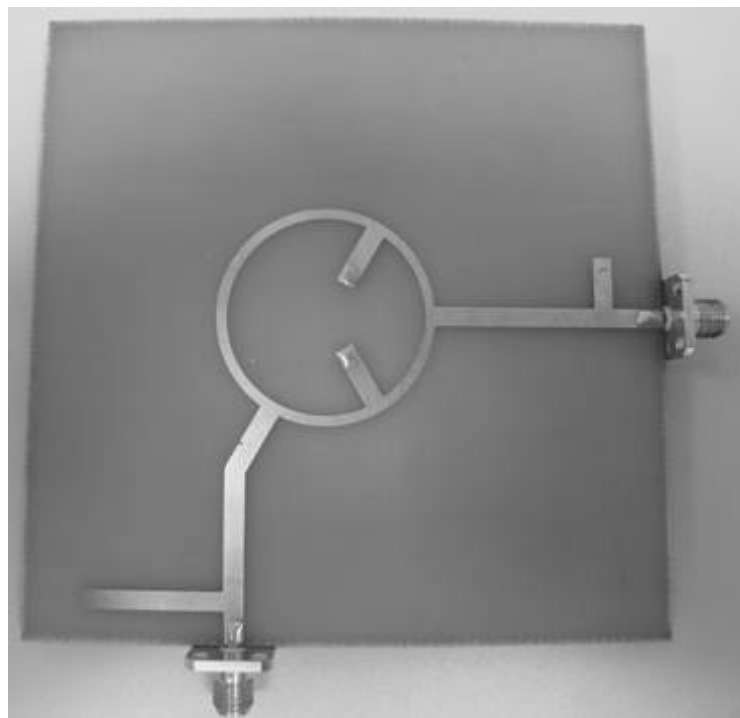


Figure 5.7 Modal feed network implemented as a rat-race hybrid on the lower surface of the substrate

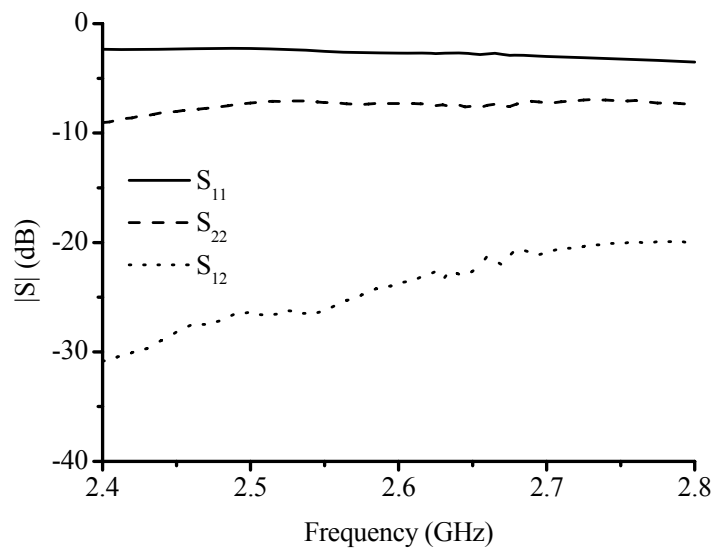


Figure 5.8 Measured S-parameters of the hybrid coupler connected to the 2-element monopole array

Finally, the external ports were matched by introducing stubs at ports 1 and 2 [59], as depicted in Figure 5.7. Theoretically, this should be a straightforward task of calculating stub lengths and positions to match the impedances corresponding to the port reflection coefficients in (5.26). It should however be noted that the currents induced on the array elements for a specific mode are strictly not a direct superposition of the currents for single element excitation. \mathbf{S}^a is therefore not entirely independent of the element excitation. As in Figure 5.9, the measurement shows that the two ports of the decoupled array are matched at different and shifted frequencies, although they were both theoretically matched at around 2.6 GHz. Some tuning was thus required to obtain the measured results shown in Figure 5.10. Decoupling and matching are achieved simultaneously, albeit over a narrow band.

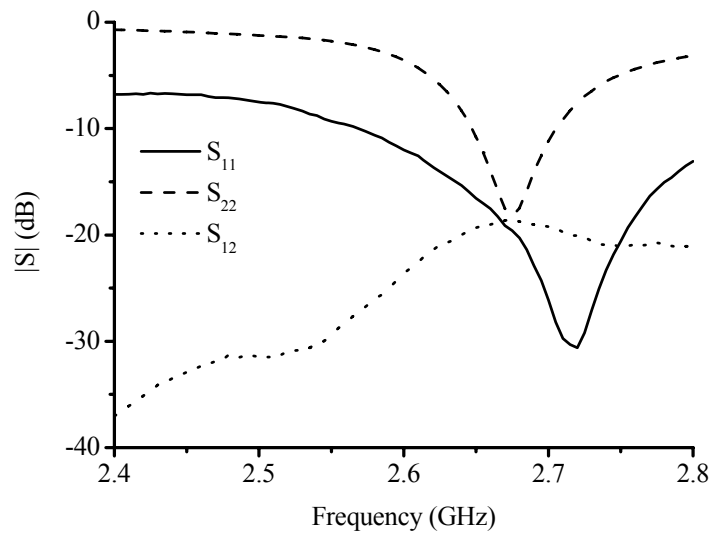


Figure 5.9 Measured S-parameters of the 2-element monopole array with matching networks at the external ports of the modal feed network without tuning

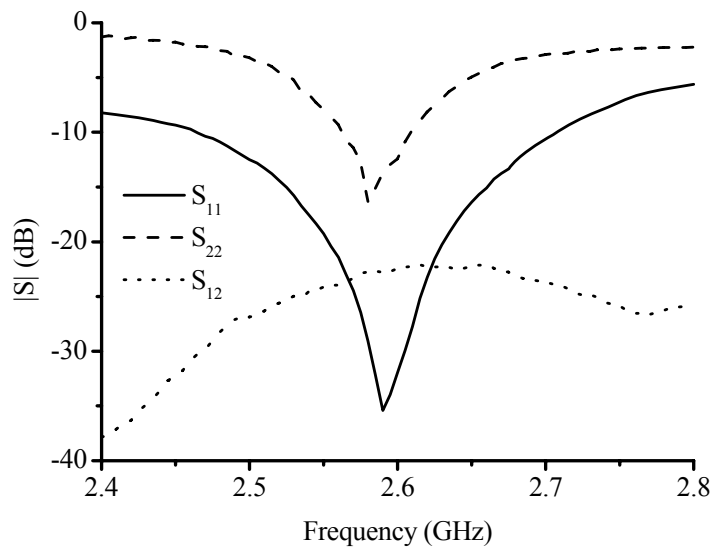


Figure 5.10 Measured scattering parameters of the 2-element monopole array with tuned matching networks at the external ports of the modal feed network

Measured and simulated modal radiation patterns of this array at 2.6 GHz are shown

in Figure 5.11 and Figure 5.12. The measurements were performed in an anechoic chamber. The measurement setup consisted of an Agilent N5230A network analyzer and AL-4806-3C multi-axis position controller from ORBIT/FR Engineering to rotate the antenna. Calibration was performed using two horn antennas from Q-Par Angus Ltd. The array was fed at one of the two input ports of the modal feed network while the other input port was terminated in matched load. This termination absorbed any cross-coupled power at the other port, thus preventing the excitation of more than one eigenmode. Pattern measurements were performed while rotating the antenna through 360 degrees. The simulations were performed using the commercial software package IE3D [52]. The simulation model included the effect of the feed network, but an infinite ground plane was assumed for pattern calculations.

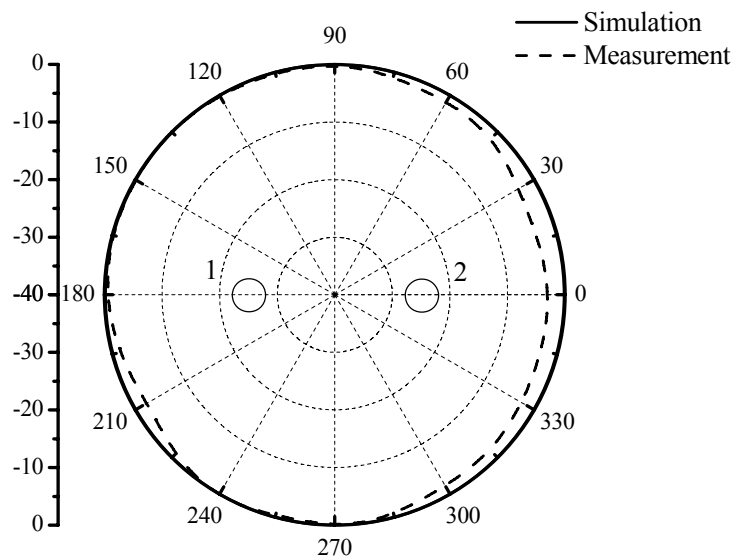


Figure 5.11 Simulated and measured radiation patterns for mode 1 of the 2-element monopole array

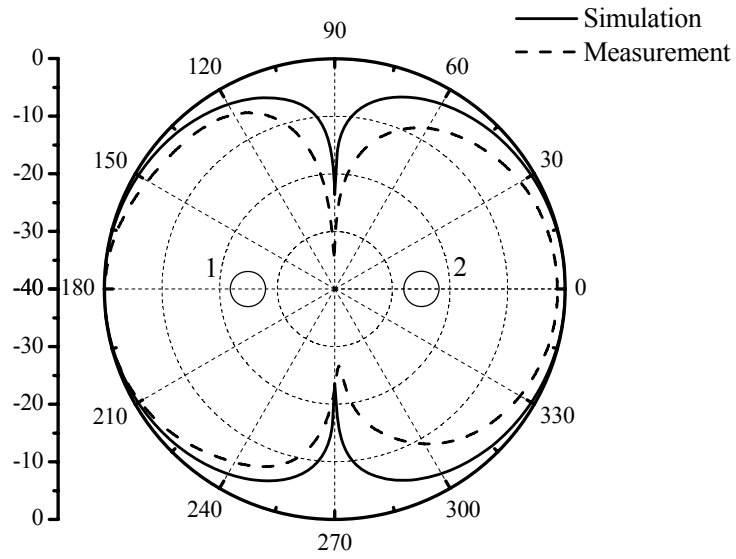


Figure 5.12 Simulated and measured radiation patterns for mode 2 of the 2-element monopole array

5.4.2 Modal feed network for 2×2 element monopole array

A symmetrical 2×2 array has the following S-parameters:

$$\mathbf{S}^a = \begin{bmatrix} S_{11}^a & S_{12}^a & S_{13}^a & S_{14}^a \\ S_{12}^a & S_{11}^a & S_{14}^a & S_{13}^a \\ S_{13}^a & S_{14}^a & S_{11}^a & S_{12}^a \\ S_{14}^a & S_{13}^a & S_{12}^a & S_{11}^a \end{bmatrix}. \quad (5.27)$$

The eigenvalues of \mathbf{S}^a are given by

$$\begin{aligned} \lambda_1 &= S_{11}^a + S_{12}^a + S_{13}^a + S_{14}^a, \\ \lambda_2 &= S_{11}^a + S_{12}^a - S_{13}^a - S_{14}^a, \\ \lambda_3 &= S_{11}^a - S_{12}^a - S_{13}^a + S_{14}^a, \\ \lambda_4 &= S_{11}^a - S_{12}^a + S_{13}^a - S_{14}^a, \end{aligned} \quad (5.28)$$

while the orthonormal eigenvectors are

$$\mathbf{e}_1 = \frac{1}{2} \begin{bmatrix} 1 \\ 1 \\ 1 \\ 1 \end{bmatrix}, \mathbf{e}_2 = \frac{1}{2} \begin{bmatrix} 1 \\ 1 \\ -1 \\ -1 \end{bmatrix}, \mathbf{e}_3 = \frac{1}{2} \begin{bmatrix} 1 \\ -1 \\ -1 \\ 1 \end{bmatrix}, \mathbf{e}_4 = \frac{1}{2} \begin{bmatrix} 1 \\ -1 \\ 1 \\ -1 \end{bmatrix}. \quad (5.29)$$

An 8-port modal feed network can be implemented by using 90° hybrid couplers, as shown in Figure 5.13. The scattering parameters of this network are defined by

$$\mathbf{S}_{ee} = \mathbf{S}_{ii} = \mathbf{0},$$

$$\mathbf{S}_{ie} = \mathbf{S}_{ei}^T = \frac{1}{2} \begin{bmatrix} e^{-j\theta} & e^{j(\pi/2-\theta)} & e^{j(\pi-\theta)} & e^{j(\pi/2-\theta)} \\ e^{-j\theta} & e^{j(\pi/2-\theta)} & e^{-j\theta} & e^{j(-\pi/2-\theta)} \\ e^{-j\theta} & e^{j(-\pi/2-\theta)} & e^{-j\theta} & e^{j(\pi/2-\theta)} \\ e^{-j\theta} & e^{j(-\pi/2-\theta)} & e^{j(\pi-\theta)} & e^{j(-\pi/2-\theta)} \end{bmatrix}. \quad (5.30)$$

The phase terms in (5.17) are therefore

$$\begin{aligned} \phi_1 &= -\theta, \\ \phi_2 &= \phi_4 = \pi/2 - \theta, \\ \phi_3 &= \pi - \theta. \end{aligned} \quad (5.31)$$

The S-parameters of a combination of this feed network and the 2×2 array are obtained from (5.19) as

$$\begin{aligned} \mathbf{S}^c &= \text{diag} \left[(S_{11}^a + S_{12}^a + S_{13}^a + S_{14}^a) e^{-j2\theta}, \right. \\ &\quad (-S_{11}^a - S_{12}^a + S_{13}^a + S_{14}^a) e^{-j2\theta}, \\ &\quad (S_{11}^a - S_{12}^a - S_{13}^a + S_{14}^a) e^{-j2\theta}, \\ &\quad \left. (-S_{11}^a + S_{12}^a - S_{13}^a + S_{14}^a) e^{-j2\theta} \right]. \end{aligned} \quad (5.32)$$

The external ports of the feed network can again be matched with the addition of conventional matching circuits.

The 2×2 monopole array shown in Figure 5.14 was fabricated. The dimensions of antenna element are shown in Figure 5.3. The inter-element spacing was arbitrarily chosen as 20 mm (approximately 0.17λ). The measured scattering parameters of the array are shown in Figure 5.15. Strong mutual coupling is observed.

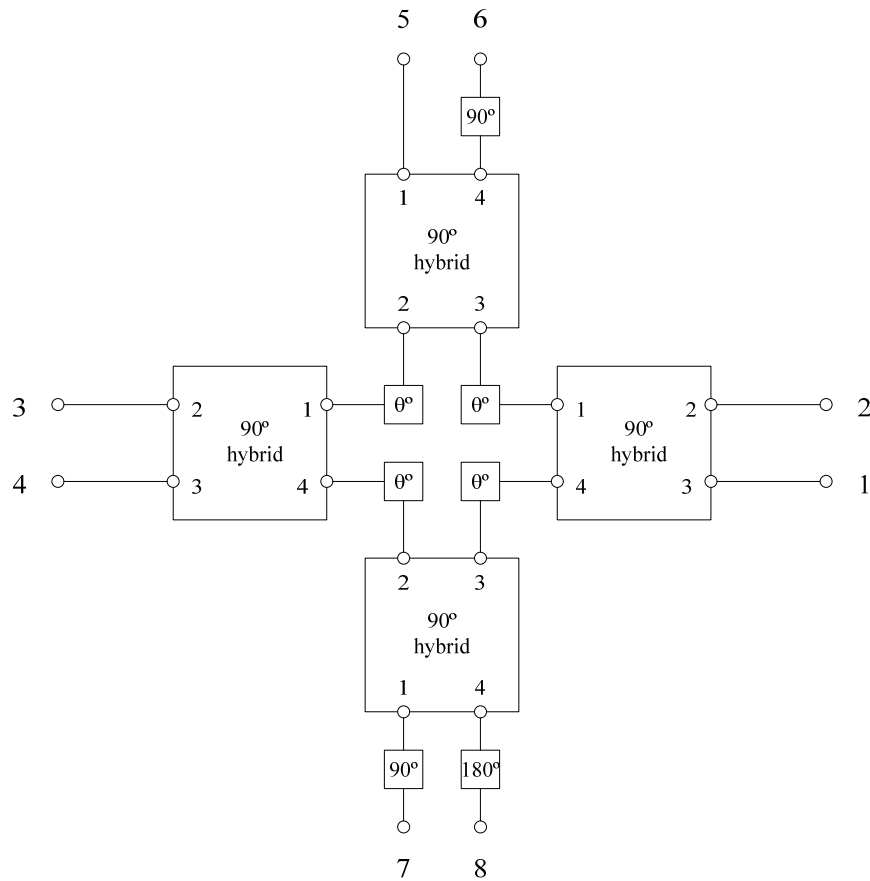


Figure 5.13 8-port modal feed network for the 2×2 element array

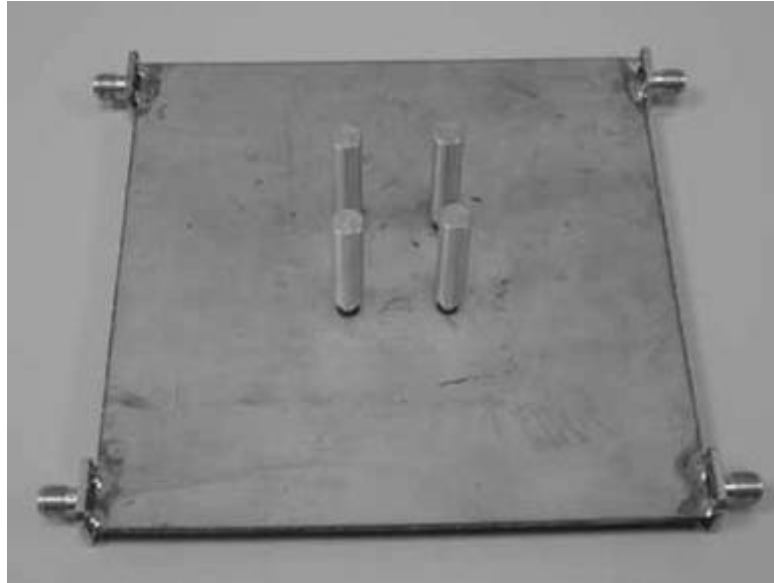


Figure 5.14 2×2 element monopole array with inter-element spacing of 20 mm

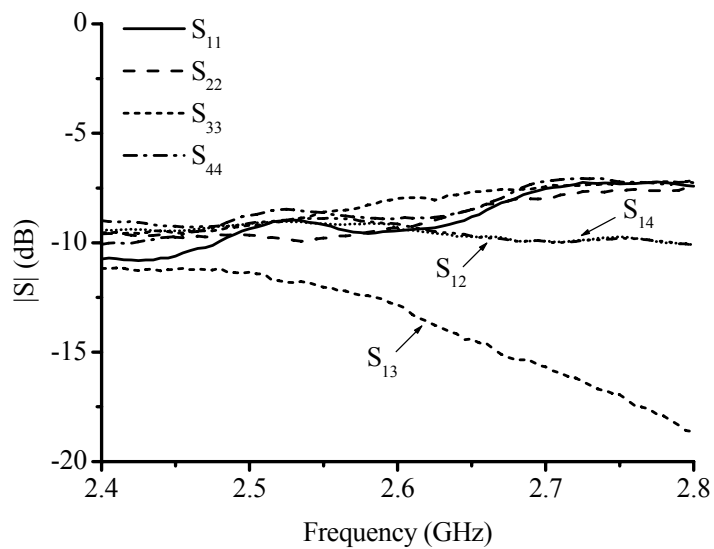


Figure 5.15 Measured scattering parameters of the 2×2 array.

The modal feed network shown in Figure 5.16 (without the matching stubs) was realized using $-3\text{dB } 90^\circ$ branchline couplers. It was implemented on the lower surface of the substrate and connected to the array. The measured S-parameters are shown in Figure 5.17. The ports are not matched, but the introduction of the modal feed

network has the effect of decoupling the ports.

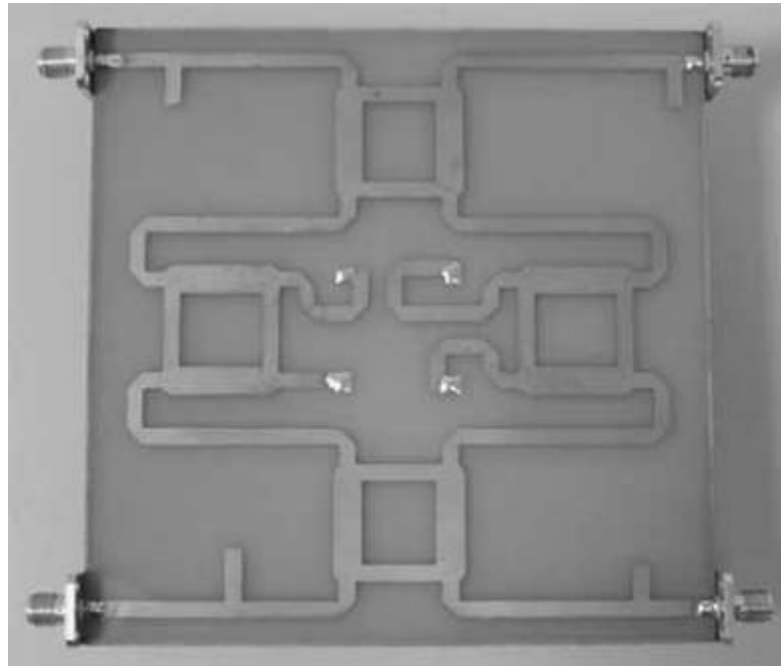


Figure 5.16 8-port modal feed network consisting of four -3 dB 90° branchline couplers

With the addition of stub matching networks at ports 1 to 4, decoupling and matching are achieved simultaneously. The measured S-parameters are shown in Figure 5.18. Some tuning was again required in order to achieve resonance at a fixed frequency for each of the four eigenmodes.

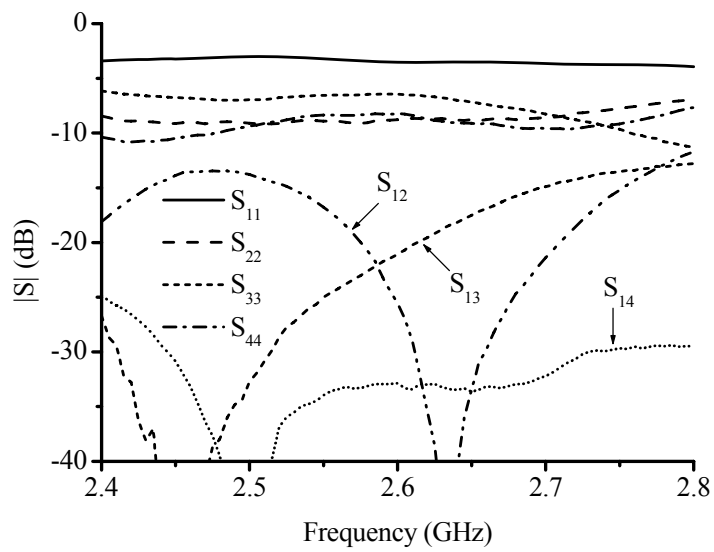


Figure 5.17 Measured scattering parameters of the modal feed network connected to the 2×2 array

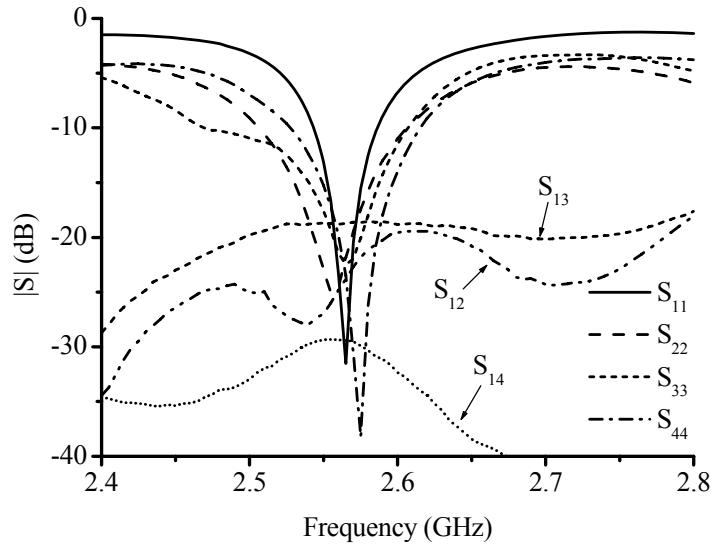


Figure 5.18 Measured scattering parameters of the 2×2 array with matched external ports of the modal feed network

The radiation patterns of the four modes were computed using IE3D [52], and the

results are shown in Figures 5.19 and 5.20. The modal feed network in Figure 5.16 was included in the simulation model for the calculation of the currents on the antenna elements and the respective radiation patterns. The eigenpatterns are mutually orthogonal according to the definition provided in [24]. An arbitrary pattern within the 4-dimensional space of radiation patterns available from the original array can be obtained from a weighted linear combination of the modal patterns [24].

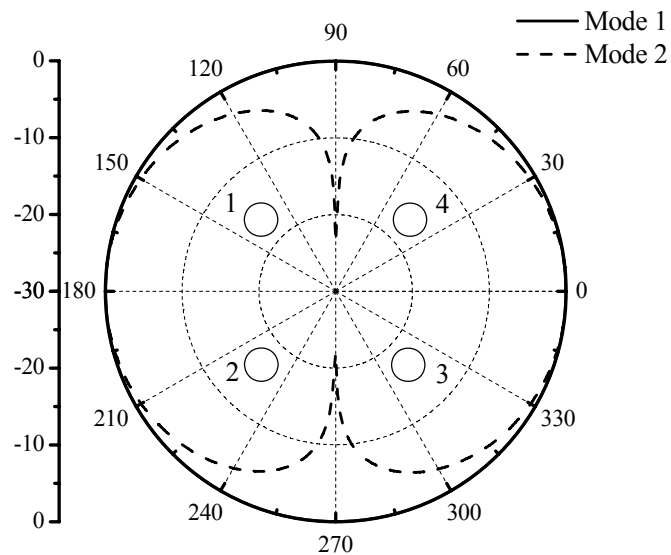


Figure 5.19 Simulated radiation patterns (normalized) of the 2×2 array for eigenmodes 1 and 2

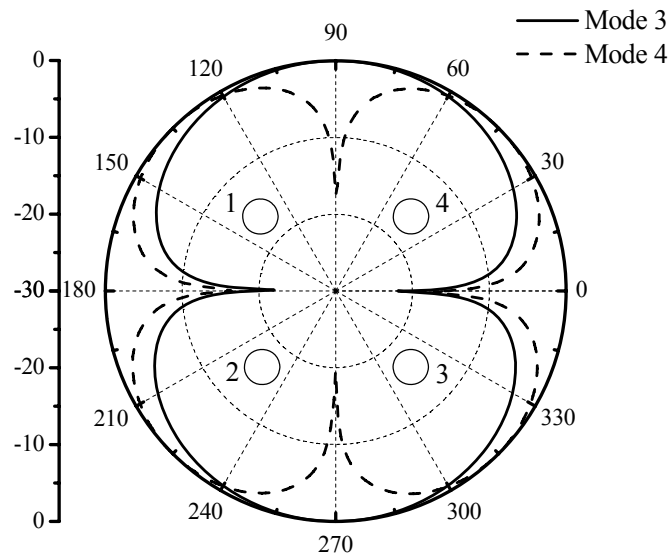


Figure 5.20 Simulated radiation patterns (normalized) of the 2×2 array for eigenmodes 3 and 4

As seen from the above examples, the modal feed network ensures isolation between the input ports of the system, which can then be matched independently. The frequency bandwidth of such a system is limited by the level of mutual coupling in the original array [23], but also depends on the extent of the impedance mismatch observed at the external ports of the modal feed network. In order to minimize the mismatch, it is desirable to start off with an array with matched elements, i.e. $|S_{11}^a|$ should be as small as possible. Theoretically, the alternative approach to port decoupling and matching presented in this chapter is applicable to arrays with an arbitrary number of uniformly-spaced, identical elements. However, the complexity involved in the implementation of the modal feed network may limit application of this method to smaller arrays.

5.4.3 Compact modal feed network for 2×2 element monopole array

The modal feed network described in previous sections successfully isolates the input ports of a symmetrical array by exploiting the inherent orthogonality of the eigenmodes of the array. For a symmetrical 2×2 array, the required modal feed network basically consists of an 8-port comparator and impedance matching circuits. In the example of Section 5.4.2, the modal feed network was realized using four -3dB 90° branchline couplers. While this circuit produced the desired response, it was again substantial in size compared to the area required for the array. It would therefore be desirable to be able to reduce the size of the feed network while retaining the attractive properties of such an antenna system.

In this section, a novel 2×2 monopole array is described. The feed network is implemented as a planar ring-type 8-port comparator with four broadside coupled line sections [60]. Compared to other 8-port hybrids based on interconnected branch guide 90° hybrids and transmission lines [61, 62], the compact coupled line hybrid ring circuit has a circumference of only 1 wavelength and thus is a good choice for the feed network. This results in a significant reduction in size. The dimensions of the adaptive array are determined by the radiating elements and element spacing, since the feed network no longer imposes a lower limit on the overall size.

As shown in Figure 5.21, the ring circuit has four quarter-wavelength-long coupled line hybrids. The coupled transmission lines are etched on the top (solid lines) and bottom (dotted lines) surfaces of a thin dielectric board. It is based on the use of four 90° hybrids connected together in a symmetrical arrangement to produce an 8-port

circuit. As a result, at a given frequency, the 8-port hybrid has the same size as a 2-branch 90° hybrid, which can significantly reduce the size of the feed network.

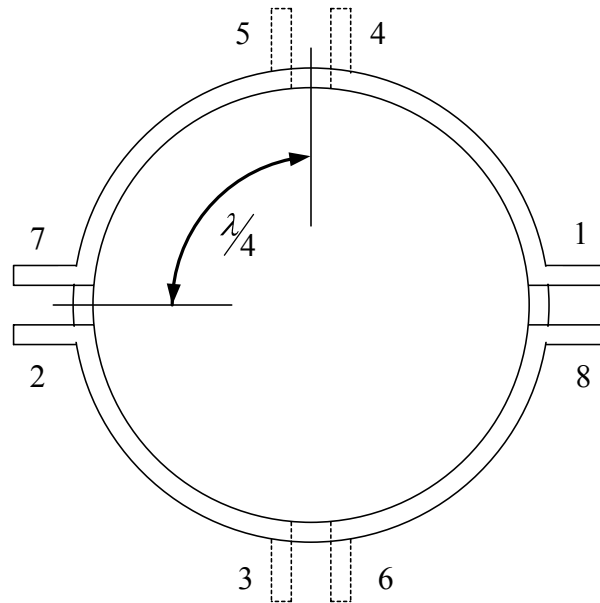


Figure 5.21 Schematic diagram of an 8-port hybrid ring circuit based on four coupled line 90° hybrids

At an appropriate reference plane, it can be shown that the coupled ring circuit has S-parameters of

$$\mathbf{S} = \frac{1}{2} \begin{bmatrix} 0 & 0 & 0 & 0 & 1 & 1 & j & -j \\ 0 & 0 & 0 & 0 & 1 & 1 & -j & j \\ 0 & 0 & 0 & 0 & j & -j & 1 & 1 \\ 0 & 0 & 0 & 0 & -j & j & 1 & 1 \\ 1 & 1 & j & -j & 0 & 0 & 0 & 0 \\ 1 & 1 & -j & j & 0 & 0 & 0 & 0 \\ j & -j & 1 & 1 & 0 & 0 & 0 & 0 \\ -j & j & 1 & 1 & 0 & 0 & 0 & 0 \end{bmatrix}. \quad (5.33)$$

As seen from the above S matrix, all ports are matched and the sets of 4 input and 4 output ports are isolated and power from any input port is equally divided to the output ports.

If -90° phase shifter is added to ports 3 and 7 and 90° phase shifter is added to ports 4 and 8, the S matrix becomes

$$\mathbf{S} = \frac{1}{2} \begin{bmatrix} 0 & 0 & 0 & 0 & 1 & 1 & 1 & 1 \\ 0 & 0 & 0 & 0 & 1 & 1 & -1 & -1 \\ 0 & 0 & 0 & 0 & 1 & -1 & -1 & 1 \\ 0 & 0 & 0 & 0 & 1 & -1 & 1 & -1 \\ 1 & 1 & 1 & 1 & 0 & 0 & 0 & 0 \\ 1 & 1 & -1 & -1 & 0 & 0 & 0 & 0 \\ 1 & -1 & -1 & 1 & 0 & 0 & 0 & 0 \\ 1 & -1 & 1 & -1 & 0 & 0 & 0 & 0 \end{bmatrix}. \quad (5.34)$$

This is the S matrix of the standard sum and difference comparator. From Equation (5.6) – (5.8), we know it is exactly the S matrix of an ideal feed network for an array of 4.

Figure 5.22 shows the structure of the 4-element array with ring coupled lines as decoupling network. The top surface of the first layer and the bottom surface of the third layer are ground planes and the ring coupled lines are etched on the two sides of the mid layer. The substrate was chosen as RT/Duroid 5880 ($\epsilon_r = 2.2$) of thickness 20 mil for the top and bottom layers and 5 mil for center layer. The ideal even and odd mode impedances for the coupled line hybrids are $Z_{0e} = 120.71 \Omega$ and $Z_{0o} = 20.71 \Omega$. At the selected center frequency of 2.6 GHz, it was calculated that the chosen line width of 0.508 mm would yield impedances of approximately $Z_{0e} = 114 \Omega$ and $Z_{0o} = 22 \Omega$, which were deemed to be acceptable. The inner radius of the ring is then 13.51 mm and the outer radius is 14.02 mm. The additional phase shifters mentioned above that are required at some of the ports to produce the proper comparator response were implemented as simple line sections. The inter-element

spacing for the monopoles is 15 mm ($\approx 0.13\lambda$). Each monopole consists of a copper wire which is 1 mm in diameter and 29 mm in length. The array elements are placed inside the ring. They protrude through Teflon-filled holes in the upper ground plane of the stripline structure and are connected to the internal ports of the feed network. The photographs of the prototype array with decoupling network are shown in Figures 5.23 - 5.25.

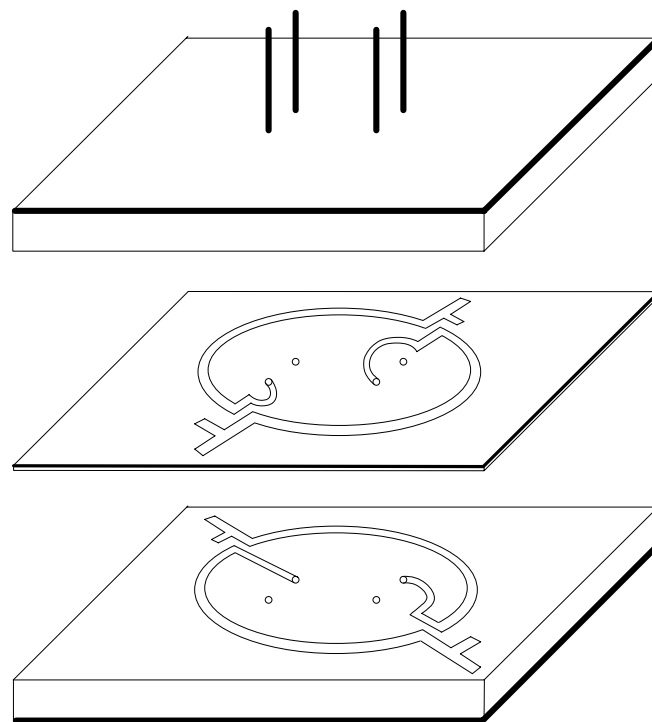


Figure 5.22 2×2 element monopole array with compact ring-type comparator circuit as modal feed network

The scattering parameters of the original array were measured using an Agilent Technologies 8510C Network Analyzer. The results are shown in Figure 5.26. Mutual coupling of approximately -10 dB at 2.6 GHz is observed.



Figure 5.23 Prototype 2×2 element monopole array with decoupled ports

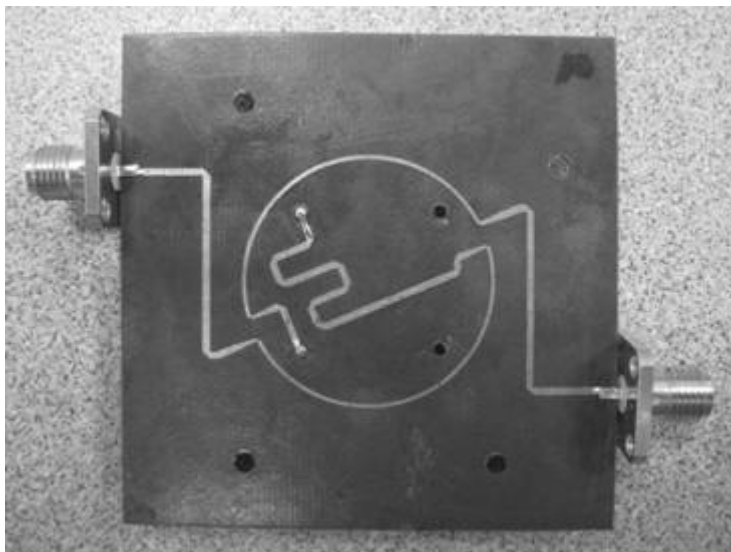


Figure 5.24 Ring etched on the bottom surface of first layer

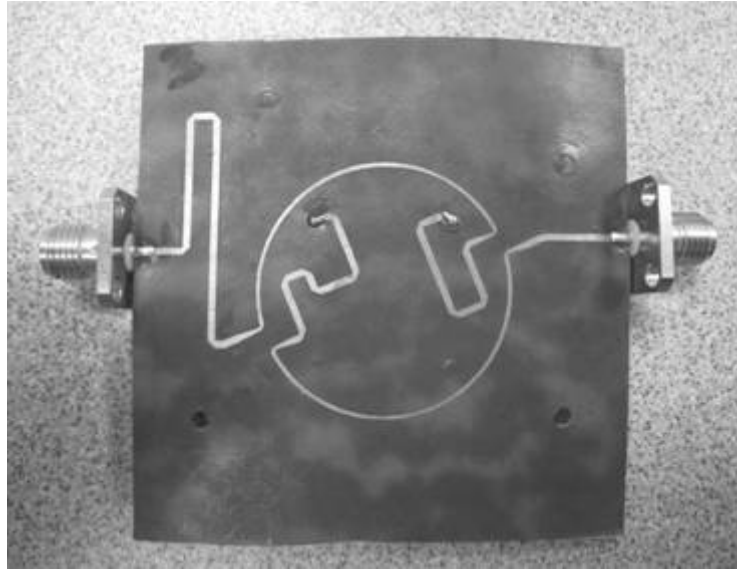


Figure 5.25 Ring etched on the bottom surface of second layer

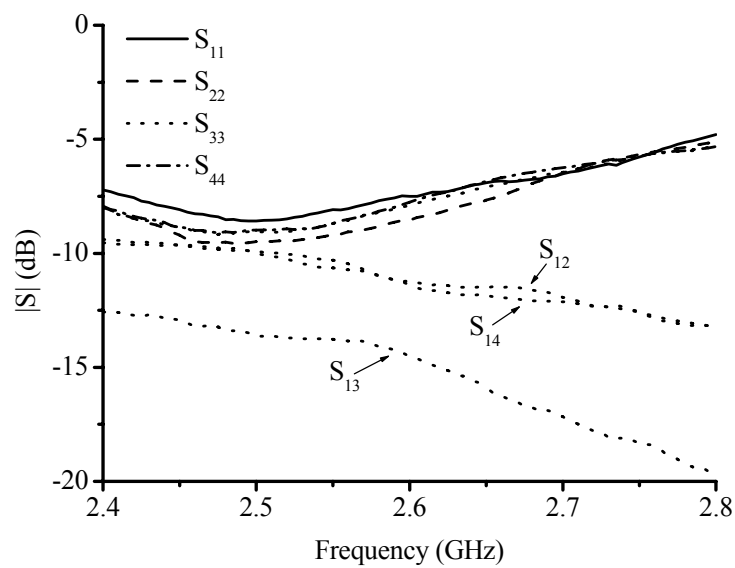


Figure 5.26 Measured S-parameters of the original 2×2 monopole array

The measured S-parameter of the array with ring feed network (without the matching network) is shown in Figure 5.27. It can be seen that all the ports have been isolated with the mutual coupling being around -20 dB across the frequency band. However, in accordance with Equation (5.9), the ports are not matched. With the addition of

stub matching networks at ports 1 to 4, decoupling and matching are achieved simultaneously. The measured S-parameters are shown in Figure 5.28. Some tuning was again required in order to achieve resonance at a fixed frequency for each of the four eigenmodes.

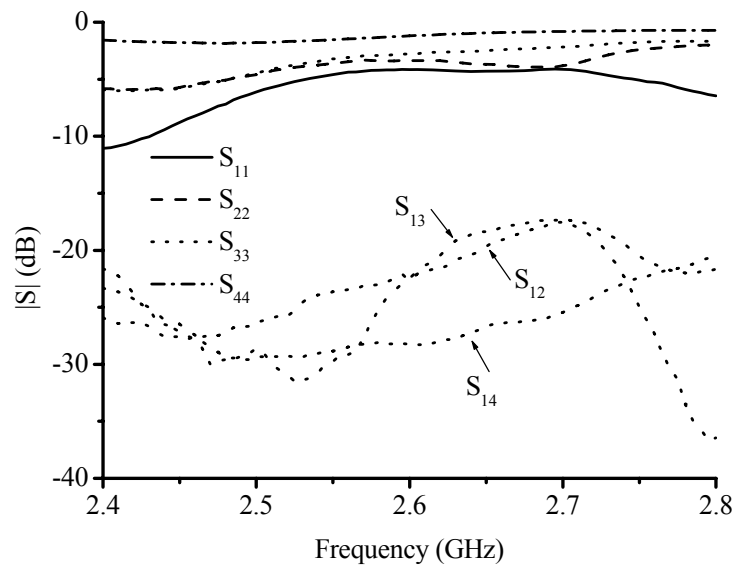


Figure 5.27 Measured S-parameters of the modal feed network connected to the 2×2 array

Measured and simulated modal radiation patterns at 2.6 GHz are shown in Figures 5.29 – 5.32. The measurements were performed in the same way as described in Section 5.4.1. The simulations were performed using the commercial software package IE3D [52]. The simulation model assumed an ideal feed network and an infinite ground plane was assumed for pattern calculations.

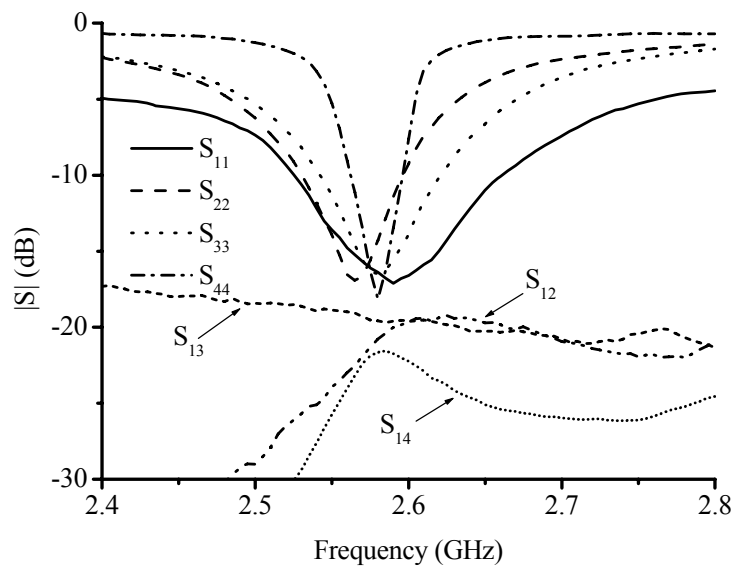


Figure 5.28 Measured S-parameters of the 2×2 array with matched external ports of the modal feed network.

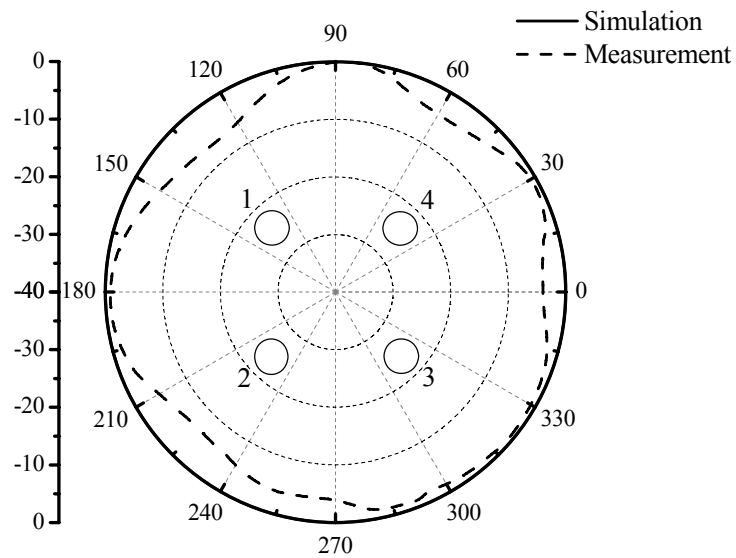


Figure 5.29 Radiation pattern (normalized) of the 2×2 array for eigenmode 1.

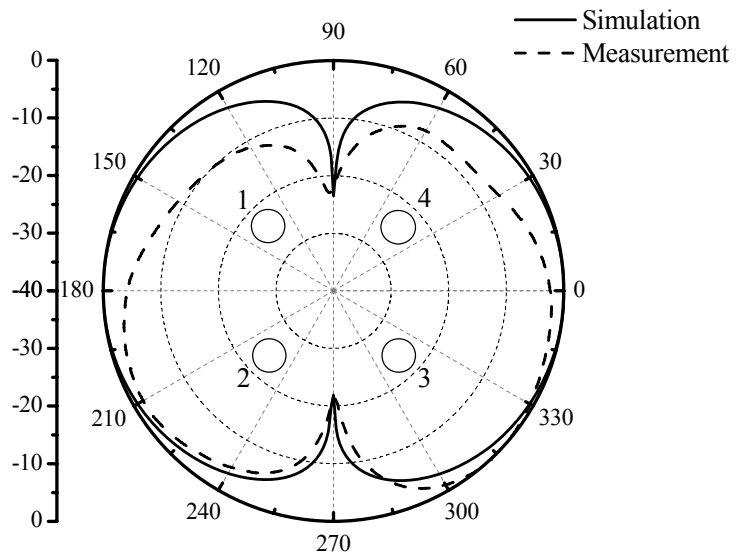


Figure 5.30 Radiation pattern (normalized) of the 2×2 array for eigenmode 2.

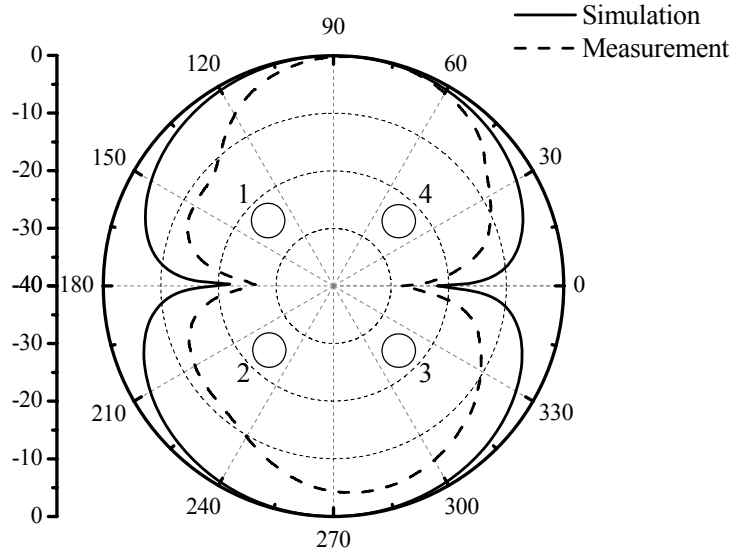


Figure 5.31 Radiation pattern (normalized) of the 2×2 array for eigenmode 3.

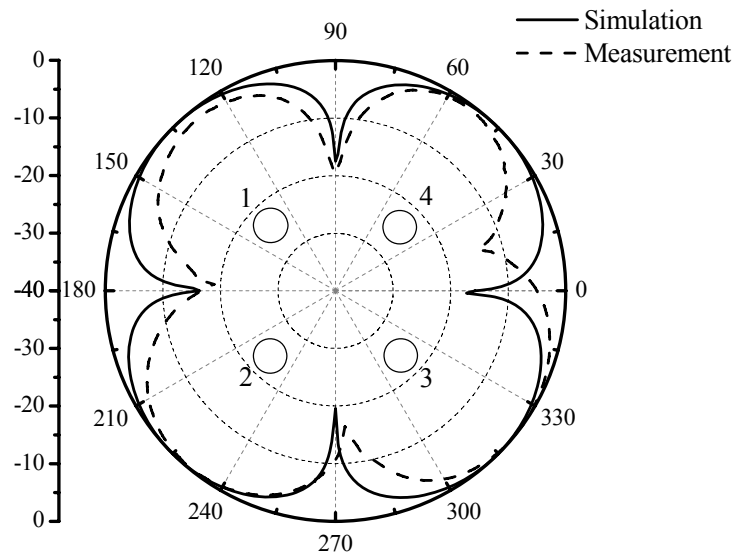


Figure 5.32 Radiation pattern (normalized) of the 2×2 array for eigenmode 4.

Large discrepancies were found between the above simulated and measured radiation patterns of the 2×2 array. It was analyzed that the discrepancies might be due to several aspects. Firstly, the simulation model used direct excitation of the eigenmodes and therefore did not include effects of discrepancies in the feed network response. The modal feed network was analysed to obtain a more accurate estimation of its response. The respective output voltages for each mode were then used to excite the array elements during the pattern simulations. Secondly, infinite ground plane was assumed in IE3D simulation, which is not the case in practical. Therefore, to get more accurate results, the simulations were then performed using the commercial software package HFSS [63]. This finite element based code was chosen due to its ability to model the asymmetric, finite ground plane.

In addition, it was noted that for the prototype shown in Figure 5.23, connection between the upper and lower ground planes was provided by four metal screws which

clamped the substrate layers between the ground planes. This resulted in improper grounding at the feed points. Thus, the upper ground plane was redesigned to include L-shaped metal tabs to which the connectors were secured, as illustrated in Figure 5.33. This ensured the proper excitation of stripline mode at the feed points and also improved the integrity of the measured radiation patterns. With above analysis and improvements, good agreement between the simulated and measured results was obtained. The updated results are shown in Figures 5.34 – 5.38.

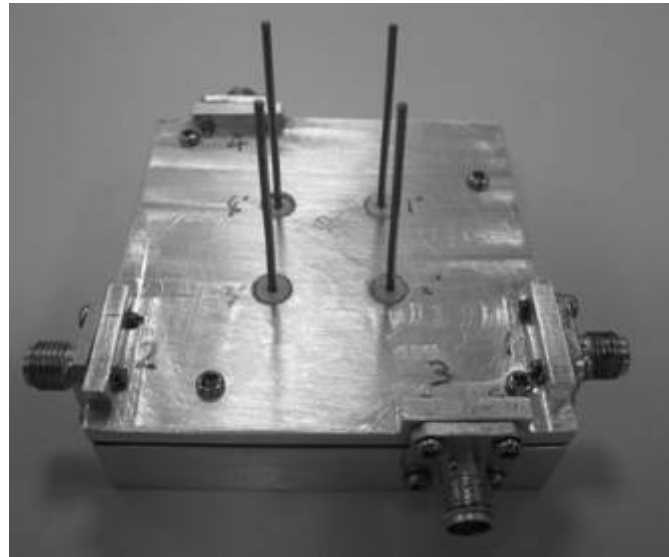


Figure 5.33 Redesigned prototype of 2×2 monopole array with decoupled ports

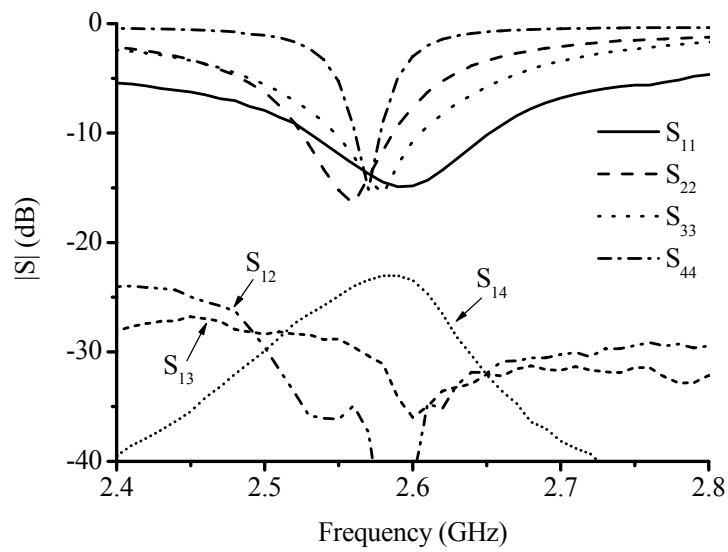


Figure 5.34 Measured S-parameters of the redesigned prototype array.

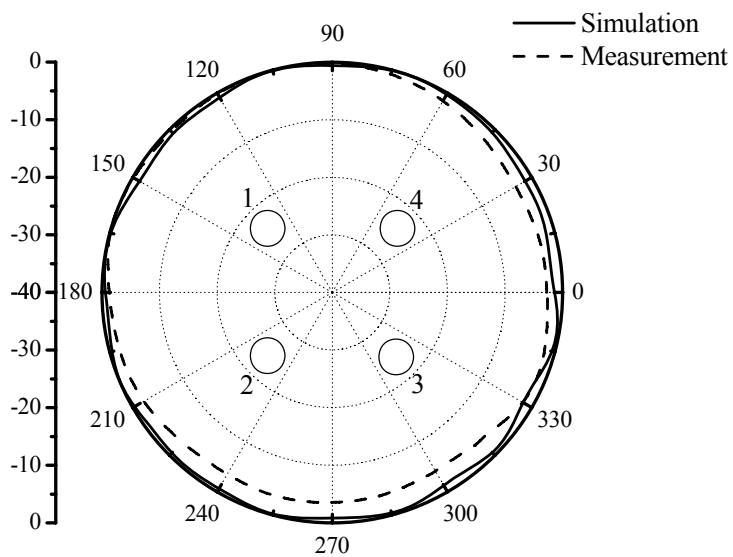


Figure 5.35 Radiation pattern (normalized) of the redesigned prototype 2×2 array for eigenmode 1.

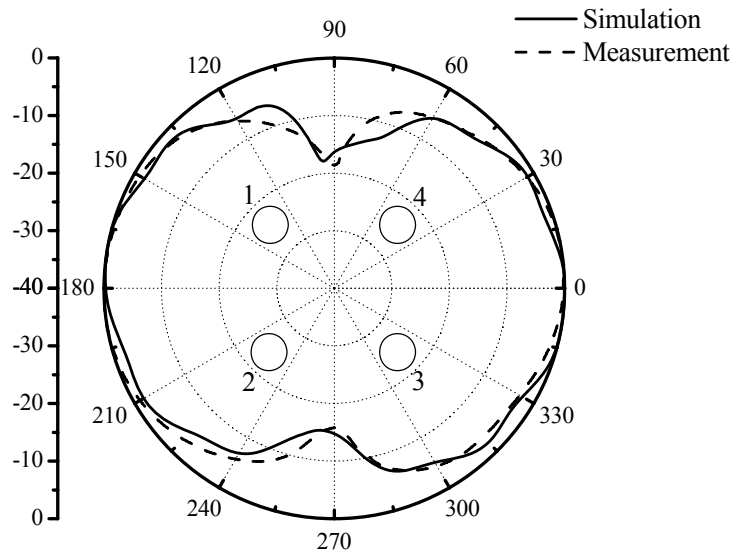


Figure 5.36 Radiation pattern (normalized) of the redesigned prototype 2×2 array for eigenmode 2.

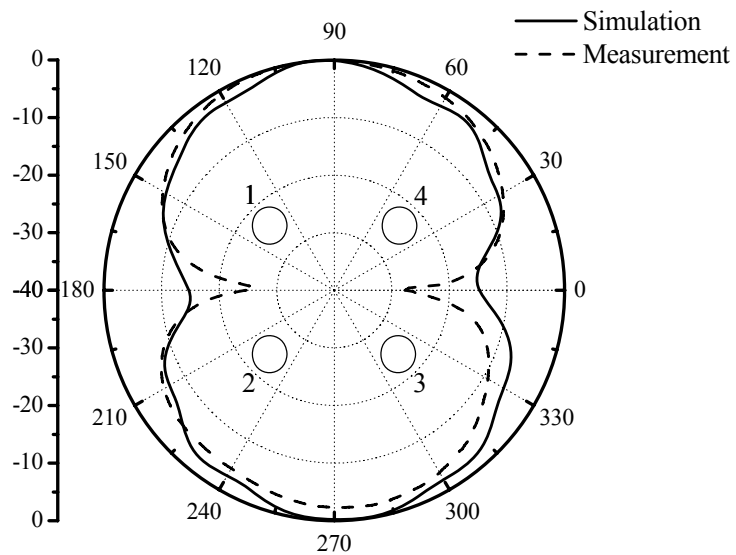


Figure 5.37 Radiation pattern (normalized) of the redesigned prototype 2×2 array for eigenmode 3.

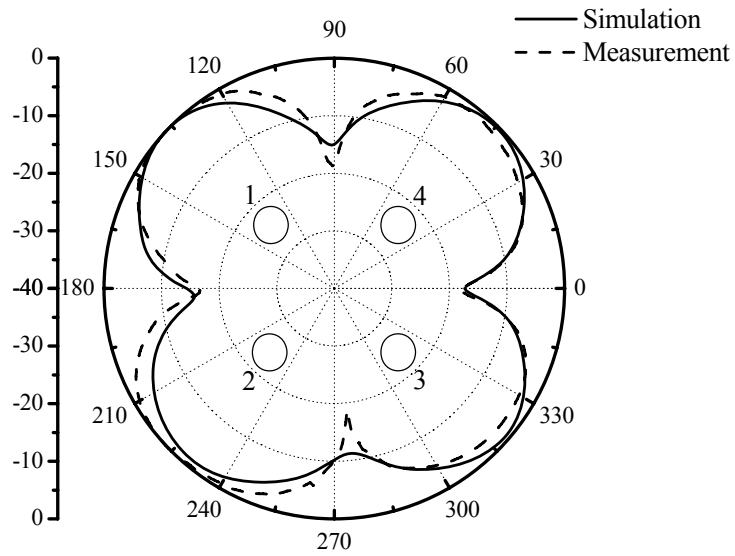


Figure 5.38 Radiation pattern (normalized) of the redesigned prototype 2×2 array for eigenmode 4.

Again from a weighted linear combination of the modal patterns, it is possible to construct an arbitrary pattern within the 4-dimensional space of radiation patterns available from the original array. With the modal feed network introduced in this paper, the decoupling circuit no longer determines the overall size of the array. This makes it suitable for future application in mobile devices. The fact that the diameter of the feed network is only 0.32λ also opens up the possibility of using this compact array as an adaptive element in a larger array with conventional $\lambda/2$ inter-element spacing, i.e. an array of arrays.

Chapter 6 Conclusions

Multiport antenna arrays are widely used in space-time techniques like diversity reception, adaptive beamforming or nulling and direction finding. A multiport array with isolated ports has the ability to provide duplexing functions. As a result, multiport antennas usually have the design goal of isolated ports and uncorrelated radiation patterns. For antenna diversity on size-limited platforms (e.g. in mobile applications), restrictions on the available space demand the use of an element spacing significantly smaller than $\lambda/2$. The small element spacing introduces strong mutual coupling between the ports of such compact arrays. Due to the coupling, the input impedance of the array changes when element excitations are varied. Consequently, the array cannot be matched for an arbitrary excitation. The strong coupling can cause significant system performance degradation. A decoupling network may compensate for the mutual coupling effects to yield decoupled ports and a fixed input impedance.

For an n -port array, the decoupling network is a $2n$ -port network with n ports connected to the array elements, while the remaining n ports represent the isolated input ports. It generally consists of a symmetrical network of interconnected reactive elements and/or transmission line sections and stubs. Various implementations of decoupling networks have been described in the literature. In its simplest form, the decoupling network consists of reactive elements connected between neighboring array elements, which effectively cancel the external mutual coupling between them. However, this technique is only applicable in special cases where the off-diagonal elements of the admittance matrix of the original array are all purely imaginary.

As related work to this thesis, reviews on characteristics of dense array and modal model were presented in Chapter 3. Decoupling network design using eigenmode analysis for 3-element and 4-element arrays with arbitrary complex mutual admittances were also described. The values of lossless components in the circuit were obtained by solving a number of complicated equations. The decoupling network design becomes increasingly more complicated as the number of array elements grows. However, for maximum versatility, the number of elements in an adaptive array needs to be as large as possible. The design of decoupling networks for larger arrays with 4 or more elements was explored in Chapter 4. This new systematic design approach involves the step-by-step decoupling of the characteristic eigenmodes of the array. The procedure would theoretically be applicable to arrays of various sizes. However, implementation of the decoupling network for the examples of 6-element and 8-element array would require the use of multilayer circuits, which is not surprising for arrays with large number of elements.

The decoupling networks proposed previously contain only lossless components such as inductors or capacitors. In practical implementation, the lossless reactive components are usually converted to microstrip lines or striplines. These networks are sometimes much larger in size than the array itself, which makes the concept less suitable for applications where the available space for the antennas is limited. Therefore, novel alternative approach to realize port decoupling was presented in Chapter 5. Antenna elements are fed via a modal feed network where isolation between the new input ports is achieved by exploiting the inherent orthogonality of the eigenmodes of the array. The input ports can then be matched independently. For

beam forming, the required element weights are obtained as a linear combination of the orthogonal eigenvectors. This new approach is easy to understand and provides a simple design procedure of decoupling. For a symmetrical 2×2 array, the required modal feed network basically consists of an 8-port comparator and impedance matching circuits. In the first design example, the modal feed network was realized using four -3dB 90° branchline couplers. While this circuit produced the desired response, it was again substantial in size compared to the area required for the array. It would therefore be desirable to be able to reduce the size of the feed network while retaining the attractive properties of such an antenna system. The planar ring-type 8-port comparator with four broadside coupled line sections has a circumference of only 1 wavelength and thus is a good choice for the feed network. This results in a significant reduction in size. The dimensions of the adaptive array are determined by the radiating elements and element spacing, since the feed network no longer imposes a lower limit on the overall size. This makes it suitable for future application in mobile devices.

In conclusion, this thesis has deeply investigated different decoupling techniques and successfully developed novel decoupling network design concepts.

REFERENCE

- [1] A. Paulraj and C. B. Papadias, "Space-time processing for wireless communications", *IEEE Signal Processing Magazine*, vol. 14, no. 6, pp.49-83, Nov 1997.
- [2] G. J. Foschini and M. J. Gans, "On limits of wireless communications in a fading environment when using multiple antennas", *Wireless Personal Communications*, vol. 6, no. 3, pp. 311-335, Mar 1998.
- [3] J. H. Winters, J. Salz and R. D. Gitlin, "The impact of antenna diversity on the capacity of wirelesscommunication systems", *IEEE Trans. Communications*, vol. 42, no. 234, pp. 1740-1751, Feb/ Mar/ Apr 1994.
- [4] I. J. Gupta and A. A. Ksienski, "Effect of mutual coupling on the performance of adaptive arrays", *IEEE Trans. Antennas and Propagation*, vol. 31, no. 5, pp. 785-791, Sep 1983.
- [5] I. J. Gupta and A. A. Ksienski, "Dependence of adaptive array performance on conventional array design", *IEEE Trans. Antennas and Propagation*, vol. 30, no. 4, pp. 549-553, Jul 1982.
- [6] I. J. Gupta and A. A. Ksienski, "Prediction of adaptive array performance", *IEEE Trans. Aerospace and Electronic Systems*, vol. 19, no. 3, pp. 380-388, May 1983.
- [7] H. E. King, "Mutual impendence of unequal length antennas in echelon", *IRE Trans. Antennas and Propagation*, vol. 5, no. 3, pp. 306-313, Jul 1957.
- [8] C. A. Balanis, *Antenna Theory: Analysis and Design*, 2nd ed., Wiley, 1997.
- [9] V. Jungnickel, V. Pohl and C. von Helmolt, "Capacity of MIMO systems with closely spaced antennas", *IEEE Communications Letters*, vol. 7, no. 8, pp. 361-363, Aug 2003.

- [10] H. J. Chaloupka and X. Wang, "Novel approach for diversity and MIMO antennas at small mobile platforms", in *Proc. IEEE Int. Symp. on Personal, Indoor and Mobile Radio Communications*, vol. 1, pp. 637- 642, Sep 2004.
- [11] A. C. Ludwig, "Mutual coupling, gain and directivity of an array of two identical antennas", *IEEE Trans. Antennas and Propagation*, vol. 24, no. 6, pp. 837-841, Nov 1976.
- [12] E. M. Friel and K. M. Pasala, "Effects of mutual coupling on the performance of STAP antenna arrays", *IEEE Trans. Aerospace Electronic Systems*, vol. 36, no. 2, pp. 518-527, Apr 2000.
- [13] W. Lee, "Effect of mutual coupling on a mobile-radio maximum ratio diversity combiner with a large number of branches", *IEEE Trans. Communications*, vol. 20, no. 6, pp. 1188–1193, Dec 1972.
- [14] R. R. Ramirez and F. De Flaviis, "A mutual coupling study of linear polarized microstrip antennas for use in BLAST wireless communications architecture", in *IEEE Antennas and Propagation Society Int. Symp. Dig.*, vol. 2, pp. 490–493, Jul 2000.
- [15] G. V. Tsoulos, "Experimental and theoretical capacity analysis of spacedivision multiple access (SDMA) with adaptive antennas", in *Proc. IEE Communications*, vol. 146, no. 5, pp. 307–311, Oct 1999.
- [16] K. R. Dandekar, H. Ling, and G. Xu, "Effect of mutual coupling on direction finding in smart antenna applications", *Electronics Letters*, vol. 36, no. 22, pp. 1889–1891, Oct 2000.
- [17] A. M. Wyglinski and S. D. Blostein, "Mutual coupling and scattering effects on cellular CDMA systems using smart antennas", *IEEE Vehicular Technology Conference*, vol. 4, pp. 1656–1662, Sep 2000.

- [18]S. R. Rengarajan and A. G. Derneryd, “Application of compound coupling slots in the design of shaped beam antenna patterns”, *IEEE Trans. Antennas and Propagation*, vol. 41, no. 1, pp. 59-65, Jan 1993.
- [19]H. Steyskal and J. S. Herd, “Mutual coupling compensation in small array antennas”, *IEEE Trans. Antennas and Propagation*, vol. 38, no. 12, pp. 1971-1975, Dec 1990.
- [20]P. Darwood, P. N. Fletcher and G. S. Hilton, “Mutual coupling compensation in small planar array antennas”, *IEE Proc. Microwaves, Antennas and Propagation*, vol. 145, no. 1, pp. 1-6, Feb 1998.
- [21]D. Segovia-Vargas, R. Martin-Cuerdo and M. Sierra-Perez, “Mutual coupling effects correction in microstrip arrays for direction-of-arrival (DOA) estimation”, *IEE Proc. Microwaves, Antennas and Propagation*, vol. 149, no. 2, pp. 113-118, Apr 2002.
- [22]H. T. Hui, “Compensating for the mutual coupling effect in direction finding based on a new calculation method for mutual impedance”, *IEEE Antennas and Wireless Propagation Letters*, vol. 2, no. 1, pp. 26-29, Jan 2003.
- [23]H. J. Chaloupka, X. Wang and J. C. Coetzee, “A superdirective 3-element array for adaptive beamforming”, *Microwave and Optical Technology Letters*, vol. 36, no. 6, pp. 425-430, Feb 2003.
- [24]H. J. Chaloupka, X. Wang and J. C. Coetzee, “Performance enhancement of smart antennas with reduced element spacing”, in *Proc. IEEE Conference Wireless Communications and Networking*, vol. 1, pp. 425 – 430, Mar 2003.
- [25] H.J. Chaloupka, X. Wang and J.C. Coetzee, “Compact Arrays for Mobile Platforms: Trade-off Between Size and Performance for SDMA and MIMO Applications”, 48 *Internationales Wissenschaftliches Kolloquium*, Technische

- Universität Ilmenau, Sep. 2003.
- [26] J. Anderson and H. Rasmussen, "Decoupling and descattering networks for antennas", *IEEE Trans. Antennas and Propagation*, vol. 24, no. 6, pp. 841-846, Nov 1976.
- [27] J. Weber, C. Volmer, K. Blau, R. Stephan and M. A. Hein, "Miniaturized antenna arrays using decoupling networks with realistic elements", *IEEE Trans. Microwave Theory and Techniques*, vol. 54, no. 6, pp. 2733-2740, Jun 2006.
- [28] P. T. Chua and J. C. Coetzee, "Microstrip decoupling networks for low-order multi-port arrays with reduced element spacing", *Microwave and Optical Technology Letters*, vol. 46, no. 6, pp. 592-597, Jul 2005.
- [29] H. J. Chaloupka, Y. H. Lu and J. C. Coetzee, "A dual-polarized microstrip antenna array with port decoupling for MIMO systems", in *Proc. Int. Symp. Antennas and Propagation (ISAP)*, pp. 1229-1232, Aug 2004.
- [30] J. Litva and T. K. Lo, *Digital Beamforming in Wireless Communications*, 1st ed., Artech House, 1996.
- [31] P. R. P. Hoole, *Smart Antennas and Signal Processing for Communications, Biomedical and Radar Systems*, WIT Press, 2001.
- [32] H. Steyskal, "Digital beamforming – an emerging technology", *IEEE Military Communications Conference*, vol. 2, pp. 399-403, Oct 1988.
- [33] S. S. Jeon, Y. Wang, Y. Qian and T. Itoh, "A novel planar array smart antenna system with hybrid analogue-digital beamforming", *IEEE MTT-S Int. Microwave Symp. Dig.*, vol. 1, pp. 121-124, May 2001.
- [34] T. W. Nuteson and G. S. Mitchell, "Digital beamforming for smart antennas", *IEEE MTT-S Int. Microwave Symp. Dig.*, vol. 1, pp. 125-128, May 2001.
- [35] K. Mori, Y. Inoue, K. Minseok, K. Ichige and H. Arai, "DBF array antenna

- systems at 8.45GHz”, *IEEE Antennas and Propagation Society Int. Symp.*, vol. 3, pp. 222-225, Jul 2001.
- [36] K. Mori, Y. Inoue and H. Arai, “A digital beam forming by using low cost receiver at 2.6GHz”, *IEEE 11th Int. Conference on Antennas and Propagation*, vol. 1, pp. 24-27, Apr 2001.
- [37] T. W. Nuteson, J. S. Clark, D. S. Haque and G. S. Mitchell, “Digital beamforming and calibration for smart antennas using real-time FPGA processing”, *IEEE MTT-S Int. Microwave Symp. Dig.*, vol. 1, pp. 307-310, Jun 2002.
- [38] J. D. Fredrick, Y. Wang and T. Itoh, “A smart antenna receiver array using a single RF channel and digital beamforming”, *IEEE Trans. Microwave Theory and Techniques*, vol. 50, no. 12, pp. 3052-3058, Dec 2002.
- [39] C. Waldschmidt, J. V. Hagen and W. Wiesbeck, “Influence and modeling of mutual coupling in MIMO and diversity systems“, *IEEE Antennas and Propagation Society Int. Symp.*, vol. 3, pp.190-193, Jun 2002.
- [40] T. Svantesson and A. Ranheim, “Mutual coupling effects on the capacity of multielement antenna systems”, *IEEE Proc. Acoustics, Speech and Signal Processing*, vol. 4, pp. 2485-2488, May 2001.
- [41] R. G. Vaughan and J. B. Andersen, “Antenna diversity in mobile communications”, *IEEE Trans. Vehicular Technology*, vol. 36, no. 4, pp.149-172, Nov 1987.
- [42] R. S. Adve and T. K. Sarkar, “Compensation for the effects of mutual coupling on the direct data domain adaptive algorithms”, *IEEE Trans. Antennas and Propagation*, vol. 48, no. 1, pp.86-94, Jan 2000.
- [43] B. Friedlander and A. J. Weiss, “Direction finding in the presence of mutual coupling”, *IEEE Trans. Antennas and Propagation*, vol. 39, no. 3, pp.273-284,

- Mar 1991.
- [44] H. J. Chaloupka, "HTS antennas", in H. Weinstock and M. Nisenoff (eds.), *Microwave Superconductivity*, pp. 353-386, 2001.
- [45] R. C. Hansen, *Phased Array Antennas*, Wiley, 1998.
- [46] Mathematica, Version 5.0, Wolfram Research, Inc., 2003
- [47] Matlab, Version 7.3.0.267, The MathWorks, Inc., 2006
- [48] D. M. Pozar, *Microwave Engineering*, 2nd ed., Wiley, 1998.
- [49] D. H. Schradler, *Microstrip Circuit Analysis*, Prentice Hall, 1995.
- [50] J. A. G. Malherbe, *Microwave Transmission Line Filters*, Artech House, 1979.
- [51] P. L. D. Abrie, *The Design of Impedance-matching Networks for Radio Frequency*, Artech House, 1985.
- [52] IE3D, Version 11.23, Zeland Software Inc., 2006
- [53] J. C. Coetzee and Y. Yu, "An alternative approach to decoupling of arrays with reduced element spacing", in *Proc. Int. Symp. Antennas and Propagation (ISAP)*, Nov 2006.
- [54] C. Volmer, J. Weber, R. Stephan, K. Blau and M. A. Hein, "Decoupling and matching network for miniaturised 3-port antenna arrays based on 180° couplers", in *Proc. 2nd Int. ITG Conference on Antennas*, pp. 63-66, Mar 2007.
- [55] C. Volmer, J. Weber, R. Stephan, K. Blau and M. A. Hein, "An eigen-analysis of compact antenna arrays and its application to port decoupling", *IEEE Trans. Antennas and Propagation*, vol. 56, no. 2, pp. 360-370, Feb 2008.
- [56] J. C. Coetzee and Y. Yu, "Port decoupling for small arrays by means of an eigenmode feed network", *IEEE Trans. Antennas and Propagation*, vol. 56, no. 6, pp. 1587-1593, Jun 2008.
- [57] V. A. Monaco and P. Tiberio, "Computer-aided analysis of microwave circuits",

- IEEE Trans. Microwave Theory Techniques*, vol. 22, no. 3, pp. 249-263, Mar 1974.
- [58] Advanced Design System (ADS), version 2004A, Agilent, 2004.
- [59] D. K. Cheng, *Field and Wave Electromagnetics*, 2nd ed., Addison-Wesley, 1989.
- [60] G. P. Riblet, "A compact ring-style 8-port comparator circuit using coupled lines", *IEEE Trans. Microwave Theory Techniques*, vol. 41, no. 6/7, pp. 1224-1226, Jun/Jul 1993.
- [61] T. Kawai, K. Iio, I. Ohta and T. Kaneko, "A branch-line-type eight-port comparator circuit", *IEEE MTT-S Int. Microwave Symp. Dig.*, vol. 2, pp. 869-872, Jun 1991.
- [62] I. Ohta, T. Kawai, S. Shimahashi and K. Iio, "A transmission-line-type eight-port hybrid", *IEEE MTT-S Int. Microwave Symp. Dig.*, vol. 1, pp. 119-122, Jun 1992.
- [63] Ansoft High Frequency Structure Simulator (HFSS), version 9.2, Ansoft Corporation, 2005.

APPENDIX A

PROGRAM CODE IN MATHEMATICA FOR CLOSED-FORM DESIGN

EQUATIONS OF 6-ELEMENT ARRAY

(* Closed-form design equations for decoupling network *)
(* of circulant symmetric 6-element array *)
(* IE3D 6mono_3: example used in Chapter 4 *)

```
Sa11 = -0.4283+0.1619i;  
Sa12 = 0.3987+0.03147 i;  
Sa13 = 0.1021-0.1373 i;  
Sa14 = -0.02532-0.1243i;
```

```
Sa = {{Sa11, Sa12, Sa13, Sa14, Sa13, Sa12},  
      {Sa12, Sa11, Sa12, Sa13, Sa14, Sa13},  
      {Sa13, Sa12, Sa11, Sa12, Sa13, Sa14},  
      {Sa14, Sa13, Sa12, Sa11, Sa12, Sa13},  
      {Sa13, Sa14, Sa13, Sa12, Sa11, Sa12},  
      {Sa12, Sa13, Sa14, Sa13, Sa12, Sa11}};
```

```
Ind = IdentityMatrix[6];  
A1 = Ind+Sa;  
A2 = Inverse[Ind-Sa];  
Z0 = Rin= 50;  
Za=Z0×Dot[A1,A2];  
Za11 = Extract[Extract[Za,1],1];  
Za12 = Extract[Extract[Za,1],2];  
Za13 = Extract[Extract[Za,1],3];  
Za14 = Extract[Extract[Za,1],4];  
Zma = Za11 +2×Za12+2×Za13+Za14  
Zmb = Za11 - 2×Za12+2×Za13-Za14  
Zmc = Za11 - Za12-Za13+Za14  
Zme = Za11 + Za12-Za13-Za14
```

(* Decouple modes (c, d) and (e, f) *)

```
Rmc = Re[Zmc];  
Xmc = Im[Zmc];  
Rme = Re[Zme];  
Xme = Im[Zme];  
Aa = Rmc- Rme;  
Bb = 2×(Rmc×Xme - Rme×Xmc);  
Cc = Rmc×(Rme2+Xme2) - Rme×(Rmc2+Xmc2);
```

$$X11 = \frac{-Bb - \sqrt{Bb^2 - 4 \times Aa \times Cc}}{2 \times Aa}$$

$$B21 = \frac{1}{3-1} \times \left(\frac{Xmc + X11}{Rmc^2 + (Xmc + X11)^2} - \frac{Xme + X11}{Rme^2 + (Xme + X11)^2} \right)$$

$Z1 = \{ \{ X11 \times i, 0, 0, 0, 0, 0 \},$
 $\{ 0, X11 \times i, 0, 0, 0, 0 \},$
 $\{ 0, 0, X11 \times i, 0, 0, 0 \},$
 $\{ 0, 0, 0, X11 \times i, 0, 0 \},$
 $\{ 0, 0, 0, 0, X11 \times i, 0 \},$
 $\{ 0, 0, 0, 0, 0, X11 \times i \} \};$
 $Y2 = \{ \{ 2 \times B21 \times i, -B21 \times i, 0, 0, 0, -B21 \times i \},$
 $\{ -B21 \times i, 2 \times B21 \times i, -B21 \times i, 0, 0, 0 \},$
 $\{ 0, -B21 \times i, 2 \times B21 \times i, -B21 \times i, 0, 0 \},$
 $\{ 0, 0, -B21 \times i, 2 \times B21 \times i, -B21 \times i, 0 \},$
 $\{ 0, 0, 0, -B21 \times i, 2 \times B21 \times i, -B21 \times i \},$
 $\{ -B21 \times i, 0, 0, 0, -B21 \times i, 2 \times B21 \times i \} \};$
 $Zp = \text{Inverse}[\text{Inverse}[Za + Z1] + Y2]$
 $Zp11 = \text{Extract}[\text{Extract}[Zp, 1], 1];$
 $Zp12 = \text{Extract}[\text{Extract}[Zp, 1], 2];$
 $Zp13 = \text{Extract}[\text{Extract}[Zp, 1], 3];$
 $Zp14 = \text{Extract}[\text{Extract}[Zp, 1], 4];$
 $Zpma = Zp11 + 2 \times Zp12 + 2 \times Zp13 + Zp14$
 $Zpmb = Zp11 - 2 \times Zp12 + 2 \times Zp13 - Zp14$
 $Zpmc = Zp11 - Zp12 - Zp13 + Zp14$
 $Zpme = Zp11 + Zp12 - Zp13 - Zp14$

(* Decouple modes b and (c, d, e, f)*)

$Rpmb = \text{Re}[Zpmb];$
 $Xpmb = \text{Im}[Zpmb];$
 $Rpmc = \text{Re}[Zpmc];$
 $Xpmc = \text{Im}[Zpmc];$
 $Aaa = Rpmb - Rpmc;$
 $Bbb = 2 \times (Rpmb \times Xpmc - Rpmc \times Xpmb);$
 $Ccc = Rpmb \times (Rpmc^2 + Xpmb^2) - Rpmc \times (Rpmb^2 + Xpmb^2);$
 $X31 = \frac{-Bbb - \sqrt{Bbb^2 - 4 \times Aaa \times Ccc}}{2 \times Aaa}$

$B41 = \frac{1}{0-3} \times \left(\frac{Xpmb + X31}{Rpmb^2 + (Xpmb + X31)^2} - \frac{Xpmb + X31}{Rpmc^2 + (Xpmb + X31)^2} \right)$

$Z3 = \{ \{ X31 \times i, 0, 0, 0, 0, 0 \},$
 $\{ 0, X31 \times i, 0, 0, 0, 0 \},$
 $\{ 0, 0, X31 \times i, 0, 0, 0 \},$
 $\{ 0, 0, 0, X31 \times i, 0, 0 \},$
 $\{ 0, 0, 0, 0, X31 \times i, 0 \},$
 $\{ 0, 0, 0, 0, 0, X31 \times i \} \};$
 $Y4 = \{ \{ 2 \times B41 \times i, 0, -B41 \times i, 0, -B41 \times i, 0 \},$
 $\{ 0, 2 \times B41 \times i, 0, -B41 \times i, 0, -B41 \times i \},$
 $\{ -B41 \times i, 0, 2 \times B41 \times i, 0, -B41 \times i, 0 \},$
 $\{ 0, -B41 \times i, 0, 2 \times B41 \times i, 0, -B41 \times i \},$
 $\{ -B41 \times i, 0, -B41 \times i, 0, 2 \times B41 \times i, 0 \},$
 $\{ 0, -B41 \times i, 0, -B41 \times i, 0, 2 \times B41 \times i \} \};$

$Zpp = \text{Inverse}[\text{Inverse}[Zp + Z3] + Y4]$
 $Zpp11 = \text{Extract}[\text{Extract}[Zpp, 1], 1];$
 $Zpp12 = \text{Extract}[\text{Extract}[Zpp, 1], 2];$

$$\begin{aligned}
Z_{pp13} &= \text{Extract}[\text{Extract}[Z_{pp},1],3]; \\
Z_{pp14} &= \text{Extract}[\text{Extract}[Z_{pp},1],4]; \\
Z_{ppma} &= Z_{pp11} + 2 \times Z_{pp12} + 2 \times Z_{pp13} + Z_{pp14} \\
Z_{ppmb} &= Z_{pp11} - 2 \times Z_{pp12} + 2 \times Z_{pp13} - Z_{pp14} \\
Z_{ppmc} &= Z_{pp11} - Z_{pp12} - Z_{pp13} + Z_{pp14} \\
Z_{ppme} &= Z_{pp11} + Z_{pp12} - Z_{pp13} - Z_{pp14}
\end{aligned}$$

(* Decouple modes a and (b, c, d, e, f) *)

$$\begin{aligned}
R_{ppma} &= \text{Re}[Z_{ppma}]; \\
X_{ppma} &= \text{Im}[Z_{ppma}]; \\
R_{ppmb} &= \text{Re}[Z_{ppmb}]; \\
X_{ppmb} &= \text{Im}[Z_{ppmb}]; \\
Aaaa &= R_{ppma} - R_{ppmb}; \\
Bbbb &= 2 \times (R_{ppma} \times X_{ppmb} - R_{ppmb} \times X_{ppma}); \\
Cccc &= R_{ppma} \times (R_{ppmb}^2 + X_{ppmb}^2) - R_{ppmb} \times (R_{ppma}^2 + X_{ppma}^2);
\end{aligned}$$

$$X_{51} = \frac{-Bbbb - \sqrt{Bbbb^2 - 4 \times Aaaa \times Cccc}}{2 \times Aaaa}$$

$$B_{61} = \frac{1}{0-1} \times \left(\frac{X_{ppma} + X_{51}}{R_{ppma}^2 + (X_{ppma} + X_{51})^2} - \frac{X_{ppmb} + X_{51}}{R_{ppmb}^2 + (X_{ppmb} + X_{51})^2} \right)$$

$$Z_5 = \{ \{ X_{51} \times i, 0, 0, 0, 0, 0 \}, \\
\{ 0, X_{51} \times i, 0, 0, 0, 0 \}, \\
\{ 0, 0, X_{51} \times i, 0, 0, 0 \}, \\
\{ 0, 0, 0, X_{51} \times i, 0, 0 \}, \\
\{ 0, 0, 0, 0, X_{51} \times i, 0 \}, \\
\{ 0, 0, 0, 0, 0, X_{51} \times i \} \};$$

$$Y_6 = \{ \{ 5/6 \times B_{61} \times i, -1/6 \times B_{61} \times i, -1/6 \times B_{61} \times i, -1/6 \times B_{61} \times i, -1/6 \times B_{61} \times i, -1/6 \times B_{61} \times i \}, \\
\{ -1/6 \times B_{61} \times i, 5/6 \times B_{61} \times i, -1/6 \times B_{61} \times i, -1/6 \times B_{61} \times i, -1/6 \times B_{61} \times i, -1/6 \times B_{61} \times i \}, \\
\{ -1/6 \times B_{61} \times i, -1/6 \times B_{61} \times i, 5/6 \times B_{61} \times i, -1/6 \times B_{61} \times i, -1/6 \times B_{61} \times i, -1/6 \times B_{61} \times i \}, \\
\{ -1/6 \times B_{61} \times i, -1/6 \times B_{61} \times i, -1/6 \times B_{61} \times i, 5/6 \times B_{61} \times i, -1/6 \times B_{61} \times i, -1/6 \times B_{61} \times i \}, \\
\{ -1/6 \times B_{61} \times i, -1/6 \times B_{61} \times i, -1/6 \times B_{61} \times i, -1/6 \times B_{61} \times i, 5/6 \times B_{61} \times i, -1/6 \times B_{61} \times i \}, \\
\{ -1/6 \times B_{61} \times i, -1/6 \times B_{61} \times i, -1/6 \times B_{61} \times i, -1/6 \times B_{61} \times i, -1/6 \times B_{61} \times i, 5/6 \times B_{61} \times i \} \};$$

$$\begin{aligned}
Z_{ppp} &= \text{Inverse}[\text{Inverse}[Z_{pp} + Z_5] + Y_6] \\
Z_{ppp11} &= \text{Extract}[\text{Extract}[Z_{ppp},1],1]; \\
Z_{ppp12} &= \text{Extract}[\text{Extract}[Z_{ppp},1],2]; \\
Z_{ppp13} &= \text{Extract}[\text{Extract}[Z_{ppp},1],3]; \\
Z_{ppp14} &= \text{Extract}[\text{Extract}[Z_{ppp},1],4]; \\
Z_{pppma} &= Z_{ppp11} + 2 \times Z_{ppp12} + 2 \times Z_{ppp13} + Z_{ppp14} \\
Z_{pppmb} &= Z_{ppp11} - 2 \times Z_{ppp12} + 2 \times Z_{ppp13} - Z_{ppp14} \\
Z_{pppmc} &= Z_{ppp11} - Z_{ppp12} - Z_{ppp13} + Z_{ppp14} \\
Z_{pppme} &= Z_{ppp11} + Z_{ppp12} - Z_{ppp13} - Z_{ppp14}
\end{aligned}$$

$$\begin{aligned}
R_{pppma} &= \text{Re}[Z_{pppma}]; \\
X_{pppma} &= \text{Im}[Z_{pppma}];
\end{aligned}$$

(* Matching network *)

$$B_{71} = \frac{X_{pppma} + \sqrt{R_{pppma} \div R_{in} \times \sqrt{R_{pppma}^2 + X_{pppma}^2} - R_{in} \times R_{pppma}}}{R_{pppma}^2 + X_{pppma}^2}$$

$$X81 = \frac{1}{B71} + \frac{Xpppma \times Rin}{Rpppma} - \frac{Rin}{B71 \times Rpppma}$$

$$Y7 = \{ \{B71 \times i, 0, 0, 0, 0\}, \\ \{0, B71 \times i, 0, 0, 0\}, \\ \{0, 0, B71 \times i, 0, 0\}, \\ \{0, 0, 0, B71 \times i, 0\}, \\ \{0, 0, 0, 0, B71 \times i\}, \\ \{0, 0, 0, 0, B71 \times i\} \};$$

$$Z8 = \{ \{X81 \times i, 0, 0, 0, 0\}, \\ \{0, X81 \times i, 0, 0, 0\}, \\ \{0, 0, X81 \times i, 0, 0\}, \\ \{0, 0, 0, X81 \times i, 0\}, \\ \{0, 0, 0, 0, X81 \times i\}, \\ \{0, 0, 0, 0, X81 \times i\} \};$$

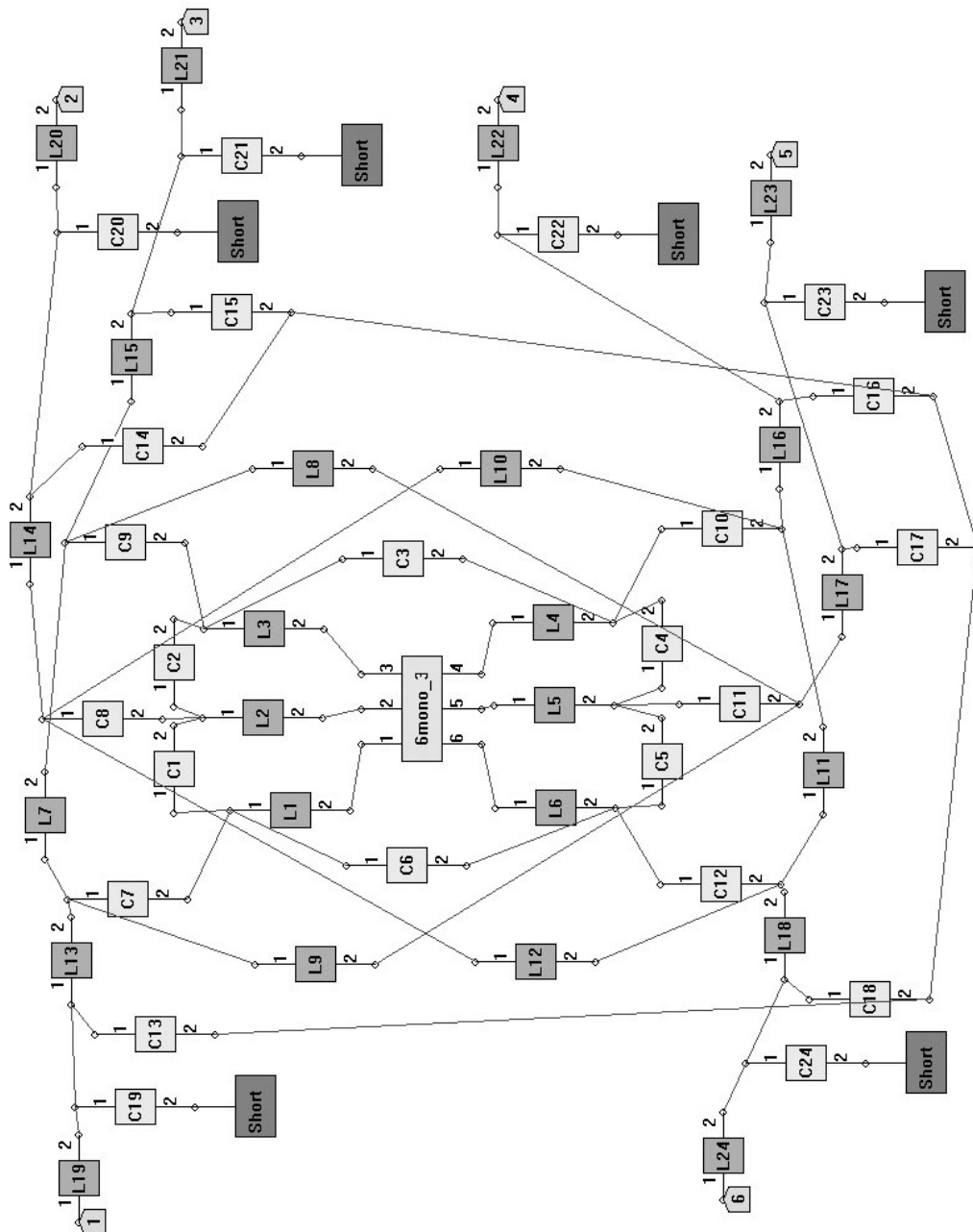
$$Z4p = \text{Inverse}[\text{Inverse}[Zppp] + Y7] + Z8$$

APPENDIX B

CIRCUIT MODEL IN IE3D TO CALCULATE THE S-PARAMETERS OF THE DECOUPLED 6-ELEMENT ARRAY

The “6mono_3” is the geometry model in IE3D of the 6-element array in Chapter 4.

Values of capacitors and inductors are calculated according to Table 4.4.

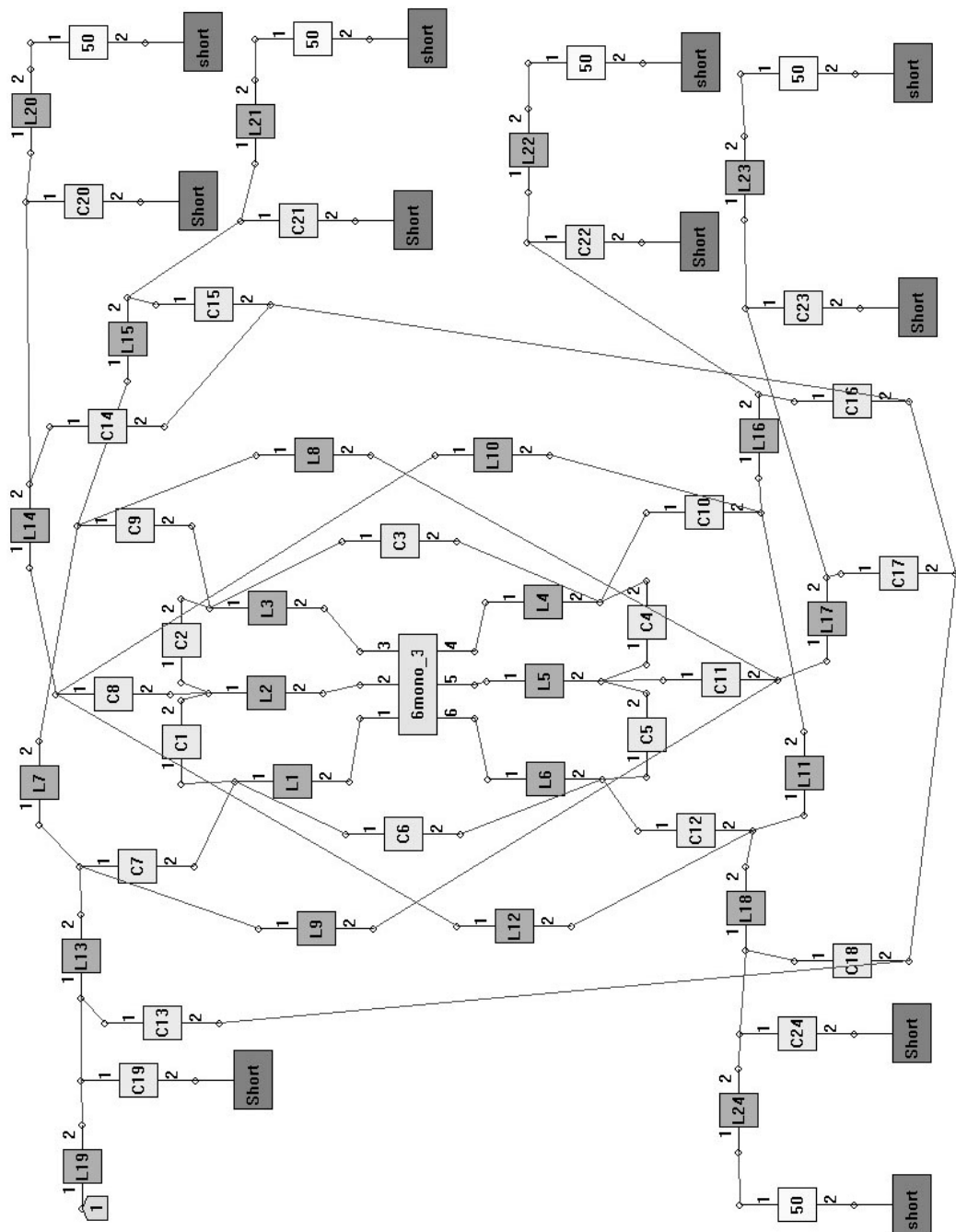


APPENDIX C

CIRCUIT MODEL IN IE3D TO CALCULATE THE RADIATION PATTERN OF THE DECOUPLED 6-ELEMENT ARRAY

The “6mono_3” is the geometry model in IE3D of the 6-element array in Chapter 4.

Values of capacitors and inductors are calculated according to Table 4.4.

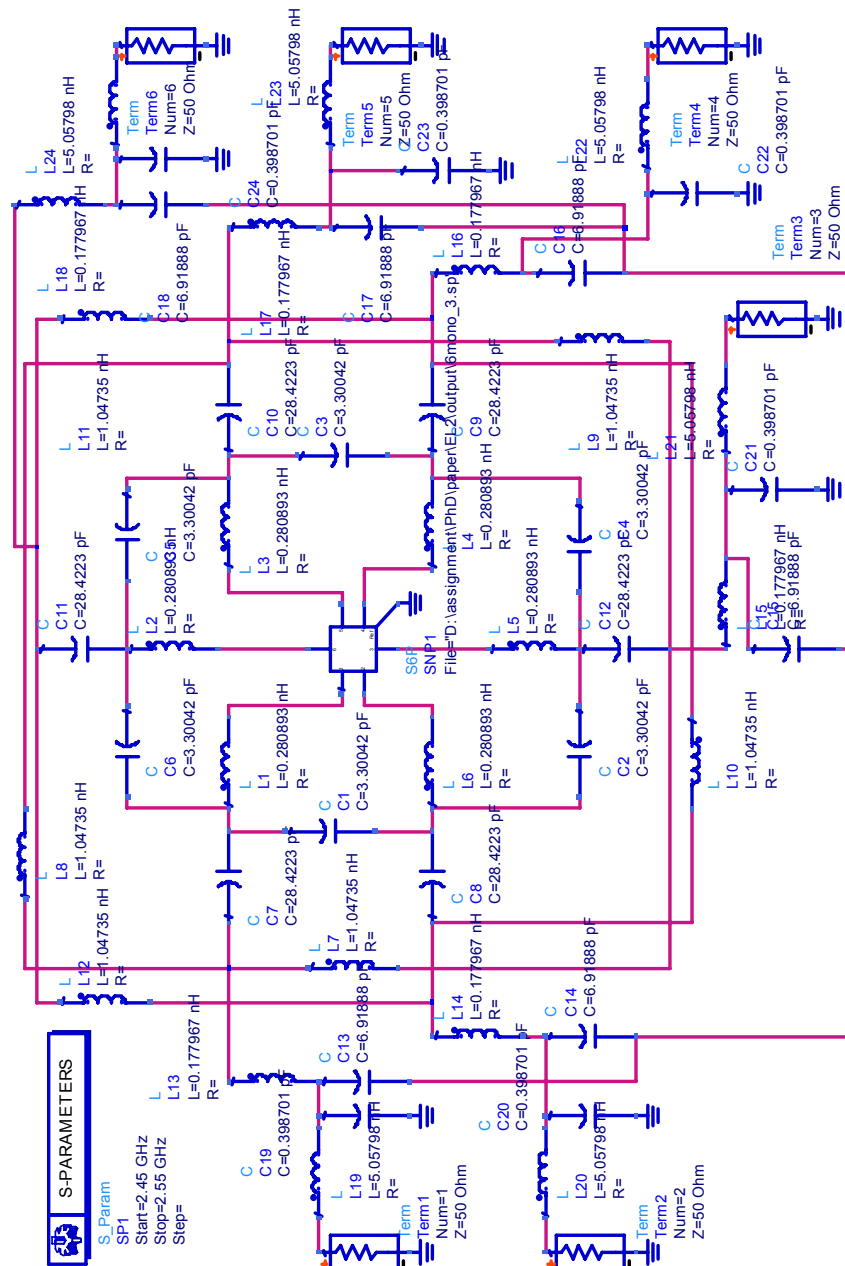


APPENDIX D

CIRCUIT MODEL IN ADS TO CALCULATE THE S-PARAMETERS OF THE DECOUPLED 6-ELEMENT ARRAY

The data item “6mono_3.sp” is the S-parameters of the 6-element array in Chapter 4.

Values of capacitors and inductors are calculated according to Table 4.4.



APPENDIX E

ARRAY MODEL IN HFSS TO CALCULATE THE RADIATION PATTERN WITH FINITE GROUND PLANE

To include the effect of finite ground plane during radiation pattern calculation, this model was created in HFSS for the array (without decoupling network) in Figure 5.33. The dimensions of the monopole array are as in Section 5.4.3. The array ports are excited by respective output voltages of the modal feed network for each mode, which are obtained by feeding one of the input ports of the modal feed network while other input ports are terminated in matched load. The results with this model were discussed in Section 5.4.3.

